INTEGRATING
SOLID-STATE NANOPORE SENSORS
WITHIN VARIOUS MICROFLUIDIC ARRAYS
FOR SINGLE-MOLECULE DETECTION

Radin Tahvildari

A thesis submitted to the
Faculty of Graduate and Postdoctoral Studies
in partial fulfillment of the requirements for the degree of

DOCTORATE IN PHILOSOPHY

in Physics

uOttawa

Ottawa-Carleton Institute for Physics, Department of Physics
Faculty of Science
University of Ottawa

© Radin Tahvildari, Ottawa, Canada, 2017

Abstract

The miniaturization afforded by the integration of microfluidic technologies within lab-on-a-chip devices has greatly enhanced analytical capabilities in several key applications. Microfluidics has been utilized in a wide range of areas including sample preparation and analysis, DNA microarrays[1], cell detection[2], as well as environmental monitoring[3]. The use of microfluidics in these applications offer many unique advantages: reduction in the required sample size, reduction in analysis time, lowered cost through batch fabrication, potentially higher throughput and the vision of having such devices used in portable systems.

Nanopore sensors are a relatively new technology capable of detection and analysis with single-molecule sensitivity, and show promise in many applications related to the diagnosis and treatment of many diseases.[4,5] Recently, some research groups demonstrated the integration of nanopores within microfluidic devices to increase analytical throughput.[6–8] This thesis describes a methodology for integrating nanopore sensors within microfluidic devices with the aim of enhancing the analytical capabilities required to analyze biomolecular samples.

In this work, the first generation of an integrated nanopore-microfluidic device[9] contained multiple independently addressable microfluidic channels to fabricate an array of nanopore sensors using controlled breakdown (CBD)[10]. Next, for the second generation[11], we added pneumatic microvalves to manipulate electrical and fluidic access through connected microfluidic channels. As a proof-of-concept, single molecules (single- and double-stranded DNA, proteins) were successfully detected in the devices.

It is also demonstrated that inclusion of the microfluidic via (microvia) limited the exposed area of the embedded silicon nitride membrane to the solution. This helped in localizing nanopore formation by confining the electric field to specific regions of the insulating membrane while significantly reducing high frequency noise in the ionic current signal through the reduction of chip capacitance.

The devices highlighted in this thesis were designed and fabricated using soft lithography techniques which are available in most biotechnology laboratories. The core of this thesis is based on two scientific articles (Chapters 3 and 4), which are published in peer-reviewed scientific journals. These chapters are preceded by an introductory chapter and another chapter detailing the experimental setup and the methods used during the course of this study.

Reference:

[1] R. H. Liu, J. Yang, R. Lenigk, J. Bonanno, P. Grodzinski, *Anal. Chem.* **2004**, *76*, 1824.

[2] B. G. Chung, L. A. Flanagan, S. W. Rhee, P. H. Schwartz, A. P. Lee, E. S. Monuki, N. L. Jeon, *Lab. Chip* **2005**, *5*, 401.

[3] L. Marle, G. M. Greenway, *TrAC Trends Anal. Chem.* **2005**, *24*, 795.

[4] C. Shasha, R. Y. Henley, D. H. Stoloff, K. D. Rynearson, T. Hermann, M. Wanunu, *ACS Nano* **2014**, *8*, 6425.

[5] J. E. Reiner, A. Balijepalli, J. W. F. Robertson, J. Campbell, J. Suehle, J. J. Kasianowicz, *Chem. Rev.* **2012**, *112*, 6431.

[6] E. M. Nelson, V. Kurz, J. Shim, W. Timp, G. Timp, *Analyst* **2012**, *137*, 3020.

[7] N. A. W. Bell, V. V. Thacker, S. Hernández-Ainsa, M. E. Fuentes-Perez, F. Moreno-Herrero, T. Liedl, U. F. Keyser, *Lab. Chip* **2013**, *13*, 1859.

[8] T. Jain, R. J. S. Guerrero, C. A. Aguilar, R. Karnik, *Anal. Chem.* **2013**, *85*, 3871.

[9] R. Tahvildari, E. Beamish, V. Tabard-Cossa, M. Godin, *Lab. Chip* **2015**, *15*, 1407.

[10] W. H. H. Kwok, New Approach in Fabrication of Solid-State Nanopore for Bio-Sensing Applications, 2015, **2015**.

[11] R. Tahvildari, E. Beamish, K. Briggs, S. Chagnon-Lessard, A. N. Sohi, S. Han, B. Watts, V. Tabard-Cossa, M. Godin, *Small* **2016**, DOI 10.1002/smll.201602601.

Statement of Originality

I hereby declare that, to the best of my knowledge, the presented work in this thesis is entirely original. Research during the course of this study was based on a collaborative project between **Abbott Laboratories** and conducted under the supervision of **Professor Michel Godin** and co-supervised by **Professor Vincent Tabard-Cossa** in the Centre for Interdisciplinary Nanophysics, Department of Physics at the University of Ottawa.

The following patent application has been filed covering various aspects of this novel method and the rights of this intellectual property has been licensed by **Abbott Laboratories**.

- V. Tabard-Cossa, M. Godin, **R. Tahvildari**, E. Beamish, "Integrating nanopore sensors within microfluidic channel arrays using controlled breakdown", WO/2016/098080.

Chapters 3 and 4 are comprised of the following manuscripts. A manuscript information sheet is preceded for each of these chapters to detail the contribution of other authors.

- **R. Tahvildari,** E. Beamish, K. Briggs, S. Chagnon-lessard, A. Najafi Sohi, S. Han, B. Watts, V. Tabard-Cossa, M. Godin, "Manipulating electrical and fluidic access in an integrated nanopore-microfluidic arrays using microvalves", *Small,* DOI: 10.1002/smll.201602601
- **R. Tahvildari*,** E. Beamish*****, V. Tabard-Cossa, M. Godin, "Integrating nanopore sensors within microfluidic channel arrays using controlled breakdown", *Lab On a Chip*, 15, 1407-1411, 2015. **These authors contributed equally.*

The work in Chapter 3 was presented at the **4th International Conference on Bio-Sensing Technology, Lisbon, Portugal** in May 2015.

- **R. Tahvildari**, E. Beamish, V. Tabard-Cossa, M. Godin, "Integrating nanopore sensors within microfluidic networks using controlled breakdown of a dielectric", *the 4th International Conference on Bio-Sensing Technology*, Lisbon, Portugal, 2015. (Poster)

In partial fulfilment of PhD requirements, an oral presentation was given at the Ottawa-Carleton Institute of Physics (OCIP) graduate student symposium in May 2016.

- **Radin Tahvildari**, *Integration of Nanopore sensors in Microfluidic networks (INM)*, Ottawa-Carleton Institute of Physics (May 2016)

Statement of Contribution

I, Radin Tahvildari, contributed the large majority of the work presented in this thesis. In regards to the published works of Chapters 3 and 4, I directly contributed to the experiment designs, mask designs, experimental set up design (including faraday cage design and fluid flow setup), microfabrication (soft lithography, PDMS moulding, assembly of all presented devices, and chemical treatment), nanopores fabrication, sample preparation, data acquisition and analysis.

Eric Beamish is listed as having contributed equally to the work presented in Chapter 3. Eric Beamish's contributions were complementary to my own and involves providing advice on the setup and initial experiments, performing the finite element modeling of the electric field in the presented devices, and assistance in writing the manuscript.

The nanopore fabrication circuit was designed by Professor Vincent Tabard-Cossa and Dr. Harold Kwok, and built by Lukasz Andrzejewski. The LabView routines for data acquisition and analysis were versions of code provided by Professor Vincent Tabard-Cossa and modified by Dr. Harold Kwok and Eric Beamish. The work was done under the supervision of Professor Michel Godin and Professor Vincent Tabard-Cossa.

In Chapter 4, other researchers also contributed during the course of this work. Eric Beamish provided technical advice and assisted in editing all drafts of the manuscript. Kyle Briggs and Sophie Chagnon-Lessard assisted in some data analysis. Dr. Benjamin Watts and Shuo Han assisted with some microfabrication and performed preliminary experiments. Dr. Ali Najafi Sohi provided advices on the devices treatment.

Individual contributions are outlined prior to the manuscripts presented in Chapters 3 and 4 of this thesis.

Acknowledgements

First, I would like to express my gratitude and appreciation to my supervisors Prof. Michel Godin and Prof. Vincent Tabard-Cossa for giving the opportunity to pursue my PhD study. Five years ago when I started my research at the Godin lab, I had no knowledge of microfluidics but I was so lucky to be introduced to Prof. Gary Slater and collaborated with his PhD student, Dr. Tyler Shendruk, on a fruitful project. That was a great chance to learn and I achieved lots of hands-on experience while conducting the experimental part of the project. I should thank Dr. Maryam Mirzaei who trained me with patience how to do the microfabrication.

Life is made of lots of moments and events. They are like chapters in a book that is written every single day. Sometimes, a chapter includes an unexpected bump which hits you all at once, you may get frustrated but at the end you should move on, because that is the only option. However, I truly believe the presence of good friends ease the toughest moments in one's life. I was truly so lucky to be surrounded with the best ever people. Herein, I would like to thank all the present and former members of the Godin, Tabard-Cossa and Pelling labs, specifically: Adefami Adeyemi, Adriana Prystay, Cedric Eveleigh, Daniel Modulevsky, Daniel Sigouin, Desola Olurotimi Odedina, Dylan Stone, Dr. Ainara Benavente, Dr. Ali Najafi Sohi, Dr. Autumn Carlsen, Dr. Benjamin Watts, Dr. Charles Cuerrier, Dr. Daniel Tessier, Dr. Jason Riordon, Gabriel Dupras, Jeremie Gaudreau, Jose Bustamante, Dr. Kristina Haase, Keith Ludlow, Kyle Briggs, Laurent Gagné-Dumais, Louise Munro, Martin Charron, Matias Calderini, Matt Walker, Matt Waugh, Michael Nash, Nicholas Catafard, Nicholas Bodé, Philipp Karau, Sebastian Hadjiantoniou, Ryan Hickey, Shuo Han, Sophie Chagnon-Lessard, Veronika Cencen, Wenyang Jing and Zach Roelen.

Our daily greetings, the conversations at lunchtime about everything and nothing, after-work beers, poker nights, gatherings, cottage trips and camping, your care, empathy, support, and encouragement motivated me and gave me the push to keep on and have meant so much to me. You have been my family and I've lived with all of you every single day. All the good memories will stay fresh in my mind, no matter where I would be. The word "Thank You" do not seem enough, but from the bottom of my heart I would like to say, **Thank You!**

The last but the most important person was Eric Beamish. He has not been only a colleague, or just a friend but like a brother. He was always there, for a talk, helping out, discussion, brainstorming, venting, fighting, and even being a partner in crime! I was also overwhelmed by his wife and his family's kindness on different occasions. They always warmly welcomed and treated me like their own family member. I wish I could find the words to perfectly express my highest gratitude and respect to them.

I'd like to dedicate this thesis to my sister, Ladan, who is my role model for everything in life specifically, her capabilities in handling the life challenges and always set the best as the goals in life. Her dream was to gather the circle of family once again, but destiny brutally destroyed everything and we just remained for each other. I am now here and get to this level of success because of all her care and efforts about the family.

Finally, I would like to close this chapter of my life in memories of my beloved parents, Louise Tahvildary and Aman Tahvildari, and my brother Babak. You are really missed at this moment!

List of Abbreviations

General

- AFM: Atomic-Force Microscopy
- CBD: Controlled Breakdown
- CMOS: Complementary Metal-Oxide-Semiconductor
- DAQ: Data Acquisition card
- DC: Direct Current
- FIB: Focused Ion Beam
- FFF: Field Flow Fractionation
- fFFF: faxén-mode Field Flow Fractionation
- GrFFF: Gravitational Field Flow Fractionation
- HC: Hydrodynamic Chromatography
- LPCVD: Low-Pressure Chemical Vapour Deposition
- LOC: Lab-On-a-Chip
- mV: milliVolt
- MPCD: Multi-Particle Collision Dynamics
- nA: nanoAmpere
- nFFF: normal-mode Field Flow Fractionation
- NMR: Nuclear Magnetic Resonance
- pA: picoAmpere
- PCR: Polymerase Chain Reaction
- PSD: Power Spectral Density
- PTFE: PolyTetraFluoroEthylene
- sFFF: steric-mode Field Flow Fractionation
- SMR: Suspended Microchannel Resonator
- SNR: Signal-to-Noise Ratio
- STM: Scanning Tunneling Microscopy
- TEM: Transmission Electron Microscopy

Chemical

- Ag: Silver
- AgCl: Silver chloride
- bp: Base pair
- DI Water: Deionized waster
- DNA: Deoxyribonucleic acid
- dsDNA: Double-stranded DNA
- EthOH: Ethanol
- HF: Hydrofluoric acid
- IPA: Isopropanol
- KCl: Potassium chloride
- KOH: Potassium hydroxide
- LiCl: Lithium chloride
- PDMS: Polydimethylsiloxane
- PEEK: Polyether ether ketone
- RNA: Ribonucleic acid
- Si: Silicon
- SiN: Silicon nitride
- SiO_2: Silicon oxide
- ssDNA: Single-stranded DNA

Table of Contents

List of Figures

List of Tables

Chapter 1 | Introduction

1.1 Biophysics: An overview

Life intrinsically consists of multi-scaled components ranging from nanometers (molecules) to hundred meters (trees) and from femtoseconds (chemical reactions) to millennium (evolution). Biophysics is an interdisciplinary branch of science that seeks to explore biological systems at those many length scales, a concept originally introduced by Karl Pearson in 1892.[1] Although this science had not advanced considerably back then, he expressed that physical phenomena were the root of all biological processes.

A biophysicist employs principles of physics to study living systems at different length scales, from atoms, molecules and cells to organisms, populations and even the biosphere.[2] By combining the natural and life sciences and utilizing novel techniques, it would be possible to understand and develop insight into more complex biological systems and their interactions.

In modern life, millions are following a variety of diets and exercise plans only in the hope of elongating their lives for as long as possible. However, recent biomedical improvements in the research spheres of molecular repair and stem cells transplant are already enhancing people's life expectancy. All these advancements can be achieved when the scale of studies changed from cell to single-molecule.

Nucleic acids including DNA and RNA, carry genes that contain all information that an organism needs for growth, reproduction and proper functionality. Based on the central dogma of molecular biology, stated by Francis Crick[3] and presented in Figure 1-1, whole-genome sequencing of DNA yield information similarly obtained from RNA and/or proteins. This information can optimize identifying inherited disorders, revealing comprehensive view of the mutations in genes which cause benign tumors and/or malignancy and tracking disease outbreaks.[4] Moreover, high success rate in disease treatments, better drugs and long-term prognosis have greater likelihood by having access to a person's genome.[5]

In a nutshell, studies and analysis of gene function and expression require accuracy in detection of DNA and RNA and also specific proteins. Thus, research and the quest for techniques that reach the single-molecule detection limit have been emerged significantly by biophysicists over the past few decades. This demand also aims for faster and cheaper technology.

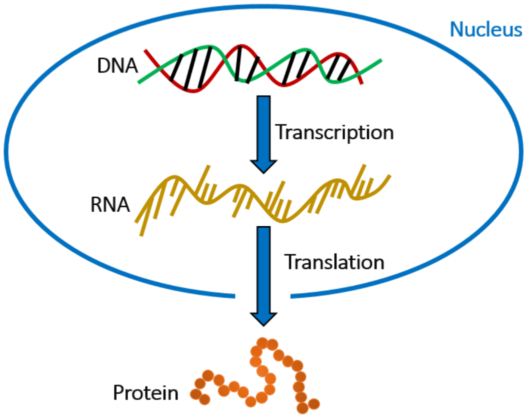

Figure 1-1 Overview of the central dogma shows the flow of genetic information inside a biological system. In order to make protein, a cell first transcribes genetic information from DNA onto a temporary template of RNA. Then each RNA translates a set of specific information for synthesis of a particular protein.

1.2 Structure of DNA

DNA was first identified in the late 1860s and decades later its primary chemical components and the ways in which they joined together were revealed.[6] DNA is a semi-flexible charged biopolymer constructed from four different monomers (nucleotides). The nucleotides are built from the bases adenine (A), thymine (T), guanine (G), and cytosine (C), placed in a very specific way and connected to a phosphate group and a deoxyribose sugar. The separating space between each nucleotide along a backbone is ~0.34 nm. Single-stranded DNA (ssDNA) contains a sequence of nucleotides bonded to a sugar-phosphate backbone. It has a cross section of approximately ~1.2-1.5 nm. In the helix structure of a dsDNA, the base pairs form by individual hydrogen bonds between adenine and thymine (A with T) and cytosine with guanine (C with G), illustrated in Figure 1-2. The cross section of dsDNA is ~2.2 nm. The presence of the phosphate group makes DNA a negatively charged molecule.[6]

The sequence of base pairs carries the genetic instructions used in the development and functionality of all living organisms.

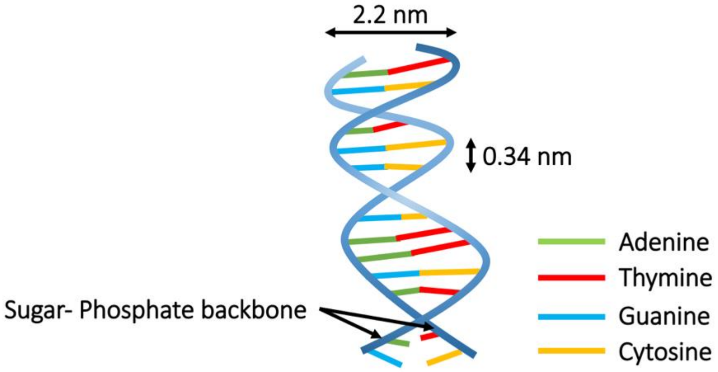

Figure 1-2 The double-helical structure of double-stranded DNA. The schematic is adapted from Reference[6].

Several universally accepted scales are used to explain the state of DNA (relaxed or confined).[7] For example, the conformation of a molecule in solution of interest depends on the ionic strength of the buffer. The presence of the phosphate group makes DNA a negatively charged molecule, therefore positively charged ions are attracted while negative ones are repulsed. Thus the concentration of counterions decays exponentially around DNA molecule. Debye length, is the characteristic length scale for the decay of the charge layer around the molecule.[7]

Contour length L is the total length of fully stretched dsDNA. For N monomers of length d (one base pair) it is given by[8],

$$\mathrm{L} = \mathrm{Nd} \tag{1.2}$$

In the relaxed state, DNA has a spherical shape (coiled up) and is defined by the radius of gyration[7]:

$$\mathrm{R_g} \sim N^{\nu} \tag{1.3}$$

This describes the average dimension of the molecule which strongly depends on its stiffness. The interactions between DNA molecule and the solvent are characterized by the excluded volume, or Flory exponent ν. This parameter depends on the properties of both molecules and the solvent. For a good solvent, that interactions between molecule and the solvent are favourable, ν=0.6.[7]

Another scale is Persistence length, L_p, defined by a semi-flexible unit of the strand with a certain degree of stiffness, much larger than the size of one monomer. This length depends on several factors including the solution concentration. Typically, it is about 50 nm, equal to ~150 base pairs.[8]

1.3 Molecular characterization down to single-molecule detection

Over the last three decades of the twentieth century, biophysicists have been enabled to study biomolecular systems at the single-molecule scale using new techniques based on advances in optics and miniaturization of mechanical systems. The single-molecule detection was first done by studying the activity of single enzyme molecule (β-galactosidase) trapped in a microdroplet using non-fluorescent material (fluorogenic substrate).[9] This substrate is reacted with an enzyme to produce fluorescent compound. In this method the solution containing the enzyme and the substrate is dispersed into droplets of 0.1 to 40 µm diameter on a microscope slide coated with silicone. Droplets with measurable fluorescence appear only when the enzyme molecule is present.[9]

For several years other techniques such as gel electrophoresis[10], X-ray crystallography[11], and nuclear magnetic resonance (NMR)[12] have provided detailed information on biomolecular structure albeit not at the scale of individual molecules. In recent years approaches with the ability to probe single molecules were developed, including fluorescence-based techniques[13], optical and magnetic tweezers[14], atomic force microscopy (AFM) and scanning tunneling microscopy (STM)[15].

Nanopore sensors offer a new approach for single-molecule sensing. This label-free sensing technology can be done without the need of any optical instruments, amplification or purification of the target molecule.[16,17] Furthermore, the scale of the pores is typically the same as the molecules of interest. For instance, a biological nanopore can be formed with a sub-nm inner diameter. This diameter is five orders of magnitude smaller than a human hair and similar to the size of many molecules. This unique characteristic makes nanopore-based sensing attractive for analysis of individual molecules. This youngest member of single-molecule detection techniques is also low cost, typically requires low reagent volumes and is easily scalable for high-throughput analysis.[16]

Oxford Nanopore Technologies, founded in 2005, is a leading company in development of nanopore-based DNA sequencing systems for commercial use. Since May 2015, MinION as the first handheld nanopore DNA sequencer is commercially available. This platform is compatible with complex samples including blood, serum and water. To run real-time analysis, the device should only be plugged in to a PC or laptop using a USB while no additional computing infrastructure is needed. The core of this device is a protein nanopore set in an arrayed sensor chip. Biased potentials across each nanopore are applied by custom high-performance Application-Specific Integrated Circuits (ASICs). They measure the resulting ionic current flow at high sampling frequencies, tens of kHz per nanopore, while minimizing measurement noise and maximising signal.[18] This device only costs $1000 with simple 10-minute sample preparation.[19]

To meet their goal: "to enable the analysis of any living thing by any person, in any environment", the company is now working on development of their smallest sequencing device, SmigION, designed to be used at any location with a smartphone.[20]

1.4 Nanopore sensors: An ion microscope and a single-molecule force apparatus

1.4.1 Brief history

In 1947, Wallace H. Coulter[21] introduced his aperture-based resistive counter which was designed for counting and sizing blood cells. He never assumed this counter could be the first embodiment of a nanopore sensor. His principle gave birth to automated hematology, particle counting industry and later was used in quality control of consumer products.[21] He made the first counter out of a cellophane wrapper with a poked hole that divided a filled glass chamber with electrolyte solution into two. A pair of electrodes connected to a source of electric current was placed across the aperture while the solution conductivity was measured. Typically, the passage of suspended cells through the aperture and blocking it results in discrete short pulses. The frequency of these pulses is related to the total amount of cells present in the solution while pulses magnitude is proportional to the size of the cells.[21]

The nanopore was born by merging the Coulter-counter principle with the single-channel electrophysiology. The single-current recording technique has originally been developed to characterize protein ion channels embedded in natural lipid bilayer membranes.[22,23] Thus, in this new sensing platform, the aperture was downsized from millimeter to nanometer and the target particles became individual biomolecules instead of cells. One of the first nanopore papers that reported single-molecule detection was published in PNAS by Kasianowicz *et al.* in 1996. They reported detection of single-stranded RNA and DNA molecules through a 2.6-nm diameter biological pore.[24] Five years later, in 2001, Li *et al* took the critical step towards the development of synthetic nanopores by fabrication of the first solid-state nanopore using argon ion-beam sputtering.[25] These were the starting points of a journey towards DNA sequencing using nanopores.

1.4.2 Types of nanopores

As mentioned earlier and illustrated in Figure 1-3, nanopore sensors are generally divided into two main categories: *biological* and *solid-state*.[17] They both are able to detect biological and chemical analytes at the single-molecule level.

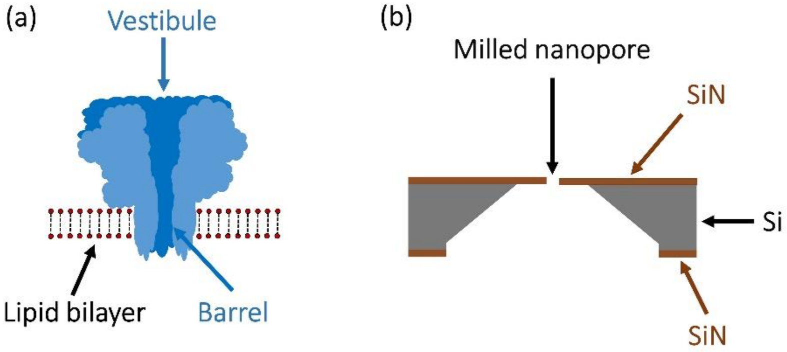

Figure 1-3 Cross-sectional view of **(a)** a biological nanopore spanning a lipid bilayer membrane and **(b)** a solid-state nanopore fabricated in a thin insulating membrane, Silicon nitride commonly used. The schematic is adapted from Reference[26].

Biological nanopores, also known as transmembrane protein channels, are usually inserted into a substrate, such as planar lipid bilayers, liposomes, or other polymer films. However, among all, α-hemolysin has been the most commonly used biological nanopore since 1996.[27] MspA (Mycobacterium smegmatis) is a powerful biological nanopore with a small pore diameter (1.2 nm) and thin (0.5 nm) thus it can improve the signal resolution.[28] The third type of the biological pore is phi29, which belongs to a family related to bacteriophages. This type of nanopore has slightly larger entrance (3.6 nm) through which the successful passage of double-strand DNA was reported.[29]

Solid-state nanopore, as the other counterpart, was first fabricated on Silicon nitride (SiN) membrane using ion beam sculpting in 2001.[25] Two years later, Dekker's group reported fabrication of nanopores with single nanometer precision on a silicon dioxide (SiO_2) wafer using focused electron beam in a transmission electron microscope.[30] Meanwhile, fabrication of solid-state nanopores using different techniques with a variety of materials, including organic polymer[31], glass[32,33], graphene[34], single-walled carbon nanotubes (SWCNT)[35,36], boron nitride[37], and hafnium oxide[38] have been reported. Solid-state nanopore, as the core of this work, is discussed furthermore in Section 1.5.

1.4.3 Principle of a nanopore

As schematically illustrated in Figure 1-4, a typical nanopore device is identical to the Coulter-counting concept and consists of a single nanoscale aperture either embedded in a biological membrane or fabricated in an insulating membrane bathed in conductive electrolyte solution.

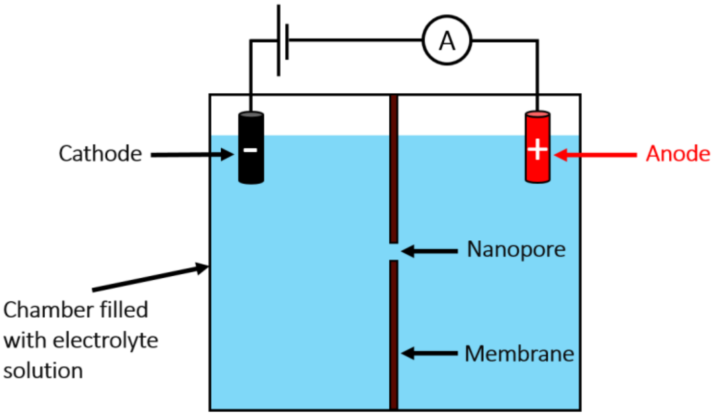

Figure 1-4 Schematic of a typical nanopore sensor setup. The membrane accommodates the nanopore and divides the chamber containing electrolyte solution in to two compartments. A pair of electrodes (cathode and anode) is immersed across the membrane. Under a bias voltage between the two electrodes, electrolyte ions move through the nanopore. The schematic is adapted from Reference[39].

Electrodes are also immersed on each side of the pore. An ionic current signal is generated when a bias voltage is applied between the electrodes astride the membrane.[40,41]

Typically, silver/silver chloride electrodes (Ag/AgCl) are used in a nanopore setup as they are non-polarizable and cause no capacitive current at the interface of electrolyte with them. When an electric potential difference is applied across the pore, the following two reversible electrochemical reactions occur at the electrodes[41], shown in Figure 1-5(a):

$$\textbf{At the anode: } \mathrm{Ag} + \mathrm{Cl}^{-} \rightarrow \mathrm{AgCl} + \mathrm{e}^{-} \tag{1.4}$$

$$\textbf{At the cathode: } \mathrm{AgCl} + \mathrm{e}^{-} \rightarrow \mathrm{Ag} + \mathrm{Cl}^{-}$$

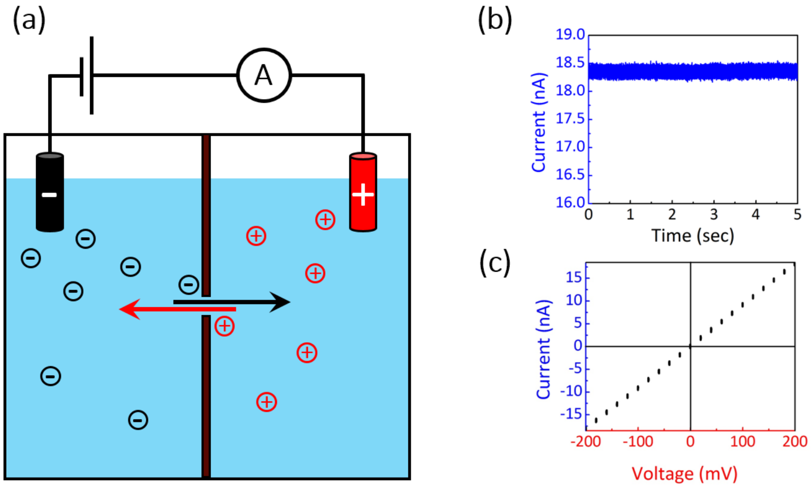

Figure 1-5 **(a)** Application of a bias voltage results in electrochemical reactions at the electrodes and moving electrolyte ions through the nanopore, thereby **(b)** a steady direct current (DC) for an open pore is generated and determined as the baseline current. **(c)** The size of a pore is estimated by its I-V characteristics. The baseline current and I-V plots are for a 15.5 nm pore in an integrated nanopore-microfluidic device. The schematic is adapted from Reference[41].

At the positive electrode, the anode (+), Ag reacts with Cl^{-} ions and produce AgCl with an electron which migrates through the wire to the measurement electronics. This produces current and generates a charge imbalance resulting in cation migration towards the membrane. Depending on the type of the electrolyte solution, the cation typically can be Na^{+}, K^{+} or Li^{+}ion.[41]

At the negative electrode, the cathode (-), the reverse reaction happens, an electron is used from the circuit while the released chloride ion migrates towards the membrane. This process is extremely fast and as shown in Figure 1-5(b) results in a steady-state ionic current (open pore current) which is generated by an infinite exchange of ions. However, at larger bias values (above 1 V), water and other species are more likely to be electrochemically active, resulting in nonlinear electrochemical processes and significant pH instability. Therefore, nanopore experiments are normally performed at biases below +/- 1 V and the nanopore behaves as ideal ohmic resistor, resulting in a linear current–voltage (I-V) response. As presented in Figure 1-5(c), nanopore conductance and also its size is calculated by fitting a linear I-V curve.[41] This will be discussed more further in Chapter 2.

As shown in Figure 1-6, when individual molecules, such as DNA or protein, pass electrophoretically (translocate) through the nanopore, consecutive disruptions in the current signal are observed. Statistical analysis on the blockage amplitudes and durations provide information about length and conformation of the translocated molecules.[42] The dwell time (t_{dwell}) is the amount of time for a molecule to fully translocate through the nanopore. The blockage amplitude (blockage depth, ΔI) is the difference between open pore current and the blockage current.[41]

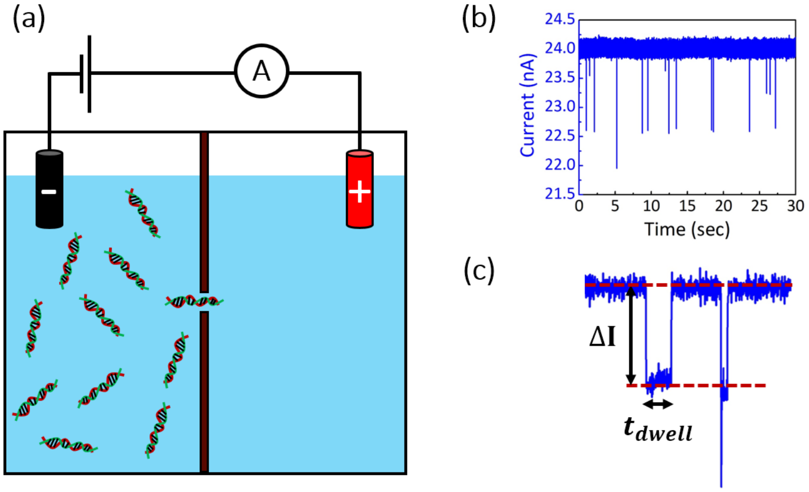

Figure 1-6 **(a)** The individual molecules start passing the nanopore under a constant applied potential. **(b)** The translocation of molecules detected by interval interuption in the basline current. **(c)** Dwell time and blockage amplitude are two important parameters to obtain information about the translocated biomolecules. The current traces shown in **(b)** and **(c)** are translocation of 10kbp dsDNA through a 15.5–nm pore in an integrated nanopore-microfluidic device. The schematic is adapted from Reference[41].

Figure 1-7 shows typical current blockades characteristics of 10kbp dsDNA translocated through a 15.5-nm solid-state nanopore.

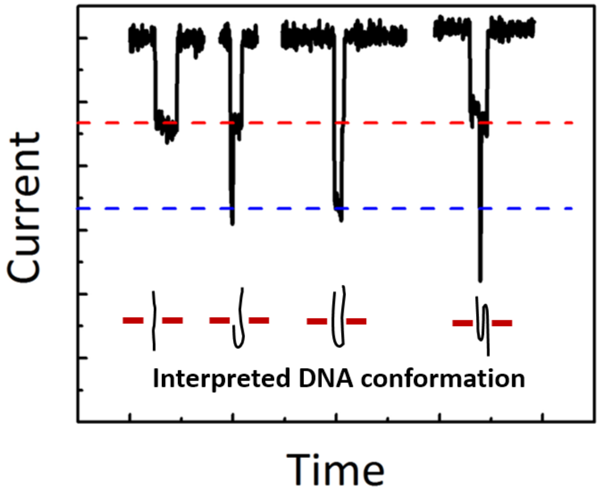

Figure 1-7 Various conformations of 10 kbp dsDNA in 3.6 M LiCl solution with pH 10 translocated through a 15.5-nm solid-state nanopore in an integrated nanopore-microfluidic device, under an applied potential difference of 200 mV. Ionic current traces were sampled at 250 kHz, low-pass filtered at 100 kHz using a 4-pole Bessel filter and multiplied by -1 for visualization. **From left to right, respectively:** folded, half-folded, fully folded and knotted dsDNA molecules.

In brief, the idea of nanopore sensors is that individual nucleotides can be differentiated with characteristic changes in the trans-membrane currents and dwell times. The current baseline stays sustained, when the molecule is not in the pore. Once a molecule enters the nanopore, the ions fluxes are reduced and these blockages are measured. Since these interruptions typically result from interactions between the nanopore and the molecule, it is expected that nanopore sensors are able to detect and quantify very subtle differences, such as the presence and absence of methylation in DNA.[43,44]

1.5 Solid-state nanopores: Candidate for integrated lab-on-a-chip devices

Biological nanopores have shown to be very useful for a range of exciting experiments including ssDNA sequencing. Biological nanopores have high-reproducibility, well-defined size and structure. Due to their biological nature, they can be easily modified to change the amino acid residue at a specific site enhancing interactions with the translocating polymer.[17] However, biological nanopores suffer from several disadvantages such as instability, if changes occur in external parameters (pH, temperature, salt concentration, and mechanical stress), fixed size, the fragility of their embedding lipid bilayer and the waiting time for single-channel reconstitution.[45]

With the development of micro- and nanofabrication techniques, solid-state nanopores have attracted increasing attention. They have a number of distinct advantages over their biological counterparts, such as thermal, chemical, and mechanical stability, size tunability, and their potential for integration within lab-on-a-chip technologies.[46–52] In addition, arrays of them can be mass produced using conventional semiconductor processes which can further improve the cost and scale of analysis.[53]

Silicon-based materials, including silicon nitride (SiN) and silicon oxide (SiO_2) films, have been widely used as the membrane because of their low mechanical stress and high chemical stability.[54,55] Silicon nitride deposited by low-pressure chemical vapour deposition (LPCVD)[56] is an excellent insulator with extremely high resistivity (10^{16} Ω.cm), allowing for the discrimination of low ionic currents (tens of picoamperes) through individual nanopores milled in such membranes. Additionally, the coefficients of thermal expansion for silicon and silicon nitride are similar, allowing the deposition of nitride layers on a silicon substrate at high temperature without large residual stresses at room temperature. Such characteristics make SiN-based nanopores useful for a wide variety of experiments. Several research groups have been studying biomolecule transportation and interaction using solid-state nanopores including nucleic acid analysis[40], single molecule force and mass spectroscopy[57–60], protein detection[61], molecule separation[62], virus translocation[63] and disease diagnosis[64].

1.5.1 Fabrication methods of silicon-based nanopores

1.5.1.1 Energetic particle beams

Solid-state nanopores are commonly fabricated by milling a nanometer-scale aperture in a thin silicon nitride membrane (5-30 nm) using a beam of energetic particles. The fabrication methods are produced either by milling the substrate using a focused ion beam (FIB)[65] or sputtering the surface with electron beam irradiation in a transmission electron microscope (TEM)[30]. The silicon membrane is typically suspended on a rigid supporting silicon substrate. The principles of both systems are similar and rely on a set of apertures and lenses to focus a beam of charged particles onto the membrane. It is also possible to image the pore immediately after the fabrication by these techniques. The nanopores fabricated by energetic particles beams have been successful in molecular sensing.[66]

However, the major downsides of these methods are time-consuming, requiring sophisticated machinery and skilled users. The chip often requires a cleaning in order to remove any left-over residue, which inevitably introduces handling risk and wetting issues during the cleaning and when transitioning into electrolyte for biosensing experiments. The size resolution of fabricated pores is ~2 nm using TEM and ~5 nm for FIB with helium ions. Therefore, some treatments are required for size tuning the fabricated pores.[25,67] These nanopores are also poorly suited for integration within microfluidic environments. The *ex-situ* fabrication, makes the correct alignment during the device assembly within microfluidics very low-yield.[50,51] All these drawbacks make scaling such a technology up to an industrial level and commercialization very challenging

Although nanopore fabrication using energetic particle beams have been the benchmark for almost 15 years, there is an overwhelming urge to find a cheap, simple and fast fabrication technique available for a wider research community.

1.5.1.2 Controlled BreakDown (CBD)

Recently, a novel technique was developed to make the entire process of nanopore fabrication and the size tuning automated, fast, simple, precise and much cheaper.[68–70] The approach relies on the phenomenon of dielectric breakdown of a thin silicon nitride (SiN) membrane.[68]

In brief, an individual nanopore, with sub-nm precision, is fabricated directly in electrolyte by applying a constant potential difference ΔV of moderate strength across a thin SiN membrane (d=5 to 30-nm thick).[70] The potential difference produces an electric field $\mathrm{E} = \frac{\Delta \mathrm{V}}{\mathrm{d}}$, in the range of 0.5-1 V/nm. A leakage current $I_{leakage}$ (tens of nanoamperes) is then observed though the membrane in response to this high electric field. It is believed that the ions in the electrolyte transfer charges that undergo trap-assisted tunneling through the membrane.[68] Accumulation of these charge traps (structural defects) form a localized conductive path results in a sudden irreversible increase in $I_{leakage}$, indicating that an individual nanopore has been formed. A feedback control mechanism is also used to terminate the applied potential immediately when the current exceeds a predetermined threshold, I_{cutoff}. This produces automated and reproducible fabrication of nanopores[70]. Following the fabrication, the nanopore size is precisely tuned by applying square short pulses in moderate electric field.[69,71] Due to its simplicity, the nanopore fabrication method by CBD can easily be accommodated within a range of fluidic environments.[72,73]

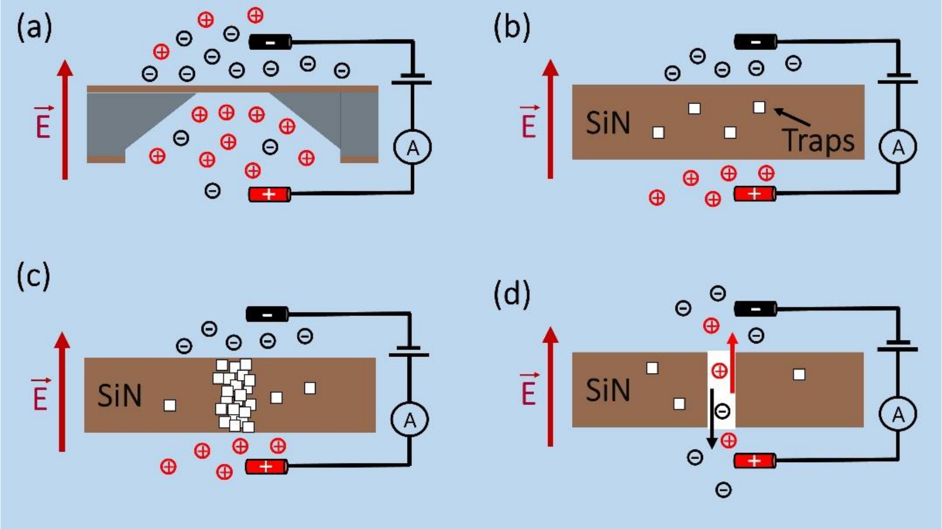

Figure 1-8 **(a)** Application of a constant potential difference to the silicon chip produces an electric field inside the silicon nitride membrane and charges the interfaces with opposite ions. **(b)** Trap-assisted tunneling through the membrane creates leakage current **(c)** Accumulation of charge traps (defects) results in a dielectric breakdown event. **(d)** A conductive path, a nanopore, is formed. The scheme is not to scale and adapted from Reference[68].

1.5.2 Background noise in solid-state nanopores

Background noise sources in solid-state nanopore experiments can be divided into two extreme regimes of interest, high-frequency and low-frequency spectra.[74] At low frequencies, below 10 kHz, flicker noise (pink), thermal and shot noise (white) are prominent whereas at higher frequencies dielectric loss (blue) and capacitance (purple) noise dominate. Noise analysis of experimental data centres on the Fourier transformation of the electrical trace to form a power spectral density (PSD)[74,75], schematically depicted in Figure 1-9.

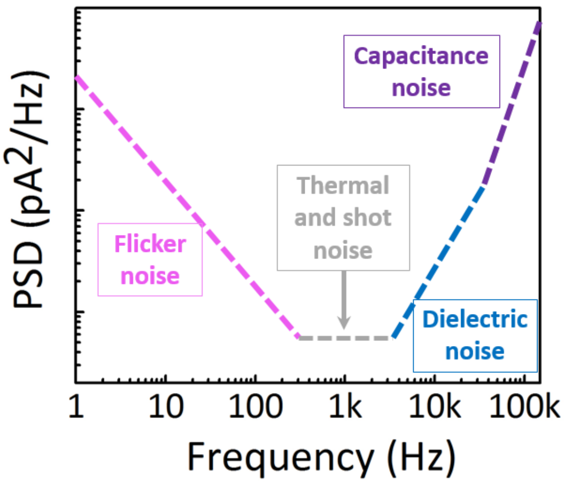

Figure 1-9 Shematic depicts the dominant sources of noise in the PSD of the ionic current of a solid-state nanopore as a function of frequency. The PSD is given by Equation 1.4. The plot is adapted from Reference[74].

Each contributor to the noise in a nanopore device has a distinct frequency dependence. Thereby, the total current noise in the PSD, S_I, can be broken down into four parts and fitted with a polynomial of the form[74]:

$$S_I = \frac{a_0}{f} + a_1 + a_2 f + a_3 f^2 \tag{1.4}$$

The terms a_0, a_1, a_2, a_3 respectively represent the contributions from the flicker, thermal, dielectric, and capacitance noises, and f is the frequency in Hertz. In the following sections, these noise sources are briefly described. However, during the course of this study, one of the objectives was noise reduction in the high frequency regime (dielectric and capacitive).

1.5.2.1 Flicker noise

A low-frequency fluctuation, with a 1/f dependence, is observed in the nanopore ionic current when an electric potential is applied across the membrane. This current is known as **flicker noise** and largely dominates **thermal** and **shot noise** in the low-frequency regime, especially for the solid-state nanopore.[74] The ion flux and variability in ion flux through the nanopore are normally two important factors that affect the magnitude of the 1/f slope. Therefore, under applied voltage contaminated nanopores have increased 1/f noise and the slope is more negative.[41] The

PSD of the flicker noise is proportional to the square of the nanopore current, the frequency and depends on a constant β, which is typically equal to one[74]:

$$\mathrm{S}_{\mathrm{flicker}} \sim \frac{I^2}{f^{\beta}} \quad (1.5)$$

Some surface modifications, such as atomic layer deposition[67], plasma[76] and piranha treatment[77] to reduce hydrophobicity effects, or "zapping" the pore with short pulses (<2 s) in moderate electrical potential (3-5 V)[69] can minimize the magnitude of flicker noise. Despite extensive investigation, the physics behind flicker noise is not fully understood.

1.5.2.2 Thermal noise

The baseline noise of a nanopore setup is triggered by **thermal noise** of the feedback resistor in circuitry of the current amplifier and/or the nanopore resistance. Typically, thermal fluctuations of charge carriers inside a conductive medium generate such a noise in the nanopore. At equilibrium, the PSD of the thermal noise is simply given by[78],

$$\mathrm{S}_{\mathrm{thermal}} = \frac{4\mathrm{kT}}{\mathrm{R}} \quad (1.6)$$

where k is the Boltzmann constant, T is the absolute temperature, and R is sum of the resistance of the nanopore and the feedback resistor. Thus, a small size nanopore, with higher resistance, and by cooling down the amplifier circuitry result in lower the level of thermal noise.

1.5.2.3 Shot Noise

In an electrical conducting medium, shot noise arises by random fluctuations in the number of ions inside the pore. The PSD of the shot noise for a nanopore is given by[74],

$$\mathrm{S}_{\mathrm{shot}} = 2\mathrm{Iq} \quad (1.7)$$

In this equation, I is the average of current and q is the effective charge of the charge carrier (for electrons, $q = -1.6 \times 10^{-19}$ C).

1.5.2.4 Dielectric noise

Generally dielectric materials are not ideal insulators. Therefore, upon application of the biased voltage to a nanopore, current leaks through the membrane and its supporting structure. The dielectric loss and the heat generation result in additional noise which is known as **dielectric noise**. The PSD of this noise is written as[74]:

$$S_{\mathrm{dielectric}} = 8\pi kTDC_{\mathrm{chip}}f \qquad (1.8)$$

In Equation 1.8, k is the Boltzmann constant, T is the absolute temperature, D is the dielectric loss, f is the frequency, and C_{chip} is the capacitance of the nanopore membrane and its supporting structure.

1.5.2.5 Input capacitance noise

Nanopore sensing relies on completing electrochemical reactions resulting in ions moving through the nanopore and producing a measured DC current signal. However, a parallel-plate electrolytic capacitor is formed by the lineup of ions and counterions astride the membrane. This parasitic capacitance produces noise fluctuations that increase with bandwidth and can severely limit the time resolution in biomolecular sensing experiments.[49] This results in an everlasting experimental battle between signal quality and so needed time resolution. The PSD of the current for the input **capacitance noise** is written as[74]:

$$S_{\mathrm{capacitance}} = (2\pi fC_{\mathrm{total}})^2 e_n^2 \qquad (1.9)$$

In Equation 1.9, C_{total} is the sum of several capacitances, including the capacitance of the membrane, stray capacitances that can be present in any wiring, and the input capacitance by the amplifier. The quantity e_n is the equivalent voltage noise at the op-amp input.

A common way to reduce the effect of such noise is decreasing the bandwidth of the measurements by attenuating the high-frequency components of the current signal. This is achieved using analog or digital low-pass filters. However, this results in degradation of the measurement time resolution which distorts the signal and masks structural information about the molecule of interest.

An study[76] has indicated that the capacitance of the nanopore membrane has the largest contribution in high-frequency noise regime. Some alternatives to reduce the amount of this contribution is using a material with a smaller capacitance to fabricate the nanopore or designing a chip with a smaller area exposed to the electrolyte. For this purpose, researchers have developed some approaches to improve SNR in the high-frequency spectrum by reducing the capacitance of the nanopore substrate, such as PDMS painting[76], passivation by photodefinable PDMS[77] or polyimide coating on the surface of a chip[52], and transfer printing of suspended membrane within microfluidic channels.[51]

1.6 Capture process in a solid-state nanopore

The throughput of a nanopore sensor is determined by the rate at which molecules of interest arrive and thread into the pore. Therefore, studies and investigations on the capturing process have received significant attention.[41]

A hypothetical hemisphere of radius r* outside of the nanopore is defined as the capture radius. In the purely diffusive motion, the negatively charged molecule (DNA) is far away from the pore mouth (r*<<r) and diffuses randomly in the solution due to the Brownian motion. Therefore, the capture is limited by the time that DNA travels to the pore mouth. In the drift motion, the DNA molecule is at a distance of r*~r. When the molecule approaches the nanopore, the effect of the electric field becomes dominant compared to the diffusive forces. The electric field only extends a few micrometers outside of the nanopore.[78,79]

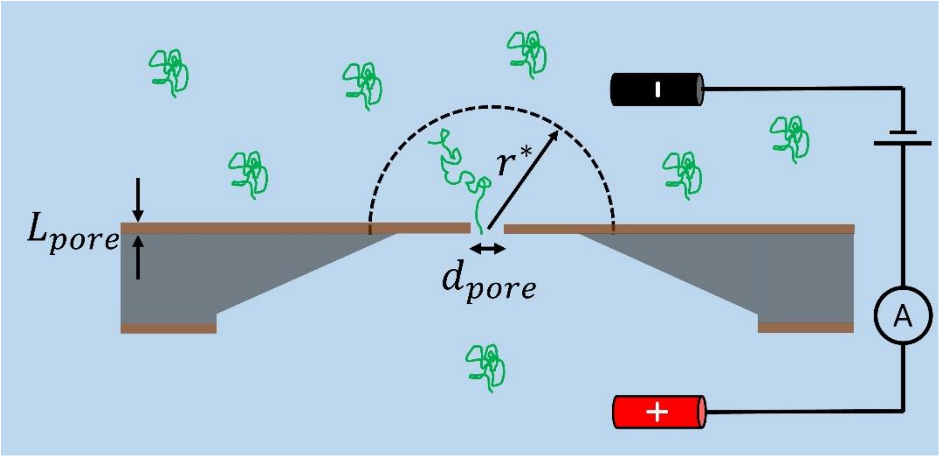

Figure 1-10 Scheme (not to scale) of biomolecules (e.g. DNA) capture at a solid-state nanopore while an electric potential is applied. The radius of hypothetical hemisphere outside of the nanopore is defined as the capture radius, r*. At a distance far away the pore (r*<<r), the electric field is negligible and the molecule motion is merely diffusive. At distances smaller than r*, the electric potential is large enough to drive the molecule towards the pore mouth. The schematic is adapted from Reference[78].

Within the capture radius, the DNA molecule diffuses no longer freely and instead it is driven towards the nanopore by a drift velocity[78]:

$$\mathrm{v_{ep}} = \mu_{ep} \nabla V(r) \tag{1.10}$$

In Equation 1.10, μ_{ep} is the electrophoretic mobility of molecule, and V(r) is the potential at a distance of r from the nanopore and defines the electric field profile in the system. V(r) is highly dependent on the nanopore geometry and given by[78],

$$\mathrm{V(r)} = \left(\frac{d_{pore}^2}{8L_{pore}r}\right)\Delta V \tag{1.11}$$

In Equation 1.11, ΔV is the potential drop across the pore, d_{pore} is the nanopore diameter, and L_{pore} is the nanopore thickness. It follows that the electric field is relatively stronger at close distance to the pore mouth (r*~ r) and creates an electrophoretic trap for the DNA molecule.

The distance r* can be estimated from the relationship between the electrophoretic speed, v_{ep}, and the diffusional speed of the molecule, v_{diff}. A term for v_{diff} can be approximated from the diffusion time, t_{diff}, required for the molecule to travel from the distance r to the pore entrance[78]:

$$v_{diff} \sim \frac{r}{t_{diff}} \sim \frac{r}{\frac{r^2}{D}} = \frac{D}{r} \qquad (1.12)$$

In this equation, D is the diffusion coefficient and t_{diff} is obtained by the Brownian motion. As earlier written in Equation 1.10, v_{ep} is defined by[78],

$$v_{ep} = -\mu_{ep} E(r) = -\mu_{ep} \frac{V(r)}{r} \qquad (1.13)$$

While the molecule approaches the nanopore, at some point v_{diff} is comparable to v_{ep}, thereby the following expression can be written for capture radius[78,80]:

$$r^* = \frac{\mu_{ep} d_{pore}^2}{8DL_{pore}} \Delta V \qquad (1.14)$$

DNA translocation is strongly governed by the applied potential as well as the nanopore dimensions. Typically, the molecule detection and the capture rate of a nanopore are predominately diffusion limited. Therefore, the capture volume is much smaller than the sample volume. To rectify this ratio, several approaches have been reported to enhance the rate at which nucleic acids are captured by a nanopore, such as increasing the applied voltage[81], introducing a trans-membrane salt gradient[78], modifying the surface charge of the nanopore, and using single-molecule dielectrophoretic trapping[82].

1.7 Microfluidics: Laboratory on a chip

Microfluidics have emerged as a distinct field in life science and medicine research for the last two decades because of the development in soft lithography[83] and large scale integration[84]. These advancements have improved rapid prototyping at very low cost and enhanced the complexity of experiments that can be performed on a single chip. This technology is characterized by fluidic channels with a linear dimension on the order of tens to hundreds of micrometers that can manipulate and control small volume of fluids (typically from micro- to nanoliters).

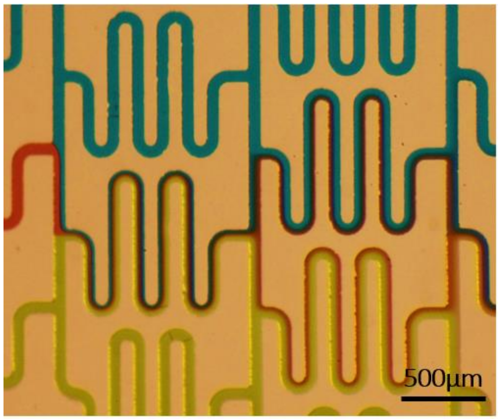

Figure 1-11 Typical PDMS-microfluidic channels, filled with food coloring dyes, to show the laminar flow conditions at the microscale. The device was designed by Jason Riordon[85], former PhD candidate at the time in the Godin lab.

The microfluidic devices are powerful tools for handling, processing, sorting and preparation of biomolecules such as cells, nucleic acids, proteins or neurons. They have already been applied to cell[86] and protein separation[87], polymerase chain reaction (PCR)[88], immunoassay[89], and cellular analysis[90]. They can offer portable, cheap, and single-use devices, soon to be a replacement of expensive and sophisticated laboratory equipment in health care facilities.[91]

Several dimensionless numbers can be used to quantify the dominant fluid mechanical effects that govern fluidic behaviour within microchannels under various conditions such as flow rates, size of the analyte, density, and channel configuration. Among them, Reynolds and Peclet are the two numbers which characterize fluid flow and how analytes act within the fluid.[92,93]

The Reynolds number (Re) is often used to determine the degree to which fluid flow can be characterized as being mainly laminar or turbulent. This number is the ratio of inertial force to viscous force and given by[92],

$$\mathrm{Re} = \frac{v l \rho}{\eta} \tag{1.15}$$

Where ν the fluid velocity, l is a characteristic channel dimension such as channel width, ρ is the fluidic density and η is the fluid viscosity. At low Reynolds numbers (Re<2000), fluid flow is laminar while at high numbers (Re>2000), fluid flow is turbulent.[92]

Pressure-driven and laminar flow has a parabolic velocity profile, as schematically shown in Figure 1-12. The highest (fastest) fluid velocities occur in the middle of the channel whereas the slowest velocities are along the channel walls. The fluid velocity is zero at the walls, so-called no-slip boundary condition. [93]

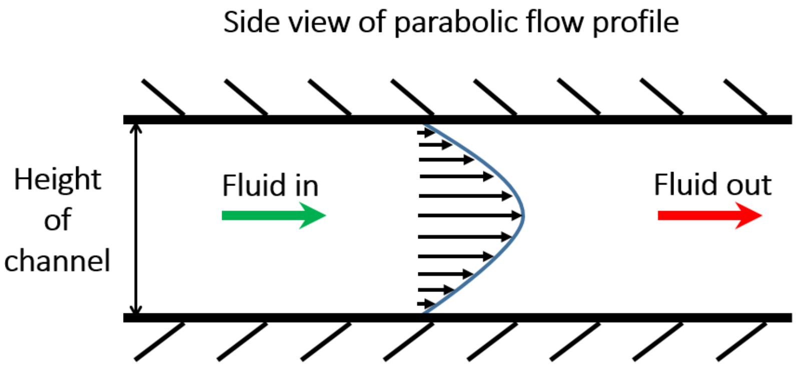

Figure 1-12 Laminar flow within a microfluidic channel has a parabolic flow profile

In microfluidics, turbulence is hard to be achieved unless the applied pressure is extremely high that results in very high fluid velocity. Therefore, the flow is always laminar in microfluidic devices (*l* is in the order of micrometers).[92] For instance the Reynolds number for a microfluidic channel with $l \approx 100$ µm filled with water ($\frac{\eta}{\rho} = 10^{-6}$ m^2/s) and fluid velocity of $\nu \approx 1$ mm/s, leads to a small number, Re ≈ 0.1. This concept of laminar flow needs more attention when the microfluidic devices are utilized to study sorting and fractionation of different size particles.

The Peclet number (Pe) quantifies the transport and mixing of fluids.[92] This number is the ratio of convection rate to diffusion rate and given by[92]:

$$\mathrm{Pe} = \frac{vl}{D} \tag{1.16}$$

In this equation, D is the diffusion constant, ν the fluid velocity, and *l* a characteristic channel dimension such as channel width. The diffusion coefficient is written as follows[93]:

$$\mathrm{D} = \frac{k_B T}{6\pi r \eta} \tag{1.17}$$

Where k_B is Boltzmann's constant, T is the absolute temperature, η is the fluid viscosity and r is the analyte radius. This means the low Reynolds number in the world of microfluidics also forces mixing to happen by diffusion alone, which causes quite long mixing times.[92]

1.8 Microvalves: "The traffic light in microfluidics"

In the late twentieth century, the design of transistors with highly engineered performance properties, including size, speed, power, and gain was allowed by knowledge development in semiconductor physics. Intensive research and exploration are being conducted in the field of microfluidic devices to launch a similar revolution in biophysics and biochemistry.[94] However, the successful miniaturization and commercialization of fully integrated microfluidic circuits have been delayed due to the lack of reliable microfluidic components. One of these fundamental components are microvalves, used for fluidic manipulation.[95] The microvalves, according to the source of actuation, are categorized into five different groups; **1)** *active – mechanical* (Magnetic, Electric, Piezoelectric, and Thermal), **2)** *active –non-mechanical* (Electrochemical, Phase change, and Rheological), **3)** *active – external* (Modular and Pneumatic), **4)** passive – mechanical (Flap, Membrane, Spherical ball, In-line mobile structure) and **5)** *passive – non-mechanical* (Diffuser and Capillary).

Pneumatic, or in-line, microvalves were first introduced by Quake[96]. Typically, it consists of two layers made of PDMS rapid prototyping and permanently bonded together in a perpendicular crossed architecture. The pneumatic channel (control/valve channel) is deformed under pressure to pinch off the flow of fluids in an in-line microchannel (flow channel). The separating membrane can be deformed either upwards (push-up valves) or downwards (push-down valves), depending on which channel is pressurized. Furthermore, a series of valves in a single layer with different dimensions (length and width) can be selectively actuated, because each has a different threshold of hydraulic pressure necessary for actuation.[97]

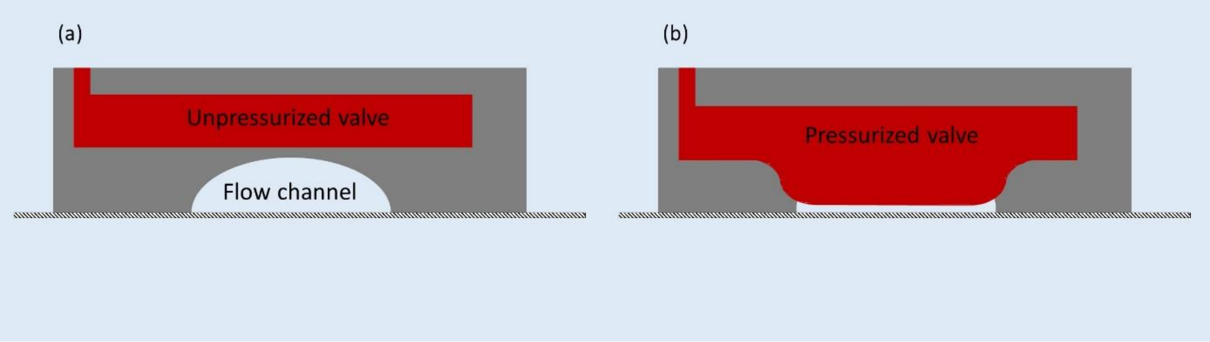

Figure 1-13 Scheme (not to scale) of push-down valves **(a)** A control channel (valve) passes over the flow channel. **(b)** Pneumatic pressurized valve flattens the separating membrane downwards and compresses the flow channel to create a seal. The schematic is adapted from Reference[97].

These elastomeric valves have proven to be valuable to solve the macroscopic–microfluidic interface problem for highly parallel analysis on a single chip.[98] The concept of these pneumatically actuated microvalves was also utilized for sorting and trapping particles and single cells.[99]

1.9 Motivation to integrate nanopore within microfluidic networks

Typically, a solid-state nanopore setup consists of two-half fluidic cells, as shown in Figure 1-14 (a). A key feature of the cell is its ability to form a very tight seal around the chip, with the nanopore as the only path for ionic current to flow between electrolyte reservoirs. The cells are made of polytetrafluoroethylene (PTFE) as it is chemically inert and resistant, permitting thorough cleaning and decontamination between experiments. However, this configuration is not well-suited for sample processing and manipulation. This setup is also limited to one nanopore per mounted silicon chip.

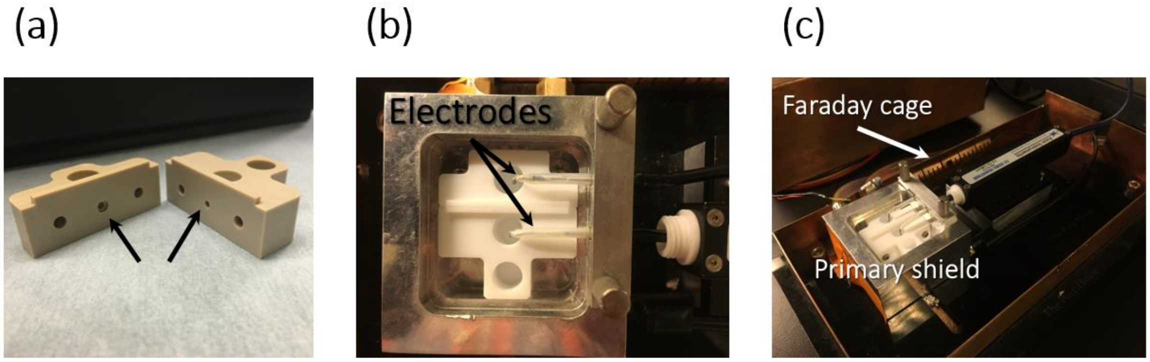

Figure 1-14 Conventional solid-state nanopore setup **(a)** A silicon chip is tightly mounted between two-half marcroscopic fluid cells. The location of the chip is pointed by the arrows **(b)** The assembled cell is then placed in a block. The electrodes are submerged in each reservoir filled with solution of interest, while a cover (not shown) completes the cage. **(c)** The electrodes are then connected to the related electronic instrument to perform either nanopore fabrication or biomolecular sensing experiment. In this image, the electrodes are connected to a current-voltage converter (the Axopatch headstage) inside a secondary Faraday cage.

Recently, there has been an increasing interest to integrate advanced biosensors into lab-on-a-chip systems by introducing microfluidics. Nanopore sensors have shown great promise in the biosensing domain, specifically as the next generation sequencing.[17] On the other hand, microfluidic systems have several intrinsic properties including portability, versatility in design, low reagents consumption, efficient mixing and reactions, and in-parallel detection of multiple sample. Since the power of microfluidic devices is compelling, such an integration will define a unique path toward brighter future for both nanopore sensors and microfluidics.

Therefore, a few research groups have explored the possibility of integrating of different types of solid-state nanopore within various microfluidic networks. Here is a brief review of some selected articles and the findings;

In 2008, the Jacobson group reported an integrated nanopore-microfluidic device in two individual articles.[46,47] The device was formed by sandwiching track-etched conical nanopores in a polyethylene terephthalate (PET) membrane between two polydimethylsiloxane (PDMS) microfluidic channels. They first studied the ion depletion and sample stacking using fluorescence images.[47] Shortly after, they reported trapping biological (bacterial cells) and non-biological (polystyrene microspheres) particles for various applied potentials from ±10 V to ±100 V and exploring frequencies.[46]

In 2012, Nelson *et al* used an integrated nanopore for single molecule detection and cell transfection.[50] The nanopore was milled in a silicon nitride membrane using TEM. The paper consists of two parts: trap and identify two proteins (bovine serum albumin and streptavidin), and manipulate proteins secreted from single cell transfection. They positioned a breast cancer cell, encapsulated in hydrogel next to the nanopore using optical tweezers, and transfected it by electroporation. Such an integrated platform with optical tweezers allows the de-convolution of a single cell secretome from the bulk populations.

In 2013, the Karnik group published a paper about integration of solid-state nanopores in microfluidic networks via transfer printing of suspended membranes.[51] The nanopore was fabricated by FIB in a silicon nitride membrane. To facilitate transferring the membrane to the PDMS pieces, the edge of the membrane was partially cut with FIB after the nanopore formation. Their results mainly highlighted the reduction of noise and signal quality enhancement owing to significant reduction in membrane capacitance. The functionality of the device was verified by detecting double-stranded DNA translocation. They concluded their findings is a significant step in the direction of rapid and portable biomolecule analysis.

The Keyser group reported the first example of multichannel ionic current detection of single molecules with 12 out of 16 glass nanopores embedded in PDMS grooves.[100] The glass nanopores were made of quartz capillaries and formed using a laser assisted capillary puller. The paper highlights the feasibility of multiplexed sensing to increase statistics on data acquisition in a cost-effective way. Each device costs less than $20. The device detected double-stranded DNA through 10 channels. As another proof-of-concept, DNA origami nanostructures were trapped to form hybrid nanopores.

Another application of glass nanopores for single molecule detection was reported by the groups of Albrecht and Edel in 2014[101]. They integrated two glass nanopores into a segmented flow microfluidic device to enhance the functionality of nanopore sensors. Although the viability of fabricated devices for experiments was around 25%, they believed the presented device would provide the platform for the development of integrated devices in which the injection and extraction could be controlled at the molecular level. The experiment can potentially be extended to preparation and detection of low-concentrated biosamples within the droplets as isolated microreators.

Most recently, Goto *et al* [52] demonstrated the fabrication of an individual nanopore using dielectric breakdown by coating the SiN membrane with a bead layer. The temporal resolution of single-molecule detection was improved. Also the reduction in high frequency noise was achieved by adding a polyimide layer to the membrane.[52]

1.10 Outline of the thesis – My research journey

1.10.1 Objectives

The objectives of this study were to design, implementation and development of integrated nanopore-microfluidic devices with various architectures for single-molecule detection.

The conventional nanopore setup (Figure 1-14(a)) generally suffers from limits such as sample preparation, manipulation and processing. Accommodating arrays of many nanopores which allows high-throughput data acquisition is unfeasible within this setup.

On the other hand, several approaches have been investigated to reduce capacitance of the silicon chip and improve significantly SNR of nanopore sensors in the high-frequency regime including PDMS painting[76], coating with polyimide[52] or removing entirely the supporting silicon chip[51].

Controlled breakdown (CBD) facilitates the nanopore fabrication *in situ* within the range of various fluidic configurations.[68] This breakthrough with our knowledge about microfluidic devices forms the main objectives of this study as follows:

1) Integrate solid-state nanopores fabricated by controlled breakdown (CBD) within arrays of various microfluidic networks.

2) Develop a design to reduce the capacitance noise in the high-frequency regime.

3) Develop an approach to utilize the microfluidic characteristics in fluid and electric manipulation

1.10.2 Chapter 2 – Experimental setup & Methods

Chapter 2 represents the information related to microfabrication, designs of the devices, fabrication of master molds, and assembly steps of various devices (single and multi-layer soft lithography). Also different parts of the experimental setup (Faraday cage, fluid setup), and detailed information about nanopore fabrication are presented.

Further discussion about characteristics of the fabricated nanopores by CBD, estimation of their sizes and blockage levels, and the approach to reduce the high frequency noise are presented at the end of this chapter.

1.10.2 Chapter 3 – CBD paved the way for the integration

Nanopore fabrication by controlled breakdown (CBD) was a breakthrough and due to the simplicity adapts itself very well to the integration within microfluidic environment. We were able to integrate a 5×1 nanopore array fabricated by controlled breakdown technique within microfluidic devices. To the best of our knowledge, this device was the first in which nanopore fabrication was done in situ after embedding the silicon nitride within microfluidic channels.

We were also able to reduce the capacitance noise by inclusion of microvias, small opening which limited the exposed area of the membrane to the solution. To validate the functionality of the devices, double-stranded DNA and human α-thrombin were detected.

These findings, presented entirely in Chapter 3, were published as a **Technical Innovation** article in *Lab on a Chip*.[72]

1.10.3 Chapter 4 – Access manipulation with microvalves

Although the first generation of the integrated nanopore-microfluidic device was a big step forward, the configuration had some drawbacks. The device previously presented consisted of five independent channels which required their own fluidic and electrical access. Indeed, the large number of fluidic and electronic connections made around the device crowded. In an effort to mitigate this issue, the use of on-chip pneumatic microvalves, which also provides new opportunities for fluidic manipulation before and during sensing was designed in the second generation of the device. Inclusion of the microvalves allows us to precisely manipulate fluidic and electrical access within connected flow channels and the respective nanopore sensors. It is shown that pressure-actuated valves provide high electrical resistance. Therefore, the fabrication of new pores or enlarging fabricated pores, and performing biomolecule sensing is feasible without any cross talk between the nanopores. In addition, using partially-actuated microvalves allows to reduce the fluid flow, potentially decrease the sample loss, while still allowing ionic current measurements.

Chapter 4 is comprised of these findings and consists of a published manuscript as a **Communications** article in *Small*.[73]

1.10.4 Chapter 5 – Conclusion and Future directions

This chapter is a summary and conclusion of the achievements and findings during the course of this study. The chapter finishes with an outlook and suggestion on future directions.

1.10.5 Chapter 6 – Other contributions

Other contributions, results and findings of a project in collaboration with Tyler Shendruk, a former PhD candidate at the the time in Professor Slater's group, are briefly highlighted in the last chapter of this thesis.

1.11 References

[1] K. Pearson, *The Grammar of Science*, Walter Scott, **1892**.

[2] R. Glaser, *Biophysics: An Introduction*, Springer Science & Business Media, **2012**.

[3] F. Crick, *Nature* **1970**, *227*, 561.

[4] E. J. Topol, *Cell* **2014**, *157*, 241.

[5] M. A. Hamburg, F. S. Collins, *N. Engl. J. Med.* **2010**, *363*, 301.

[6] "Discovery of DNA Double Helix: Watson and Crick | Learn Science at Scitable," can be found under http://www.nature.com/scitable/topicpage/discovery-of-dna-structure-and-function-watson-397, **n.d.**

[7] R. H. Colby, M. Rubinstein, *Polymer Phyics*, New-York: Oxford University, **2003**.

[8] G. B. Salieb-Beugelaar, K. D. Dorfman, A. van den Berg, J. C. T. Eijkel, *Lab. Chip* **2009**, *9*, 2508.

[9] B. Rotman, *Proc. Natl. Acad. Sci. U. S. A.* **1961**, *47*, 1981.

[10] H. V. Thorne, *Virology* **1966**, *29*, 234.

[11] J. Hajdu, *Curr. Opin. Struct. Biol.* **2000**, *10*, 569.

[12] V. S. Perunicic, L. T. Hall, D. A. Simpson, C. D. Hill, L. C. L. Hollenberg, *Phys. Rev. B* **2014**, *89*, 054432.

[13] L. J. Kricka, *Ann. Clin. Biochem.* **2002**, *39*, 114.

[14] K. C. Neuman, A. Nagy, *Nat. Methods* **2008**, *5*, 491.

[15] P. K. Hansma, V. B. Elings, O. Marti, C. E. Bracker, *Science* **1988**, *242*, 209.

[16] S. Howorka, Z. Siwy, *Chem. Soc. Rev.* **2009**, *38*, 2360.

[17] Y. Feng, Y. Zhang, C. Ying, D. Wang, C. Du, *Genomics Proteomics Bioinformatics* **2015**, *13*, 4.

[18] A. Magi, B. Giusti, L. Tattini, *Brief. Bioinform.* **2016**, bbw077.

[19] A. S. Mikheyev, M. M. Y. Tin, *Mol. Ecol. Resour.* **2014**, *14*, 1097.

[20] "SmidgION," can be found under https://nanoporetech.com/products/smidgion, **n.d.**

[21] M. D. Graham, *J. Assoc. Lab. Autom.* **2003**, *8*, 72.

[22] S. B. Hladky, D. A. Haydon, *Nature* **1970**, *225*, 451.

[23] E. Neher, B. Sakmann, *Nature* **1976**, *260*, 799.

[24] J. J. Kasianowicz, E. Brandin, D. Branton, D. W. Deamer, *Proc. Natl. Acad. Sci.* **1996**, *93*, 13770.

[25] J. Li, D. Stein, C. McMullan, D. Branton, M. J. Aziz, J. A. Golovchenko, *Nature* **2001**, *412*, 166.

[26] B. N. Miles, A. P. Ivanov, K. A. Wilson, F. Doğan, D. Japrung, J. B. Edel, *Chem. Soc. Rev.* **2013**, *42*, 15.

[27] L. Song, M. R. Hobaugh, C. Shustak, S. Cheley, H. Bayley, J. E. Gouaux, *Science* **1996**, *274*, 1859.

[28] T. Z. Butler, M. Pavlenok, I. M. Derrington, M. Niederweis, J. H. Gundlach, *Proc. Natl. Acad. Sci.* **2008**, *105*, 20647.

[29] D. Wendell, P. Jing, J. Geng, V. Subramaniam, T. J. Lee, C. Montemagno, P. Guo, *Nat. Nanotechnol.* **2009**, *4*, 765.

[30] A. J. Storm, J. H. Chen, X. S. Ling, H. W. Zandbergen, C. Dekker, *Nat. Mater.* **2003**, *2*, 537.

[31] Z. Siwy, A. Fuliński, *Phys. Rev. Lett.* **2002**, *89*, 198103.

[32] W. Li, N. A. W. Bell, S. Hernández-Ainsa, V. V. Thacker, A. M. Thackray, R. Bujdoso, U. F. Keyser, *ACS Nano* **2013**, *7*, 4129.

[33] J. A. Bafna, G. V. Soni, *PLOS ONE* **2016**, *11*, e0157399.

[34] M. D. Fischbein, M. Drndić, *Appl. Phys. Lett.* **2008**, *93*, 113107.

[35] H. Liu, J. He, J. Tang, H. Liu, P. Pang, D. Cao, P. Krstic, S. Joseph, S. Lindsay, C. Nuckolls, *Science* **2010**, *327*, 64.

[36] L. Liu, C. Yang, K. Zhao, J. Li, H.-C. Wu, *Nat. Commun.* **2013**, *4*, DOI 10.1038/ncomms3989.

[37] S. Liu, B. Lu, Q. Zhao, J. Li, T. Gao, Y. Chen, Y. Zhang, Z. Liu, Z. Fan, F. Yang, L. You, D. Yu, *Adv. Mater.* **2013**, *25*, 4549.

[38] J. Larkin, R. Henley, D. C. Bell, T. Cohen-Karni, J. K. Rosenstein, M. Wanunu, *ACS Nano* **2013**, *7*, 10121.

[39] T. Albrecht, T. Gibb, P. Nuttall, in *Eng. Nanopores Bioanal. Appl.*, William Andrew Publishing, Oxford, **2013**, pp. 1–30.

[40] B. M. Venkatesan, R. Bashir, *Nat. Nanotechnol.* **2011**, *6*, 615.

[41] M. Wanunu, *Phys. Life Rev.* **2012**, *9*, 125.

[42] D. Fologea, E. Brandin, J. Uplinger, D. Branton, J. Li, *ELECTROPHORESIS* **2007**, *28*, 3186.

[43] J. Shim, G. I. Humphreys, B. M. Venkatesan, J. M. Munz, X. Zou, C. Sathe, K. Schulten, F. Kosari, A. M. Nardulli, G. Vasmatzis, R. Bashir, *Sci. Rep.* **2013**, *3*, 1389.

[44] N. de Souza, *Nat. Methods* **2014**, *11*, 8.

[45] F. Haque, J. Li, H.-C. Wu, X.-J. Liang, P. Guo, *Nano Today* **2013**, *8*, 56.

[46] M. L. Kovarik, S. C. Jacobson, *Anal. Chem.* **2008**, *80*, 657.

[47] K. Zhou, M. L. Kovarik, S. C. Jacobson, *J. Am. Chem. Soc.* **2008**, *130*, 8614.

[48] Z. Fekete, G. Huszka, A. Pongrácz, G. Jágerszki, R. E. Gyurcsányi, E. Vrouwe, P. Fürjes, *Procedia Eng.* **2012**, *47*, 13.

[49] J. K. Rosenstein, M. Wanunu, C. A. Merchant, M. Drndic, K. L. Shepard, *Nat. Methods* **2012**, *9*, 487.

[50] E. M. Nelson, V. Kurz, J. Shim, W. Timp, G. Timp, *Analyst* **2012**, *137*, 3020.

[51] T. Jain, R. J. S. Guerrero, C. A. Aguilar, R. Karnik, *Anal. Chem.* **2013**, *85*, 3871.

[52] Y. Goto, I. Yanagi, K. Matsui, T. Yokoi, K. Takeda, *Sci. Rep.* **2016**, *6*, DOI 10.1038/srep31324.

[53] T. Deng, Y. Wang, Q. Chen, H. Chen, Z. Liu, *Appl. Surf. Sci.* **n.d.**, DOI 10.1016/j.apsusc.2016.07.171.

[54] M. J. Kim, B. McNally, K. Murata, A. Meller, *Nanotechnology* **2007**, *18*, 205302.

[55] A. J. Storm, J. H. Chen, H. W. Zandbergen, C. Dekker, *Phys. Rev. E* **2005**, *71*, 051903.

[56] J. G. E. Gardeniers, H. a. C. Tilmans, C. C. G. Visser, *J. Vac. Sci. Technol. A* **1996**, *14*, 2879.

[57] U. F. Keyser, B. N. Koeleman, S. van Dorp, D. Krapf, R. M. M. Smeets, S. G. Lemay, N. H. Dekker, C. Dekker, *Nat. Phys.* **2006**, *2*, 473.

[58] V. Tabard-Cossa, M. Wiggin, D. Trivedi, N. N. Jetha, J. R. Dwyer, A. Marziali, *ACS Nano* **2009**, *3*, 3009.

[59] G. Baaken, N. Ankri, A.-K. Schuler, J. Rühe, J. C. Behrends, *ACS Nano* **2011**, *5*, 8080.

[60] V. Arnaut, M. Langecker, F. C. Simmel, *Biophys. J.* **2013**, *105*, 1199.

[61] S. W. Kowalczyk, A. R. Hall, C. Dekker, *Nano Lett.* **2010**, *10*, 324.

[62] F. Montagne, N. Blondiaux, A. Bojko, R. Pugin, *Nanoscale* **2012**, *4*, 5880.

[63] H. Wu, Y. Chen, Q. Zhou, R. Wang, B. Xia, D. Ma, K. Luo, Q. Liu, *Anal. Chem.* **2016**, *88*, 2502.

[64] C. Shasha, R. Y. Henley, D. H. Stoloff, K. D. Rynearson, T. Hermann, M. Wanunu, *ACS Nano* **2014**, *8*, 6425.

[65] C. J. Lo, T. Aref, A. Bezryadin, *Nanotechnology* **2006**, *17*, 3264.

[66] J. Li, J. A. Golovchenko, *Methods Mol. Biol. Clifton NJ* **2009**, *544*, 81.

[67] P. Chen, T. Mitsui, D. B. Farmer, J. Golovchenko, R. G. Gordon, D. Branton, *Nano Lett.* **2004**, *4*, 1333.

[68] H. Kwok, K. Briggs, V. Tabard-Cossa, *PLoS ONE* **2013**, *9*, DOI 10.1371/journal.pone.0092880.

[69] E. Beamish, H. Kwok, V. Tabard-Cossa, M. Godin, *Nanotechnology* **2012**, *23*, 405301.

[70] K. Briggs, H. Kwok, V. Tabard-Cossa, *Small* **2014**, *10*, 2077.

[71] E. Beamish, H. Kwok, V. Tabard-Cossa, M. Godin, *J. Vis. Exp.* **2013**, DOI 10.3791/51081.

[72] R. Tahvildari, E. Beamish, V. Tabard-Cossa, M. Godin, *Lab. Chip* **2015**, *15*, 1407.

[73] R. Tahvildari, E. Beamish, K. Briggs, S. Chagnon-Lessard, A. N. Sohi, S. Han, B. Watts, V. Tabard-Cossa, M. Godin, *Small* **2016**, DOI 10.1002/smll.201602601.

[74] V. Tabard-Cossa, in *Eng. Nanopores Bioanal. Appl.* (Eds: J.B. Edel, T. Albrecht), William Andrew Publishing, Oxford, **2013**, pp. 59–93.

[75] M. P. Norton, D. G. Karczub, *Fundamentals of Noise and Vibration Analysis for Engineers*, Cambridge University Press, **2003**.

[76] S. H. Tan, N.-T. Nguyen, Y. C. Chua, T. G. Kang, *Biomicrofluidics* **2010**, *4*, 032204.

[77] V. Tabard-Cossa, D. Trivedi, M. Wiggin, N. N. Jetha, A. Marziali, *Nanotechnology* **2007**, *18*, 305505.

[78] J. D. Uram, K. Ke, M. Mayer, *ACS Nano* **2008**, *2*, 857.

[79] M.-C. Lim, M.-H. Lee, K.-B. Kim, T.-J. Jeon, Y.-R. Kim, *J. Nanosci. Nanotechnol.* **2015**, *15*, 5971.

[80] M. Wanunu, W. Morrison, Y. Rabin, A. Y. Grosberg, A. Meller, *Nat. Nanotechnol.* **2010**, *5*, 160.

[81] O. Otto, U. F. Keyser, in *Eng. Nanopores Bioanal. Appl.* (Eds: J.B. Edel, T. Albrecht), William Andrew Publishing, Oxford, **2013**, pp. 31–58.

[82] A. Y. Grosberg, Y. Rabin, *J. Chem. Phys.* **2010**, *133*, 165102.

[83] P. Chen, J. Gu, E. Brandin, Y.-R. Kim, Q. Wang, D. Branton, *Nano Lett.* **2004**, *4*, 2293.

[84] K. J. Freedman, L. M. Otto, A. P. Ivanov, A. Barik, S.-H. Oh, J. B. Edel, *Nat. Commun.* **2016**, *7*, 10217.

[85] Y. Xia, G. M. Whitesides, *Angew. Chem. Int. Ed.* **1998**, *37*, 550.

[86] T. Thorsen, S. J. Maerkl, S. R. Quake, *Science* **2002**, *298*, 580.

[87] J. A. Riordon, Developing Microfluidic Volume Sensors for Cell Sorting and Cell Growth Monitoring, 2014, **2014**.

[88] D. R. Gossett, W. M. Weaver, A. J. Mach, S. C. Hur, H. T. K. Tse, W. Lee, H. Amini, D. Di Carlo, *Anal. Bioanal. Chem.* **2010**, *397*, 3249.

[89] A. G. Hadd, D. E. Raymond, J. W. Halliwell, S. C. Jacobson, J. M. Ramsey, *Anal. Chem.* **1997**, *69*, 3407.

[90] L. J. Kricka, P. Wilding, *Anal. Bioanal. Chem.* **2003**, *377*, 820.

[91] N. Chiem, D. J. Harrison, *Anal. Chem.* **1997**, *69*, 373.

[92] B. G. Chung, L. A. Flanagan, S. W. Rhee, P. H. Schwartz, A. P. Lee, E. S. Monuki, N. L. Jeon, *Lab. Chip* **2005**, *5*, 401.

[93] G. M. Whitesides, *Nature* **2006**, *442*, 368.

[94] T. M. Squires, S. R. Quake, *Rev. Mod. Phys.* **2005**, *77*, 977.

[95] L. R. Brewer, P. R. Bianco, *Nat. Methods* **2008**, *5*, 517.

[96] V. Studer, G. Hang, A. Pandolfi, M. Ortiz, W. F. Anderson, S. R. Quake, *J. Appl. Phys.* **2004**, *95*, 393.

[97] K. W. Oh, C. H. Ahn, *J. Micromechanics Microengineering* **2006**, *16*, R13.

[98] M. A. Unger, H.-P. Chou, T. Thorsen, A. Scherer, S. R. Quake, *Science* **2000**, *288*, 113.

[99] J. Melin, S. R. Quake, *Annu. Rev. Biophys. Biomol. Struct.* **2007**, *36*, 213.

[100] J. Liu, C. Hansen, S. R. Quake, *Anal. Chem.* **2003**, *75*, 4718.

[101] J. Riordon, M. Nash, W. Jing, M. Godin, *Biomicrofluidics* **2014**, *8*, 011101.

[102] N. A. W. Bell, V. V. Thacker, S. Hernández-Ainsa, M. E. Fuentes-Perez, F. Moreno-Herrero, T. Liedl, U. F. Keyser, *Lab. Chip* **2013**, *13*, 1859.

[103] T. R. Gibb, A. P. Ivanov, J. B. Edel, T. Albrecht, *Anal. Chem.* **2014**.

Chapter 2 | Experimental setup and methods

This chapter starts with a brief introduction of the microfabrication and soft lithography used for building the microfluidic devices. Further information is also provided about the experimental setup, including the Faraday cage and fluid setup, nanopore fabrication using controlled breakdown (CBD), and characterization methods for the fabricated nanopore. Furthermore, the inclusion of microfluidic via (microvia), as an approach to reduce the high-frequency noise in the integrated microfluidic-nanopore device, is discussed.

2.1 Microfabrication

2.1.1 Introduction

Microfabrication, the ability to build small structures, has become an important part of modern science and technology. Many opportunities in research and development are provided by downsizing the structures. For example, transistors in microelectronics are smaller devices with more components in one chip, higher performance, lower energy consumption and notably less expensive. Microfabrication not only has its basis in microelectronics but also increasingly is being used in miniaturization and integration of other devices with vast applications. This allows the study of basic scientific phenomena at small dimensions.[1]

Microfabrication should be done in an extremely clean and dust-free environment, known as the cleanroom. The environment has regulated temperature and humidity while a flux of air is continuously traversed. The number of particles of size less than 4 µm per cubic inch defines the class of the clean room, which varies from 1000 to 10000.

The most successful patterning technique in microfabrication is photolithography. The procedure consists of coating a substrate with a photosensitive resist, and then exposing it to a UV light source through a mask with the desired patterns. The exposed zones become either soluble or not in a particular solvent, respectively corresponding to a positive or a negative resist. SU8-series (MicroChem, *Westborough, MA, USA*) and AZ-series (Integrated Micro Materials, *Argyle, TX, USA*) are the most commonly used resists. SU8 are negative photoresists used to fabricate square-shaped features with high-resolution. Whereas AZ are positive photoresists and reflowed by an additional heating step to form channels with semi-circular cross section (rounded).[2] In particular, these rounded channels are very useful to obtain perfect seal when they are fully compressed by pressurized control channels (valves).[3]

Figure 2-1 shows the processing steps to fabricate features with either of the photoresists. The AZ film should be exposed to UV at least an hour after a rehydration step. For this purpose, the substrate coated with AZ film is placed in a covered dish while surrounded by a few damped lint free clothes.

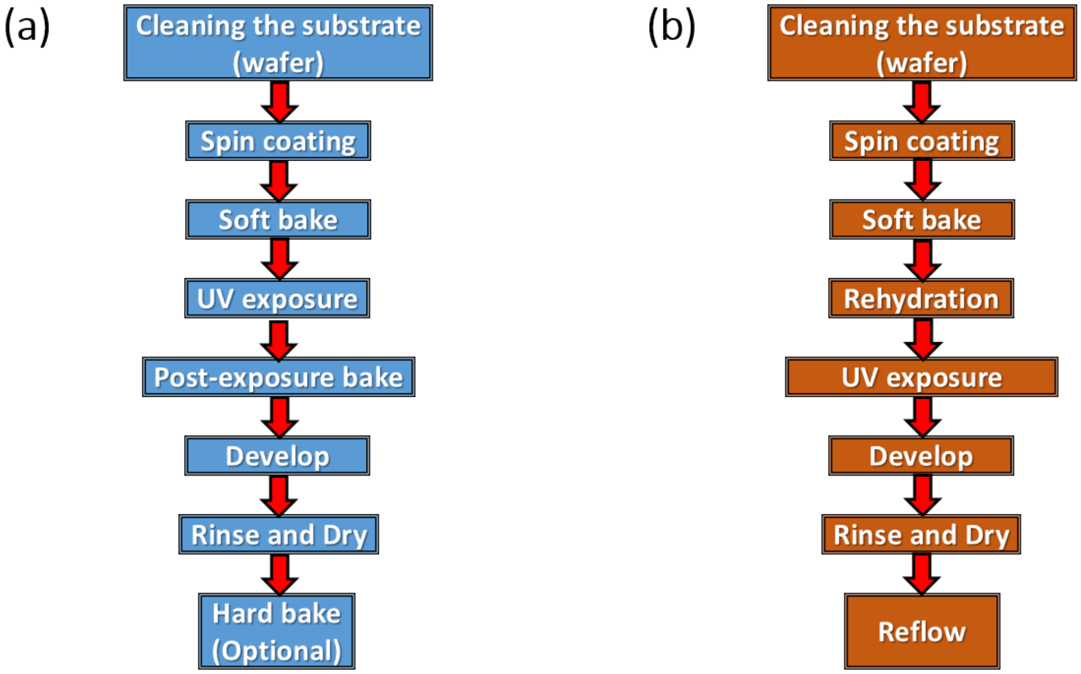

Figure 2-1 Processing steps to fabricate features with **(a)** SU8-series and **(b)** AZ-series photoresists. Fabrication parameters are set based on the desired height of the microchannel.

The substrate to coat the photoresist is normally a silicon wafer. The photoresist film is then soft baked to evaporate the solvent and densify the film. The wafer is then placed in direct contact with the photomask (a transparency with printed features) to selectively expose the film to UV light in order to obtain optimal cross-linking. There are two types of photomask, positive and negative. A post-exposure bake is required to promote cross-linking of the exposed regions. Afterwards, the wafer is immersed in the appropriate developer to remove all uncross-linked photoresist.

The fabrication parameters, including spin speed, baking temperature and duration, and the time length for UV exposure and developing procedure are adjusted based on the photoresist type and the desired feature thickness, which in this work dictate the height of the microfluidic channels. These fabrication settings for each of the presented devices are provided in detail in the related sections of Chapters 3 and 4.

Over the course of this work SU8-10, SU8-2050 and AZ-50XT photoresists were used to fabricate various microfluidic channels. Figure 2-2 is a comparison between the patterns and shapes of two typical microchannels made of these photoresists.

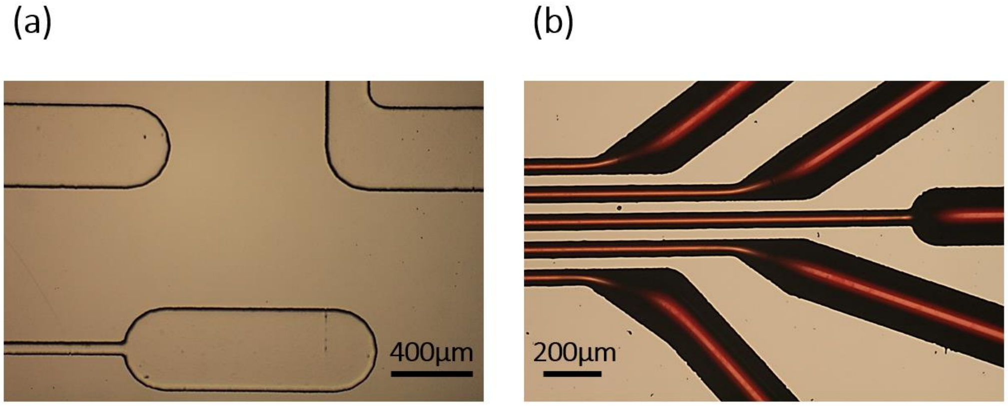

Figure 2-2 Typical fabricated microchannels with rectangular and arched shapes, respectively made of **(a)** SU8-2050 photoresist and **(b)** reflowed AZ-50XT photoresist.

2.1.2 Designs

First, the network of microfluidic channels is designed in a CAD program (in this work, CleWin4©). The design is printed on a flexible transparency (photomask) with either a negative or positive polarity using a high-resolution printer. During this work, several different photomasks were designed and used for fabrication of various master moulds. Although not all of the designed photomasks led to successful devices, a comprehensive list of the masks are presented in Section 7.1 of Chapter 7-Appendix.

2.1.3 Soft lithography

Soft lithography is a technique based on replica moulding for fabrication of the microfluidic devices.[4] The mould substrate is typically a silicon wafer and the features are first fabricated using photolithography process as discussed earlier and illustrated in Figure 2-1. A stylus profiler (in this work, Dektak 3-30, Veeco Sloan) is used to measure the related feature thicknesses. Finally, the wafer is treated with Chlorosilane to decrease its surface energy and preserve the features.

In the field of fabrication of microfluidics, Polydimethylsiloxane (PDMS) is the most common used material. PDMS belongs to a family of polymers with $(\text{-Si}(CH_3)_2O)\text{-}$ formula and contain silicon oils. Some remarkable properties of PDMS are elasticity, biocompatibility, transparency to visible and short-wave UV light, permeability to O_2 and CO_2, controllable surface chemistry, the ability to bond irreversibly to different materials (including itself, silicon and glass), to form closed microchannels, and their weak surface energy, which facilitates to peel them off from the master mould.

The PDMS kit consists of two components, the base and the curing agent (in this work, Sylgard 184 elastomer kit). A mix of the base and the curing agent is normally degassed, poured on the mould, and heated at a moderately elevated temperature (70^0 - 80^0C) for at least an hour. The mixing ratio of these two components varies based on the desired stiffness or softness of PDMS, 5:1 (base to curing agent) is the stiffest and 20:1 (base to curing agent) is the softest. The solidified PDMS can easily be peeled off and contains the mould structures in a negative way. This method can obtain features with sub-micrometric precision.[5] Although it is possible to make features with high aspect ratio, due to the deformability of PDMS, aspect ratio are normally limited to no lower than 1 to 10 for the microfluidic structures.

The PDMS pieces are oxidized using an oxygen or air plasma system. The oxidization process replaces methyl groups ($Si\text{-}CH_3$) by silanol groups (Si-OH) at the surface of the PDMS layer, results in formation of covalent siloxane bonds (Si-O-Si) when the plasma treated surfaces are brought together.[6] This allows to build active microfluidic devices containing multiple patterned layers of PDMS, each of which is separately replicated from a mould (Multi-layer soft lithography).[3]

The plasma treatment also makes the PDMS surfaces more hydrophilic therefore they easily get wet by aqueous solutions.[7] However, the PDMS surface recovers its native hydrophobicity with time due to the migration of low molecular weight oligomers from the bulk of the PDMS to the surface.[8]

2.1.4 Device assembly

In this work, three different devices are presented, shown in Figure 2-3. In Chapters 3 and 4, the devices are related to the integration of nanopore sensors within two different PDMS-microfluidic architectures,

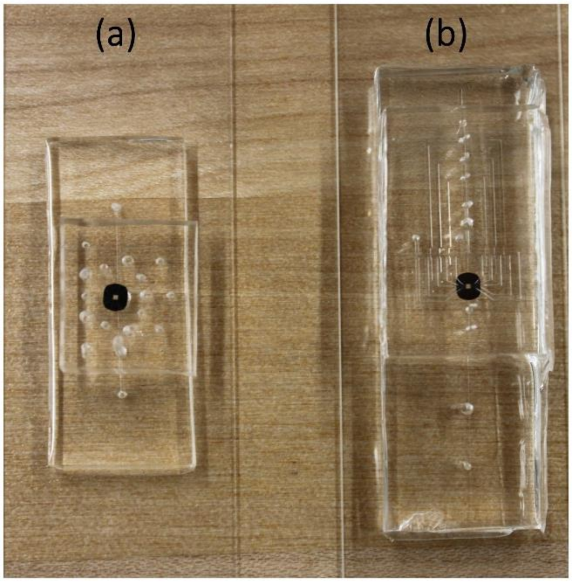

Figure 2-3 The two assembled devices used during the course of this study and respectively presented in Chapters 3 and 4 **(a)** Solid-state nanopore arrays fabricated in situ by controlled dielectric breakdown (CBD) integrated within microfluidic devices.[9] **(b)** Manipulation of electrical and fluidic access in the integrated nanopore microfluidic arrays using PDMS-based pneumatic microvalves[10].

2.1.4.1 Integrated nanopore-microfluidic devices

Multilayer soft lithography was used to fabricate the two integrated nanopore-microfluidic devices presented in Chapters 3 and 4. Commercially available, low-stress 500×500 µm^2, 20-nm-thick silicon nitride membrane (SiMPore Inc. SN100-A20Q05, *West Henrietta*, *NY*, *USA*) was embedded between layers of PDMS. The membrane is supported on a 100-µm-thick, 4mm×3mm frame size silicon substrate. The dimensions of the chip are depicted in Figure 2-4. Microfabrication, required materials, protocols, and assembly steps for each device are explained in detail in Sections 3.7 and 4.7, and illustrated in Figures 3-2 and 4-2.

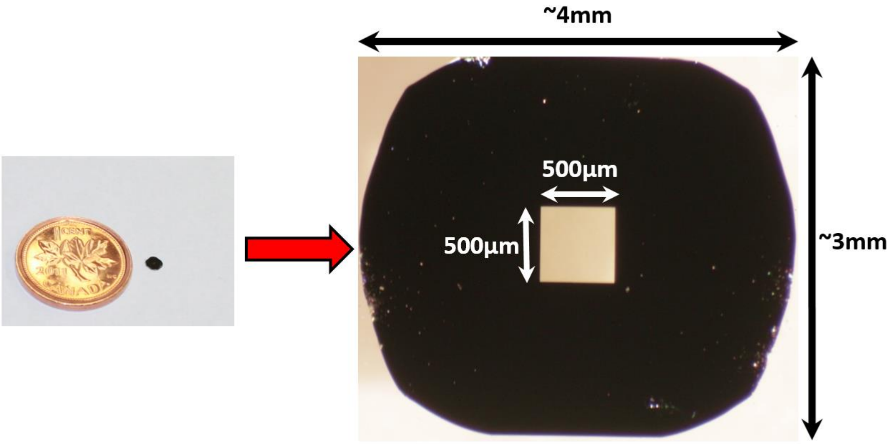

Figure 2-4 Optical image of a TEM membrane window (SiMPore Inc. SN100-A20Q05)

2.2 Fluid flow setup

Pressure-driven flow is used to introduce aqueous solutions to the microfluidic channels. Solution-containing vials were connected to the devices via polyethylene tubing. The components of the fluid flow setup, used over the course in this work, are shown in Figure 2-5. Typically, flow was established using pressure regulators (Marsh Bellofram Type 10) connected to compressed air. These regulators applied pressure to the vials on demand through solenoid valves (SMC S070C-SDG-32) which were acting as on/off switches and controlled by a custom-designed LabView software (National Instruments). Flow control diagram for each presented device is illustrated individually at the end of Chapters 3, 4 and 5.

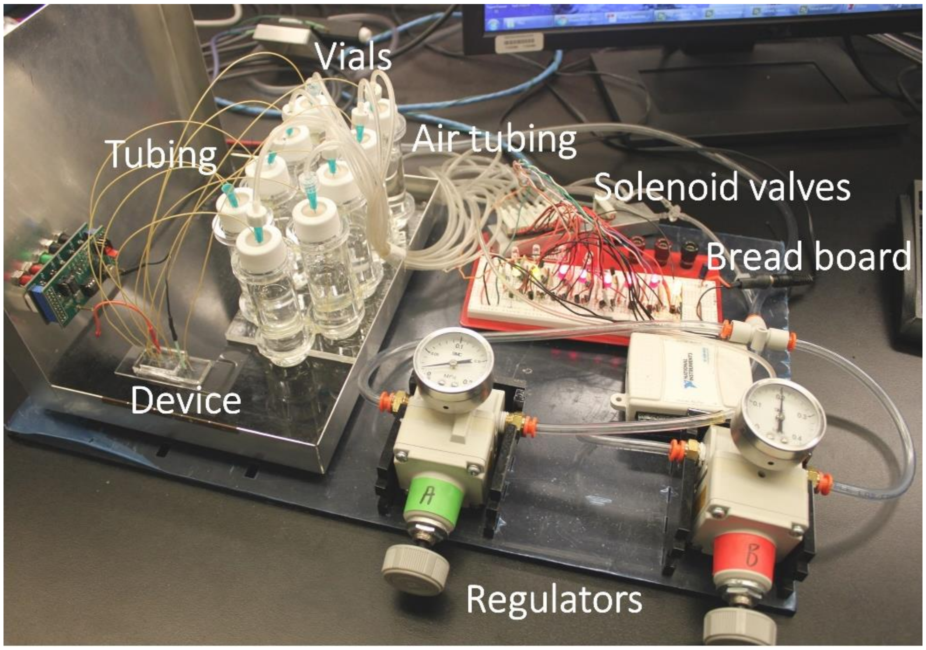

Figure 2-5 Different parts of the fluid flow setup

2.3 Experimental setup & Methods – Integrated nanopore-microfluidic device

2.3.1 Nanopore housing – Faraday cage

The main components of the experimental setup used over the course of this work to fabricate the nanopore by controlled breakdown (CBD) and perform a sensing experiment are respectively shown in Figure 2-6 and Figure 2-7.

To shield the acquisition electronics from external electrical noise, all experiments, including nanopore fabrication and sensing, were performed inside a Faraday cage. In this work, the Faraday cage (pointed out in Figure 2-6 and Figure 2-8) is made of a ~1.5-mm thick aluminium sheet, which is folded to accomplish the desired shape (26×21×20 cm). It accommodates the device, electrodes, tubing, the vials, the nanopore fabrication circuit and the headstage (during sensing experiment). During nanopore fabrication and current measurements, the Faraday cage was grounded via the common ground in the DC power supply and the Axopatch respectively. The vibrations from external sources, such as the laboratory bench, requires to be isolated as well. To minimize the effect of such noises, in this work, the inside walls of the Faraday cage were covered by a commercially available vibration damper (Sorbothane). The layout of the cage with detailed dimensions is provided in Section 7.2 of the Chapter 7-Appendix.

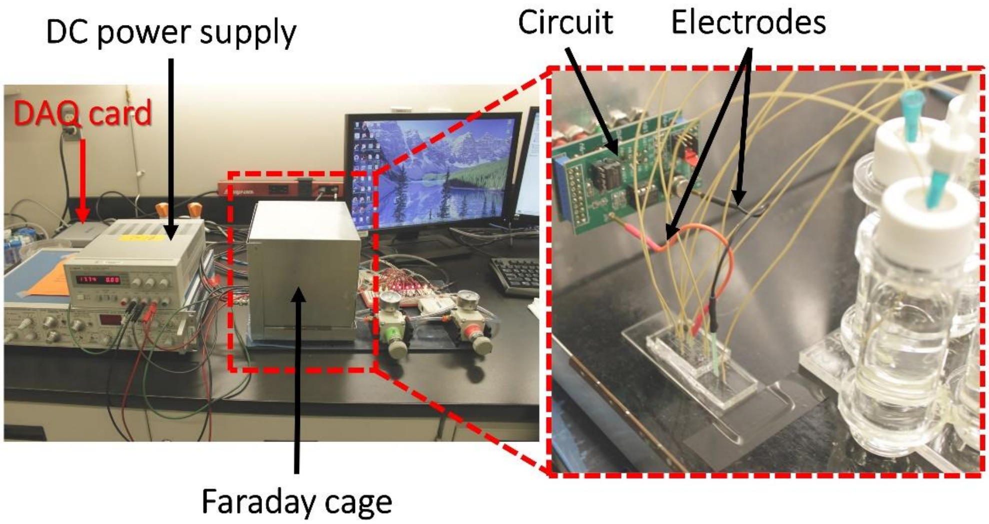

Figure 2-6 Configuration of the experimental setup during the nanopore fabrication

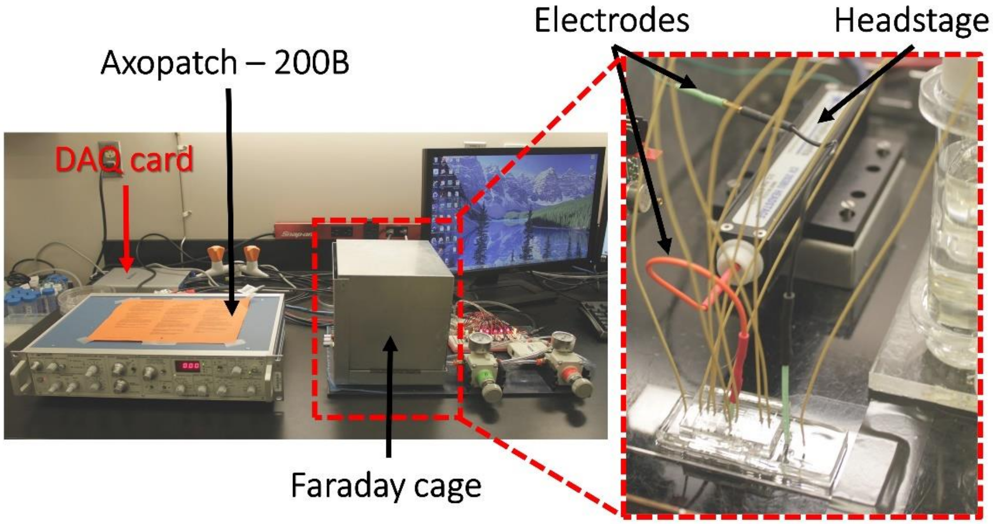

Figure 2-7 Configuration of the experimental setup during the single-molecule sensing. In the image the amplifier (Axopatch 200B) and headstage (current-to-voltage (I-V) converter) are shown.

2.3.2 Nanopore fabrication

Individual nanopores were fabricated within a few minutes by Controlled Breakdown (CBD)[11] directly in the electrolyte. In this work, nanopores were typically fabricated in 1 M KCl. High electric fields across the SiN membrane (using a potential difference of 14 V to 18 V) were applied through each of the integrated fluidic channels using a custom-built current amplifier circuit[11], shown in Figure 2-8.

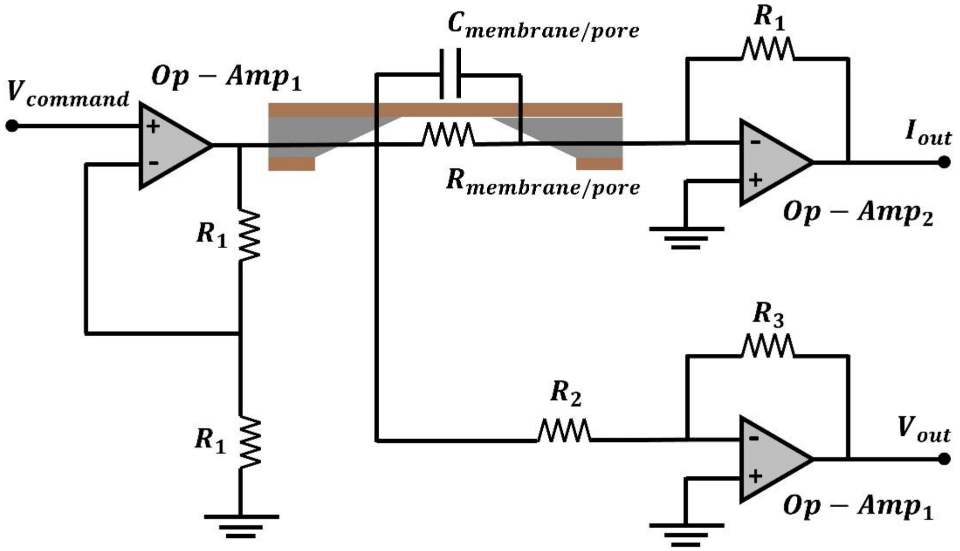

Figure 2-8 Schematic of the custom-built current amplifier used for the nanopore fabrication. DC power supply used to power the Op-amps. The DAQ card provides a command voltage between ± 10 V and amplified in the range of ± 20 V using the op-amps. The output voltage and current are simultaneously monitored. The biased voltage is cut off when the current passes pre-defined threshold. In this circuit, Op-Amp$_1$ is AD820, Op-Amp$_2$ is AD549, and the resistors are R_1=5 MΩ, R_2=1 MΩ, R_3=10 kΩ. The schematic is adapted from Reference.[11]

In Chapters 3 and 4, typical nanopore fabrication curves by CBD are shown. Nanopores were conditioned and enlarged as required by the cyclic application of moderate electric field pulses.[9,12]

2.3.3 Current versus Voltage (I-V) characteristic and size estimation

The nanopore system can simply be represented by an electrical circuit, Figure 2-8. This equivalent circuit helps to analyze electrical noise and understand the related calculations to estimate the size of a nanopore.

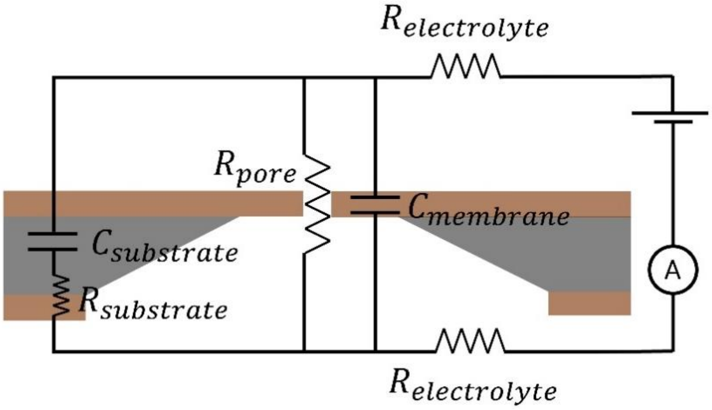

Figure 2-9 A nanopore device can be shown with a simple electrical circuit in which $R_{electrolyte}$ is the resistance from the electrode interface to the membrane, R_{pore} is the nanopore resistance, and $R_{substrate}$ is the electric path through the silicon and dielectric layers. In this schematic, capacitance of the membrane and capacitance through the substrate are respectively labelled as $C_{membrane}$ and $C_{substrate}$. The schematic is adapted from Reference[13].

For an integrated nanopore within microfluidics, the electrical access resistance, $R_{electrolyte}$, from the electrode/electrolyte interface to the membrane generally depends on the geometry of the microfluidic channels. However, in all of the presented designs the location of the electrodes was particularly chosen to limit the electrical resistance of the channels approaching each nanopore (typically ~1% of the total electrical resistance of a 10-nm nanopore). This causes $R_{electrolyte}$ to become negligible in comparison to R_{pore}, representing the nanopore resistance, and the voltage drops for the most part across the nanopore length. Therefore, an I-V curve obtained by a voltage sweep measures R_{pore}, which is directly proportional to the size of the nanopore. However, R_{pore} is assumed to include three effects[14],

1) Resistance due to geometry (length and diameter of the nanopore for a cylindrical model)
2) Nanopore access resistance (edge effects)
3) Resistance due to the wall surface charge (surface effects)

Nanopores formed in thin membranes by CBD are generally assumed to be cylindrical in shape. Based on this assumption, and using the basic equation for resistance between two electrodes in solution, the resistance for such a nanopore based on its geometry $R_{geometry}$ can be obtained by,

$$R_{pore} = \frac{4L_{pore}}{\sigma\pi d_{pore}^2} \tag{2.1}$$

In which σ is the conductivity of the electrolyte solution, d_{pore} is the diameter of a circular nanopore and L_{pore} is the thickness of the membrane.

Normally for a long and narrow nanopore the edge effects are negligible and ignored. However, for a short nanopore, thinner membrane $L_{pore} \ll d_{pore}$, this effects should be considered and the total resistance can be dominated by the so-called "access resistance". For this type of nanopore, the access resistance describes the contribution of the electric field lines, converging from the bulk electrolyte to the mouth of the pore. While the calculation is beyond the scope of this thesis, the result is generated based on the following equation[14–16],

$$R_{access} = \frac{1}{2\sigma d_{pore}} \tag{2.2}$$

An access region is present on both sides of the nanopore, each contributing equally to the resistance. Therefore, the coefficient of 2, in Equation 2.2., should be dropped for the overall access resistance of the nanopore.

Finally, the surface charge of the walls inside the nanopore also contributes to the change in the resistance. For the nanopores milled in silicon nitride membranes and immersed in an electrolyte, the surface charge density $\sigma_{surface}$ is typically negative. This negative charge is screened by cations (K^+ or Li^+, depending on the electrolyte), which forms an electrostatic double layer λ_D. For very small nanopores, $d \sim \lambda_D$, this double layer results in a greater number of ions within the nanopore and decreases the resistance of the entire system. This is the only term that does not depend on the conductivity of the solution and written as[17],

$$R_{surface} = \frac{L_{pore}}{\mu_* \pi d_{pore} \sigma_{surface}} \tag{2.3}$$

In Equation 2.2, μ_* is the electrophoretic mobility of the counterions and $\sigma_{surface}$ is the surface charge density of the walls of the nanopore.

Thus the total resistance of a nanopore is the sum of the three discussed terms,

$$R_{pore} = \left(\frac{4L_{pore}}{\sigma\pi d_{pore}^2} + \frac{1}{\sigma d_{pore}} + \frac{L_{pore}}{\mu_*\pi d_{pore}\sigma_{surface}}\right) \tag{2.4}$$

And the conductance of the pore will be given by,

$$G_{pore} = \frac{1}{R_{pore}} = \sigma\left(\frac{4L_{pore}}{\pi d_{pore}^2} + \frac{1}{d_{pore}} + \frac{\sigma L_{pore}}{\mu_*\pi d_{pore}\sigma_{surface}}\right)^{-1} \tag{2.5}$$

At sufficiently high salt concentration (≥ 1 M) the first two terms related to the geometry and the access resistance of the nanopore dominate.[17,18] At high salt concentration charge carriers in the solution contribute to the overall ionic current and negative surface charge is screened by mobile counterions.[17] Therefore, over the course of this work that the experiments performed either in 1 M KCl, 2 M KCl or 3.6 M LiCl, the conductance affects by surface charge was not considered and Equation 2.5 simplifies as;

$$G_{pore} = \sigma\left(\frac{4L_{pore}}{\pi d_{pore}^2} + \frac{1}{d_{pore}}\right)^{-1} \tag{2.6}$$

According to Equation 2.6, the conductance scales with d_{pore}^2 in longer nanopores (thicker membrane) while for very short nanopores (very thin membrane) the conductance scales linearly with d_{pore}. However, the access resistance term dominates for $L_{pore} \rightarrow 0$, and conductance stays linear with d_{pore}.[19]

Using Equation 2.6 and solving it for the nanopore diameter, the following equation will be obtained,

$$d_{pore} = \frac{G_{pore}}{2\sigma}\left(1 + \sqrt{1 + \frac{16\pi L_{pore}}{\pi G}}\right) \tag{2.7}$$

As discussed in Chapter 3 and 4, Sections 3.4 and 4.4, the slope of a current to voltage (IV) curve provides the conductance of a nanopore. The nanopore size can then be calculated by using the conductance value and inserting other parameters (solution conductance and thickness of the membrane) in Equation 2.6. Typical IV curves used to infer the size of several fabricated nanopores by CBD within microfluidic networks are presented in Figure 3-3 and 4-3.

2.3.4 DNA translocation

Once a molecule is electrophoretically driven through a nanopore, the measured current will be dropped to one or more distinct levels, knows as a blockade event. This drop in conductance according to Equation 2.6 can obtained by[16,20],

$$\Delta\mathrm{G} = \mathrm{G_{pore}} - \mathrm{G'_{pore}} \qquad (2.8)$$

Where $\mathrm{G'_{pore}}$is calculated based on $\mathrm{d'_{pore}}$, the effective diameter of the nanopore in the presence of a DNA molecule which is written as follows,

$$\mathrm{d'_{pore}} = \sqrt{\mathrm{d^2_{pore}} - \mathrm{d^2_{DNA}}} \qquad (2.9)$$

In this equation, $\mathrm{d_{DNA}}$ is the diameter of a DNA molecule. As discussed earlier in Section 1.4, it is ~1.2-1.5 nm for ssDNA and 2.2nm for dsDNA molecule.

2.3.5 Instrumentation for single-molecule sensing

An Axopatch 200B amplifier (Molecular Devices), shown in Figure 2-7, was used to acquire ultra-low noise current at high bandwidth. This instrument provides biases up to 1 V and measures current with picoampere sensitivity up to 200 nA. Its actively cooled headstage reduces thermal noise for improved signal-to-noise ratios. The electrical signals are amplified (low currents are converted to easily measurable voltages) by the headstage and connected through openings in the Faraday cage to the instrument chassis. Analogue signals from the amplifier are digitized with a National Instruments data acquisition (DAQ) card (USB-6351) connected to a computer. The DAQ card is also used to control the amplifier’s sourced voltage and record ionic current readings using custom-designed LabView software. The fastest time resolution is typically limited by the sampling rate, and also limited to the maximum bandwidth of the measurement. To maximize the temporal resolution, the ionic currents, presented in Chapter 3 and Chapter 4, were sampled at 250 kHz and low-pass filtered at 100 kHz using a 4-pole Bessel filter.

2.3.6 Noise characteristic

In the previous chapter, it was discussed that improving signal-to-noise ratio (SNR) is among the major topics of interest in solid-state nanopore sensors. The high frequency noise is the sum of the dielectric properties of the silicon chip and the noise of the measurement equipment. The capacitance of the membrane, illustrated in Figure 2-8, has the largest contribution. Therefore, several attempts and methods have been reported to mitigate this noise issue, including painting the chip with PDMS[21] (Figure 2-9(a)). Over the course of the work, a similar approach was used to reduce significantly the capacitance noise that arises from the silicon nitride membrane.[22]

A thin PDMS layer accommodates several microfluidic vias (microvias), shown in Figure 2-9(b) and (c), is placed between the SiN membrane and the microfluidic channels. These microvias minimize the exposed area of the membrane to the electrolyte, resulting in considerable reduction of the capacitance noise. For some geometries of the microvia, the RMS noise is reduced by a factor of 2 in comparison to the standard macroscopic cell (Figure 1-14). This inclusion also confines the electrical field to specific regions of the SiN membrane and controls the location of nanopore formation on the SiN membrane.[9] The effects of adding the microvias to the microfluidic configuration will be discussed further in Sections 3.8.4 and 3.8.6 of Chapter 3.

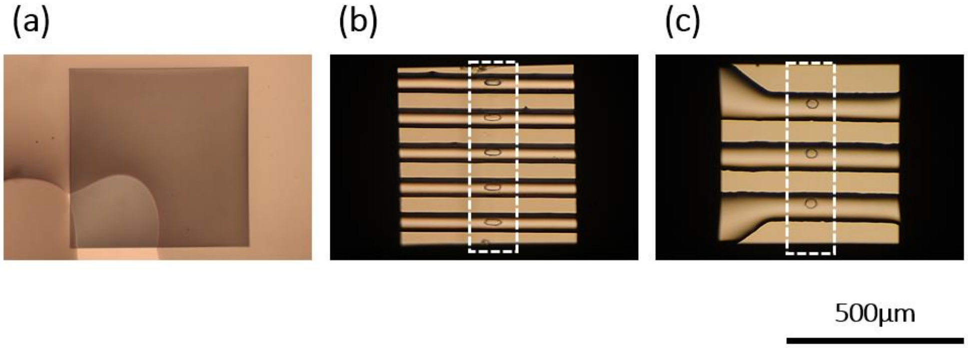

Figure 2-10 Comparison of three 500×500 µm^2 silicon nitride (SiN) membranes. **(a)** The surface of a SiN membrane is painted with PDMS, **(b)** five microfluidic channels, accommodates a 50×20 µm^2 microvia, and **(c)** three microfluidic channels, each contains a 30×30 µm^2 microvias. The white dashed boxes represent the location of the microvias.

2.4 References

[1] D. Qin, Y. Xia, J. A. Rogers, R. J. Jackman, X.-M. Zhao, G. M. Whitesides, in *Microsyst. Technol. Chem. Life Sci.* (Eds: P.A. Manz, D.H. Becker), Springer Berlin Heidelberg, **1998**, pp. 1–20.

[2] Z. Huang, X. Li, M. Martins-Green, Y. Liu, *Biomed. Microdevices* **2012**, *14*, 873.

[3] M. A. Unger, H.-P. Chou, T. Thorsen, A. Scherer, S. R. Quake, *Science* **2000**, *288*, 113.

[4] D. Qin, Y. Xia, G. M. Whitesides, *Nat. Protoc.* **2010**, *5*, 491.

[5] E. Kim, Y. Xia, G. M. Whitesides, *Nature* **1995**, *376*, 581.

[6] M. A. Eddings, M. A. Johnson, B. K. Gale, *J. Micromechanics Microengineering* **2008**, *18*, 67001.

[7] S. H. Tan, N.-T. Nguyen, Y. C. Chua, T. G. Kang, *Biomicrofluidics* **2010**, *4*, 32204.

[8] J. N. Lee, C. Park, G. M. Whitesides, *Anal. Chem.* **2003**, *75*, 6544.

[9] R. Tahvildari, E. Beamish, V. Tabard-Cossa, M. Godin, *Lab. Chip* **2015**, *15*, 1407.

[10] R. Tahvildari, E. Beamish, K. Briggs, S. Chagnon-Lessard, A. N. Sohi, S. Han, B. Watts, V. Tabard-Cossa, M. Godin, *Small* **2016**, DOI 10.1002/smll.201602601.

[11] H. Kwok, K. Briggs, V. Tabard-Cossa, *PLoS ONE* **2013**, *9*, DOI 10.1371/journal.pone.0092880.

[12] E. Beamish, H. Kwok, V. Tabard-Cossa, M. Godin, *Nanotechnology* **2012**, *23*, 405301.

[13] V. Tabard-Cossa, in *Eng. Nanopores Bioanal. Appl.* (Eds: J.B. Edel, T. Albrecht), William Andrew Publishing, Oxford, **2013**, pp. 59–93.

[14] T. Albrecht, T. Gibb, P. Nuttall, in *Eng. Nanopores Bioanal. Appl.*, William Andrew Publishing, Oxford, **2013**, pp. 1–30.

[15] J. E. Hall, *J. Gen. Physiol.* **1975**, *66*, 531.

[16] S. W. Kowalczyk, A. Y. Grosberg, Y. Rabin, C. Dekker, *Nanotechnology* **2011**, *22*, 315101.

[17] R. M. M. Smeets, U. F. Keyser, D. Krapf, M.-Y. Wu, N. H. Dekker, C. Dekker, *Nano Lett.* **2006**, *6*, 89.

[18] O. Otto, U. F. Keyser, in *Eng. Nanopores Bioanal. Appl.* (Eds: J.B. Edel, T. Albrecht), William Andrew Publishing, Oxford, **2013**, pp. 31–58.

[19] M. Wanunu, *Phys. Life Rev.* **2012**, *9*, 125.

[20] A. T. Carlsen, O. K. Zahid, J. Ruzicka, E. W. Taylor, A. R. Hall, *ACS Nano* **2014**, *8*, 4754.

[21] V. Tabard-Cossa, D. Trivedi, M. Wiggin, N. N. Jetha, A. Marziali, *Nanotechnology* **2007**, *18*, 305505.

[22] V. Tabard-Cossa, M. Godin, R. Tahvildari, E. Beamish, *Integrating Nanopore Sensors Within Microfluidic Channel Arrays Using Controlled Breakdown*, **2016**, WO/2016/098080.

Outlined contributions

Technical Innovation: Integrating nanopore sensors within microfluidic channel arrays using controlled breakdown

- This work was submitted on **November 19th, 2014** and published online on **January 19th, 2015** in *Lab on a Chip*.
- I, Radin Tahvildari, and Eric Beamish, PhD candidate in the Godin lab, contributed equally to this work.
- I, Radin Tahvildari, led the large majority of the work presented in this scientific article including: device design (photomasks), microfabrication, devices assembly, sample preparation, performing experiments, and data acquisition and data analysis.
- Eric Beamish performed the finite element modeling of the electric field in the presented devices using COMSOL Multiphysics Modeling Software© (The results are presented in Section 3.7.4). He also aided for the experimental setup, provided technical advices on performing initial experiments, and assisted in writing of the manuscript.
- The work was done under the supervision of Professor Michel Godin and Professor Vincent Tabard-Cossa.
- The format of the manuscript has been modified for formatting purposes.
- The presented supplementary material, Section 3.7, was published with this work.
- Section 3.8 is an additional note and originally was not included in the published manuscript.

Chapter 3 | Integrating nanopore sensors within microfluidic channel arrays using controlled breakdown

Reproduced by permission of The Royal Society of Chemistry (RSC) from:

Tahvildari, R., Beamish, E., Tabard-Cossa, V., and Godin, M. Integrating nanopore sensors within microfluidic channel arrays using controlled breakdown. *Lab on a Chip* **15**, 1407 (2015). DOI: 10.1039/C4LC01366B

3.1 Motivation and Objectives

Nanopores are used to detect and analysis single-molecule directly in solution. They have potential to lead revolutionary advances in the diagnosis and treatment of various diseases. However, as discussed earlier in Chapter 1, the conventional nanopore setup is made of a simple macro scale fluidic cells with several drawbacks. For instance, it is impracticable to fabricate and perform biomolecular sensing through array of several nanopores in the standard setup.

Microfluidics are ideal networks to control and confine precisely fluids. Many studies have demonstrated integration of nanopores within microfluidic devices while such a platform potentially reduces the high-frequency noise in the measured signals. In these studies, the nanopores were fabricated *ex situ* using energetic particles beam which adds further challenges for the integration process.

Controlled breakdown (CBD), a simple and inexpensive approach, facilitates the nanopore fabrication *in situ* within wide range of fluidic configurations. The main objective of this work was to design and develop a multi-channel microfluidic device to fabricate an array of low-noise nanopore sensors.

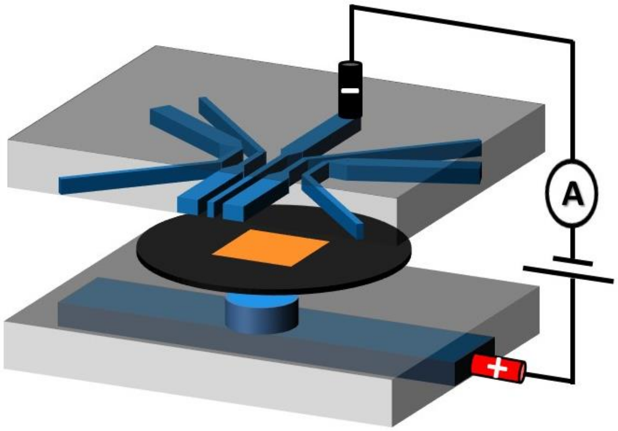

Figure 3-1 Scheme (not to scale) of an embedded silicon chip consists of a silicon nitride (SiN) membrane within microfluidic channel arrays. The presented device consists of five-independent microchannels aligned atop one side of the SiN membrane while one single channel (common) channel is located underneath of the chip.

3.2 Abstract

Nanopore arrays are fabricated by controlled dielectric breakdown (CBD) in solid-state membranes integrated within polydimethylsiloxane (PDMS) microfluidic devices. This technique enables the scalable production of independently addressable nanopores. By confining the electric field within the microfluidic architecture, nanopore fabrication is precisely localized and electrical noise is significantly reduced. Both DNA and protein molecules are detected to validate the performance of this sensing platform.

3.3 Introduction

Nanopores are now a well-established class of label-free sensors capable of detecting single molecules electrically.[1–4] The technique relies on the application of a voltage across a nano-scale aperture in a thin, insulating membrane immersed in an ionic solution. Modulation of the resulting ionic current can be associated with the translocation of individual charged biomolecules such as DNA and proteins that are electrophoretically driven through the nanopore.[5] These changes in conductance provide information about the length, size, charge and shape of translocating molecules.[2,6–9] A variety of single-molecule studies, including DNA sequencing[8,10,11], protein detection[12] and unfolding[13], single-molecule mass spectrometry[14] and force spectroscopy[15] make this technology particularly attractive.

Nanopores may be formed by incorporating proteinaceous pores in lipid bilayer membranes[16] or fabricated in thin, solid-state membranes.[17] The biological pores offer very low noise properties, but the high fragility of the conventionally used lipid bilayer membrane as a supporting structure limits their lifetime and the voltages that can be applied, thus restricting some applications. On the other hand, solid-state nanopores present increased durability over a wider range of experimental conditions, such as applied voltages, temperature and pH, and their size is tunable *in situ*.[18] In principle, solid-state nanopores offer a greater propensity to be integrated into robust lab-on-a-chip devices as arrays. In fact, recent studies revealed various integration strategies which embed such nanopores within microfluidic networks.[19–22] The nanopores used in these investigations are typically constructed in an ultrathin (10-nm to 50-nm) dielectric membrane (e.g. SiN) using high-energy ion or electron beams.[23,24] However, the use of FIB or TEM to fabricate nanopores introduces integration challenges. The need for direct line-of-sight access when drilling with beams of energetic particles demands that nanopores be fabricated before their integration within microfluidic devices. This imposes strict alignment requirements during both nanopore fabrication and device assembly, resulting in challenges that limit the yield of functional devices, particularly for array formation on a single membrane or when the dimensions of the microchannels are reduced in order to minimize electrical noise. More generally, these conventional nanofabrication techniques rely on the production of nanopores in a vacuum environment, which inevitably introduces handling risks and wetting issues when transitioning into aqueous solutions for biosensing experiments.

Kwok *et al*[25] have recently proposed an alternative method of fabricating solid-state nanopores reliably using high electric fields, referred to as nanopore fabrication by controlled breakdown (CBD). *In situ* and under typical experimental biological sensing conditions (e.g. in 1 M KCl), a dielectric breakdown event is induced in the supporting intact insulating membrane resulting in the formation of a single nanopore with a diameter as small as 1-nm in size but tuneable to large sizes with sub-nm precision.[18,26] The simplicity of the CBD method lends itself well to the integration of nanopore sensors within complex microfluidic architectures and to potential lab-on-a-chip devices. Combining the advanced sample handling and processing capabilities inherent in microfluidic devices with *in situ* nanopore fabrication is expected to mitigate various integration issues and expand the range of applications.

In this work, we demonstrate that CBD can be used to fabricate a 5×1 array of solid-state nanopores, which are individually addressable both fluidically and electrically, directly in an enclosed microfluidic environment. Importantly, by controlling the electric potential in each polydimethylsiloxane (PDMS) microchannel independently, the electric field can be confined to specific regions of a single SiN membrane. We present two microfluidic configurations: a standard 5-channel device in which the entire membrane is exposed to solution along the length of each microchannel, and a second in which only a small, localized region of the membrane is exposed using microfluidic vias. In validating the integration of nanopores within these microfluidic architectures, we characterized the noise properties of the devices and their ability to detect the translocation of individual biomolecules. As a proof-of-concept, double-stranded DNA (dsDNA) and human α-thrombin protein were detected.

3.4 Experimental

Commercial silicon chips (3-mm frame size) possessing an exposed 500×500-µm^2, 20-nm thick SiN membrane (SiMPore Inc. SN100-A20Q05) were mounted between PDMS microfluidic channel arrays of differing architectures. While arrangements of one, two and three channels were also explored, the devices presented herein utilized geometries containing five independently addressable microchannels on one side of the membrane, while the other side of the membrane was accessed by a single common microchannel (Figure 3-2). The first layout (Figure 3-2(a) and 3-2(b)) is an array of five microchannels consisting of broad 200-µm wide channels (50-µm height) tapering over the membrane to a 15-µm width. Each of the five independent channels is separated from one another by 25-µm. The second microfluidic configuration was designed to localize nanopore formation by CBD in each microchannel at the center of the membrane, and to further reduce high frequency electrical noise by minimizing the area of the membrane exposed to the ionic solution. In this second configuration, a 200-µm thick layer of PDMS with an array of rectangular apertures, varying in length from 40-µm to 120-µm with a constant width of 15-µm, was used to form microfluidic vias linking the microchannels to a well-defined area over the center of the membrane (Figure 3-2(c) and 3-2(d)). This layer was then bonded to the array of five independent PDMS microchannels as in the initial design.

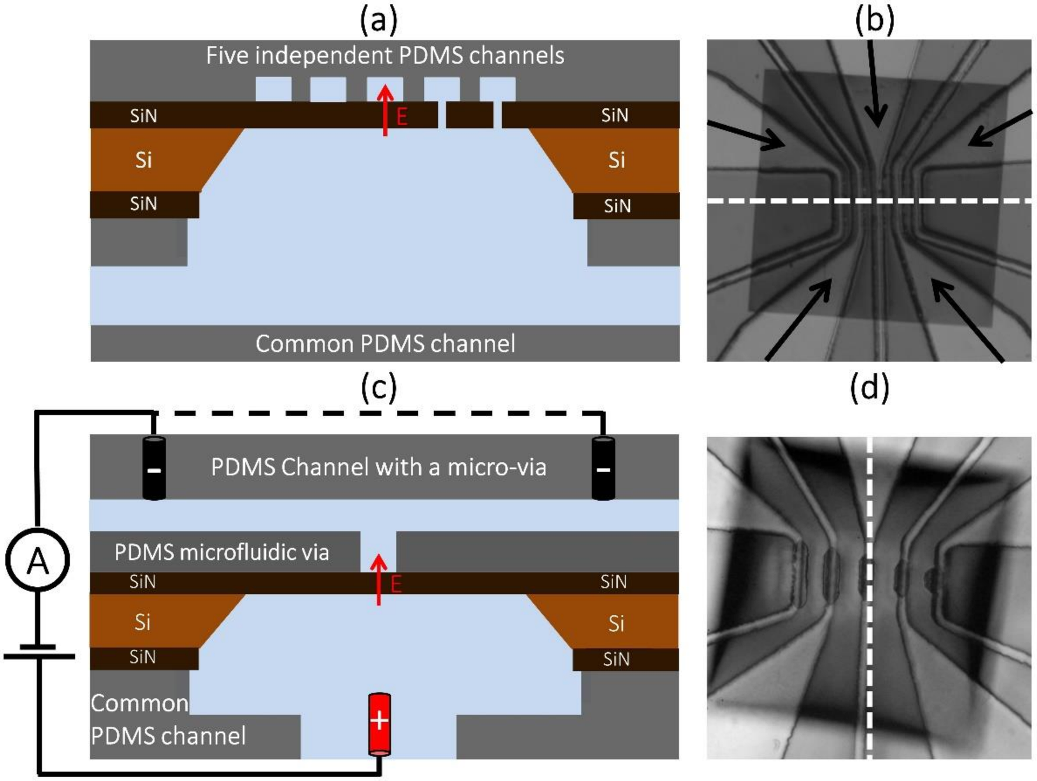

Figure 3-2 Cross-section schematics of **(a)** a five-channel device and **(c)** a channel in a device with a micro-via layer confining the electric field and electrolyte to a precise location on the membrane (images not to scale). A second electrode (dashed line in **(c)**) can be added to produce a symmetrical electric field in the independent (top) channel. **(b)** and **(d)** Reflected optical images under a stereomicroscope of devices with five microfluidic channels situated directly on a SiN membrane and isolated from the membrane by a micro-via layer, respectively. The white dashed lines in (b) and (d) indicate the orientation of the cross-sectional views in **(a)** and **(c)**, respectively.

Each layer (micro-via, five-channel, and common channel layer) was fabricated by soft lithography using PDMS (Sylgard 184 from Dow Corning at a 7:1 (w/w) ratio), patterned from a master mould prepared by photolithography.[27] In all configurations, the bottom layer consisted of a ~3-mm thick layer of PDMS containing a single 250-µm wide by 100-µm high fluidic channel bonded to a glass slide (oxygen plasma bonding, AutoGlow Research). In order to allow fluidic access to the nanopores, a 2-mm hole was hand-punched through this common bottom microchannel over which the etched side of the silicon chip was seated. A thin layer (100 ±10-μm) of PDMS was then spin-coated around the chip to compensate for the thickness of the silicon chip and to leave a smooth, sealed surface upon which the multiple microchannels could be bonded. After spin coating, this thin PDMS layer was cured on a hot plate at 80°C for 20 minutes. Figure 3-6 provides more detailed description and schematic of the microfabrication schemes.

In order to allow fluidic and electrical access to the microchannels, holes were also punched through each of the top fluidically separated and bottom common channels prior to bonding to accommodate tight fitting of Ag/AgCl electrodes and PEEK tubing flowing electrolyte solution. By placing the electrodes ~5-mm from the centre of the membrane, the resistance of the microchannel leading up to the nanopore is limited to ~100 kΩ in 1M KCl electrolyte solution, less than ~1 % of the total electrical resistance of a device containing a nanopore with a diameter of 10-nm.

Immediately prior to introducing aqueous samples into the microchannels, the assembled device was treated with oxygen plasma for 5 minutes at 70 W to increase microchannel hydrophilicity.[28] The microchannels were then connected to sample vials with polyethylene tubing and flow was initiated by pressurizing the vials using high-precision pressure regulators. Effective sealing (>10 GΩ) between microchannels was tested prior to nanopore fabrication by flowing 1 M KCl solution (pH 7.5) and attempting to measure the ionic current between microchannels under a moderate applied voltage (0.2 V – 1 V).

3.5 Results and discussion

Individual nanopores were fabricated by inducing a discrete dielectric breakdown event in each of the independent microfluidic channels integrated over the membrane. Briefly, this was done by applying high electric fields using custom-build electronic circuitry.[25] A potential difference ranging from 10 V to 14 V was applied to one of the independent microchannels relative to the grounded common microchannel to fabricate a nanopore in minutes or seconds.[26] This potential difference induced a leakage current through the SiN membrane, which is monitored in real-time (Figure 3-3(a)). The formation of a single nanopore is detected by the sudden and abrupt increase of the leakage current past a pre-defined threshold, whereby the applied voltage was cut off with a response time of 0.1 s. While the threshold current and response time can be varied to achieve a desired resultant nanopore size following the breakdown event, those discussed here were typically sub-2-nm in diameter (tight cut-off conditions). This process is then repeated in each top fluidically separated microchannel resulting in independently addressable nanopores on a single membrane but located in different microfluidic channels. Following nanopore fabrication, sensitive measurements for electrical characterization and single-molecule sensing were performed using an Axopatch 200B (Molecular Devices) low-noise current amplifier.

In order to obtain nanopores of the desired size for the detection of specific biomolecules, each nanopore was fabricated as described above and then conditioned using high electric fields shaped by the application of alternating -5 V and +5 V pulses across the membrane (Figure 3-8). This treatment was used to optimize the electrical noise properties and rejuvenate clogged nanopores for further experiments with comparable results to those reported in previous studies which used macroscopic fluidic reservoirs.[18,29]

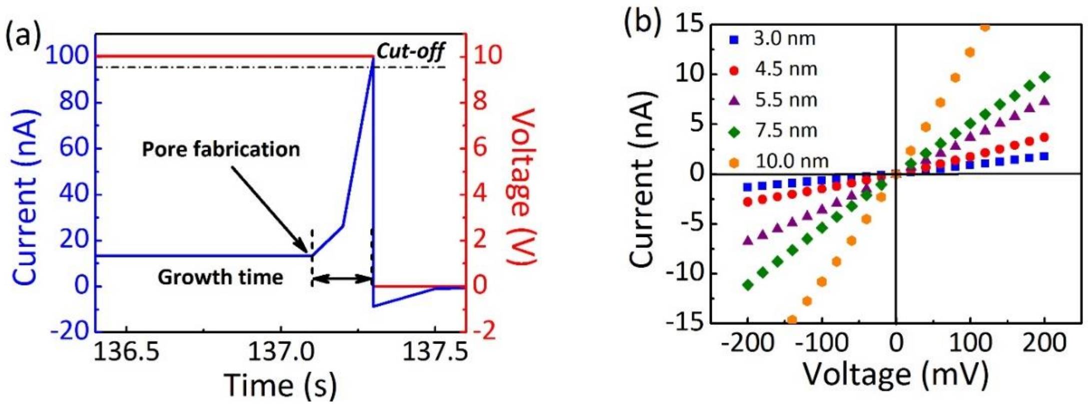

Figure 3-3 **(a)** Leakage current through the SiN membrane a few seconds before nanopore fabrication by CBD at 10 V. The instant of nanopore fabrication is characterized by a sudden increase in current. **(b)** Current-voltage (I-V) curves used to infer nanopore diameter using a conductance-based model for 5 independently fabricated nanopores on a single five-channel device.

To infer the diameter of each nanopore fabricated by CBD, its conductance *G* was measured directly in solution by monitoring the ionic current passing through each nanopore as an applied potential difference was swept from -200 mV to +200 mV. By assuming a cylindrical geometry and accounting for access resistance,[30] the effective diameter, *d*, of the nanopore can be calculated from its conductance by the following relationship:

$$G = \sigma \left(\frac{4L}{\pi d^2} + \frac{1}{d} \right)^{-1} \tag{3.1}$$

In Equation 3-1, σ is the bulk conductivity of the electrolyte and L is the effective length of the nanopore, assumed to be equal to the nominal thickness of the SiN membrane. The current-voltage (I-V) curves in Figure 3-3(b) display an ohmic response in 1 M KCl pH 7.5 ($\sigma = 10.1 \pm 0.1$ $\mathrm{Sm^{-1}}$) for five independently formed nanopores ranging in size from 3-nm to 10-nm in a single five-channel device. The error incurred by ignoring the contribution from surface charge in Equation 3.1 affects the accuracy of the effective calculated nanopore diameter by <0.5-nm for the high salt concentrations used here,[26] while the error attributed to the values of the electrolyte conductivity and the membrane thickness affects the uncertainty of the nanopore diameter by ~0.3-nm.

To further characterize performance, power spectral density plots (PSDs) of the ionic current were acquired for nanopores fabricated in each of the two microfluidic architectures (Figure 3-4(a)). While low-frequency noise (below 1 kHz) is typically of the 1/*f*-type, higher frequency noise is governed by the dielectric properties and capacitance of the device arising from the surface area exposed to the electrolyte solution.[31] Thus, minimizing the surface exposed to the solution leads to a reduction in this high-frequency noise, which significantly improves the signal-to-noise ratio during biomolecule sensing at high bandwidth.[22] This is illustrated in Figure 3-4(a), where both 5-channel devices (with and without micro-vias) are compared to a nanopore chip mounted in between fluidic reservoirs in a standard macrofluidic cell. In this high frequency range, the 5-channel microfluidic device (without the micro-via) exhibits comparable noise characteristics to those acquired in the macroscopic cell. This result is consistent with the argument that noise in this regime arises from the amount of exposed membrane area calculated to be ~3×10^5 μm^2 for the macroscopic reservoir and ~2×10^5 μm^2 for a microchannel in the standard 5-channel device. However, when the exposed membrane area is reduced 350-fold to ~6×10^2 μm^2 using the smallest micro-via (40×15-μm^2) of the 5-channel device, high frequency noise is significantly reduced. This noise reduction is further highlighted by the baseline ionic current traces of each device while no voltage applied shown in Figure 3-4(b), where the peak-to-peak noise at 100 kHz bandwidth is reduced by a factor of 2 (5 at 10 kHz bandwidth) in the configuration with micro-vias, while the RMS noise is reduced by a factor of 7 at 10 kHz and 2 at 100 kHz bandwidth (see Figure 3-9).

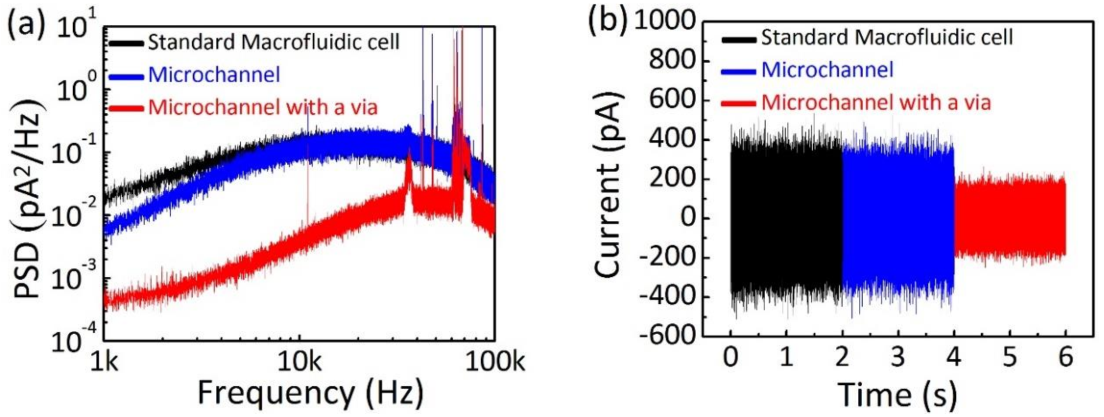

Figure 3-4 **(a)** Power spectral density (PSD) noise comparison. **(b)** Current traces in a macroscopic cell (black), five-channel device (blue) and five-channel device with micro-vias (red). All measurements were done in the absence of any fabricated nanopore at no applied voltage, sampled at 250 kHz and low-pass filtered at 100 kHz by a 4-pole Bessel filter in 1 M KCl pH 7.5.

The functionality of these devices was assessed by observing the translocation of biomolecules (Figure 3-6). In each case, nanopores were first fabricated and enlarged to a desired diameter as described above. Following sample introduction, flow was minimized in the microchannels by turning off the pressure regulators. Figure 3-5(a) shows a scatter plot of the conductance blockages and durations as individual human α-thrombin (Haematological Technologies, Inc.) molecules at 250 µM concentration are detected using a 10.5-nm nanopore in a microfluidic channel (without vias) in 1 M KCl pH 8.0. Here, protein molecules were loaded in one of the five independent top microchannels, which was biased at -200 mV relative to the grounded common bottom channel. Overall, over 5,000 individual events were observed. Figure 3-5(b) shows a similar scatter plot of DNA translocation events through a different 11.5-nm nanopore, which was localized within a microchannel that included a micro-via. Here, a 3 pM solution of 10-kbp dsDNA in 2 M KCl pH 10 was added to the top microchannel while -200 mV, -250 mV and -300 mV biases were applied relative to the common channel, resulting in over 1,500 translocation events. It is worth noting that the magnitudes of the conductance blockages obtained for both protein and single-level dsDNA events (They are ~4.5 nS and ~3.2 nS respectively in Figure 3-10 and Figure 3-12), are in agreement with previously reported models and experiments utilizing standard macrofluidic cells.[30,32]

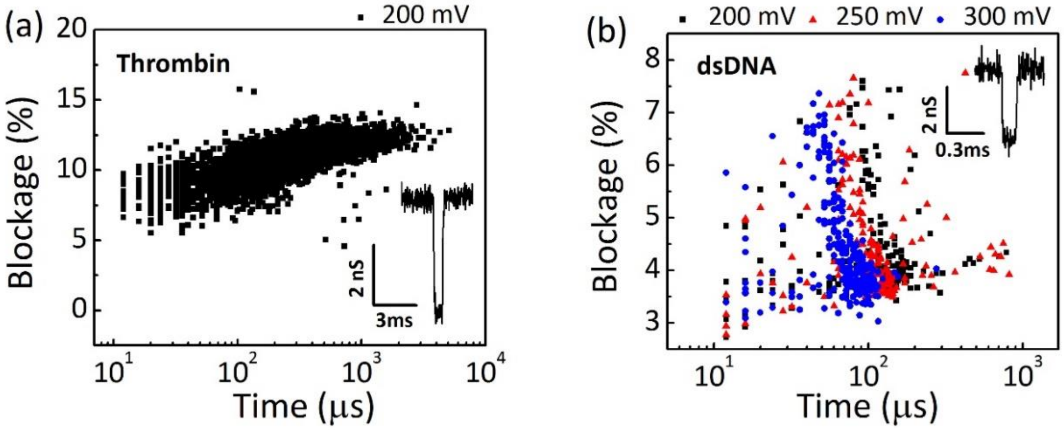

Figure 3-5 Scatter plots of the normalized average current blockade (0% representing a fully opened pore, and 100% a fully blocked pore) versus the total event duration of **(a)** human α-thrombin detection using a 10.5-nm pore for -200 mV applied voltage, and **(b)** 10-kb dsDNA translocation through a 11.5-nm pore at -200 mV (black squares), -250 mV (red triangles) and -300 mV (blue circles). Each data point represents a single event. The insets show transient current blockades as biomolecules interact with the nanopore. For clarity the data were multiplied by -1 in the insets.

The microfluidic design must be considered carefully when integrating nanopores using this approach. While nanopores integrated within microfluidic channels placed directly on the membrane (without a micro-via) were able to capture and detect proteinaceous samples in 30% of the devices tested (9 out of 30), the capture efficiency and experimental yield of devices capable of demonstrating nucleic acid translocation were markedly reduced. Here, the criteria we use to defined experimental yield is a device capable of detecting more than 1000 biomolecular translocation events. It is important to note that the placement of the electrodes inside microfluidic channels leading to the membrane introduces asymmetry in the electric field at the membrane and near the nanopore when the top microchannel contains only a single electrode. It is possible that this asymmetry results in the fabrication of a nanopore near the edge of the membrane (near the edge of the silicon support chip), a region that may be more stressed upon bonding to the PDMS microchannel layer. In this region, the surface charge characteristics of the membrane in the vicinity of the nanopore may electrostatically prevent the translocation of large, highly charged nucleic acid polymers while allowing the passage of less-charged polypeptides. The introduction of a micro-via, however, localizes nanopore fabrication to an intended region in the center of the membrane or away from the edges and ensures a more symmetrical electric field (as noted via finite-element modeling in Figure 3-7), yield to 3 out of 4 devices tested in pH 10. It is also possible to reduce this asymmetry in the electric field by incorporating pairs of electrodes biased at the same potential, in the top independent channels on either side of the membrane. In this configuration, 5 out of 6 devices tested in pH 8 were successful in detecting at least 1000 biomolecular translocation events (further detail can be found in Section 3.8).

3.6 Conclusions

In this work, we present a versatile strategy in which solid-state nanopores can be fabricated *in situ* in various microfluidic environments. Using the CBD method to integrate nanopores in lab-on-chip devices greatly simplifies the fabrication and assembly process. The inclusion of microfluidic vias is important in localizing the nanopores to specific regions of the membrane, while also reducing the electrical noise during high-bandwidth recording and maximizing the sensor's detection efficiency. Interestingly, sharing a common microchannel with an array of independently addressable nanopores increases the number of potential applications. For instance, a precious sample can be introduced to the common channel and interrogated using differently sized or functionalized nanopores in series or in parallel. Or, should the performance of a particular nanopore degrade, a neighbouring nanopore of the same size can be used to continue an experiment on the same device without the need for re-introducing the sample. Alternatively, different samples can be introduced into different microfluidic channels for multiplexed analysis on a single device. Examples of such experiments can be found in Section 3.8. This fabrication approach and this integration strategy are highly scalable and the creation of larger arrays of nanopores will be possible by adapting the membrane design and packing them accordingly.

3.7 Acknowledgements

This work was supported by the Natural Sciences and Engineering Research Council of Canada (NSERC), the Ontario Ministry of Research and Innovation, and the Canada Foundation for Innovation.

3.8 Supplementary Information

3.8.1 Materials and microfabrication protocols

The devices presented integrate commercially available silicon nitride (SiN) membranes (SN100-A20Q05, SiMPore Inc.) within microfluidic devices made of polydimethylsiloxane (PDMS). PDMS layers were replicated from a master mould fabricated by soft lithography[27] and made of SU8-2050 photoresist (Microchem Inc.) on a silicon wafer. Each microfluidic layer (microfluidic via, independent and common channel layers) was fabricated using different spin speeds, baking time and temperature, UV exposure and developing times depending on the final desired thickness (height) of the resultant features (Table 3-1).

Table 3-1 Protocols for master mould fabrication

Independent (top) channel layer (50µm height)				
Spin	**Soft Bake**	**UV exposure**	**Post Bake**	**Developing**
5 s @ 500 rpm	1min and 30 s@ 65 ^{0}C 7 min @ 95 ^{0}C	11 s	1min and 30 s @ 65 ^{0}C 6 min and 30 s @ 95 ^{0}C	5 min
30 s @ 3000 rpm				

Common (bottom) channel layer (100 µm height)				
Spin	**Soft Bake**	**UV exposure**	**Post Bake**	**Developing**
5s @ 500 rpm	5 min @ 65 ^{0}C 16 min @ 95 ^{0}C	15 s	4 min @ 65 ^{0}C 9 min @ 95 ^{0}C	8 min
30s @ 1700 rpm				

In order to construct a 200 µm high feature for the microfluidic via layer, a 100-µm thick layer of SU8-2050 photoresist was first spun (Laurell Spin Coater) on a wafer**.** Following a first soft bake, this process was repeated to double the layer thickness.

Microfluidic via (200 µm height)						
Spin	**Soft Bake**	**Spin**		**UV exposure**	**Post Bake**	**Developing**
1st Layer		**2nd Layer**	**Soft Bake**			
5 s @ 500 rpm	5 min @ 65 ^{0}C 16 min @ 95 ^{0}C	5s @ 500 rpm	7 min @ 65 ^{0}C 40 min @ 95 ^{0}C	20 s	5 min @ 65 ^{0}C 13 min @ 95 ^{0}C	16 min
30 s @ 1700 rpm		5s @ 1700 rpm				

Following the fabrication of each master mould, wafers were first treated with aminosilane to facilitate PDMS removal. PDMS (7:1 (w/w) base:curing agent for all layers) was then poured over the master mould for each channel layer, followed by degassing in a vacuum chamber for 30 minutes and baking at 80°C for 2 hours. The cured PDMS was then peeled off the mould to create the microchannel structure. Individual device components were then cut out and access holes for fluid and electrode introduction were punched through the independent channels (0.75 mm OD for fluidic tubing and 1.25 mm OD for electrodes). A 2.0 mm hole also was hand-punched in the middle of each common microchannel to allow fluidic access to the bottom of the chip. The silicon chip (etched side) was then bonded to the common channel layer atop the punched hole using oxygen plasma (Glow Research AutoGlow). All plasma bonding steps were performed at 30 W for 30 seconds.

In order to compensate for the thickness of the silicon chip and leave a levelled, smooth surface for bonding of the independent (top) channels in both configurations (with and without microfluidic via layers), a thin layer (~100 ± 10 µm) of PDMS was spun around the chip (5 seconds at 500 rpm followed by 10 seconds at 1000 rpm). This thin layer was cured directly on a hot plate at 80°C for 20 minutes.

To fabricate thin (~200 µm) microfluidic via layers upon which independent channels could be bonded, degassed PDMS was spun on its master mould (5 seconds at 500 rpm followed by 10 seconds at 800 rpm) and cured directly on a hotplate at 80 °C for 30 minutes. In order to precisely situate microfluidic vias and independent channel layers atop the SiN membrane, all alignment steps were done using an OAI DUV/NUV mask aligner (Model 206). Figure 3-6 schematically describes the steps of mounting the silicon chip between the PDMS layers.

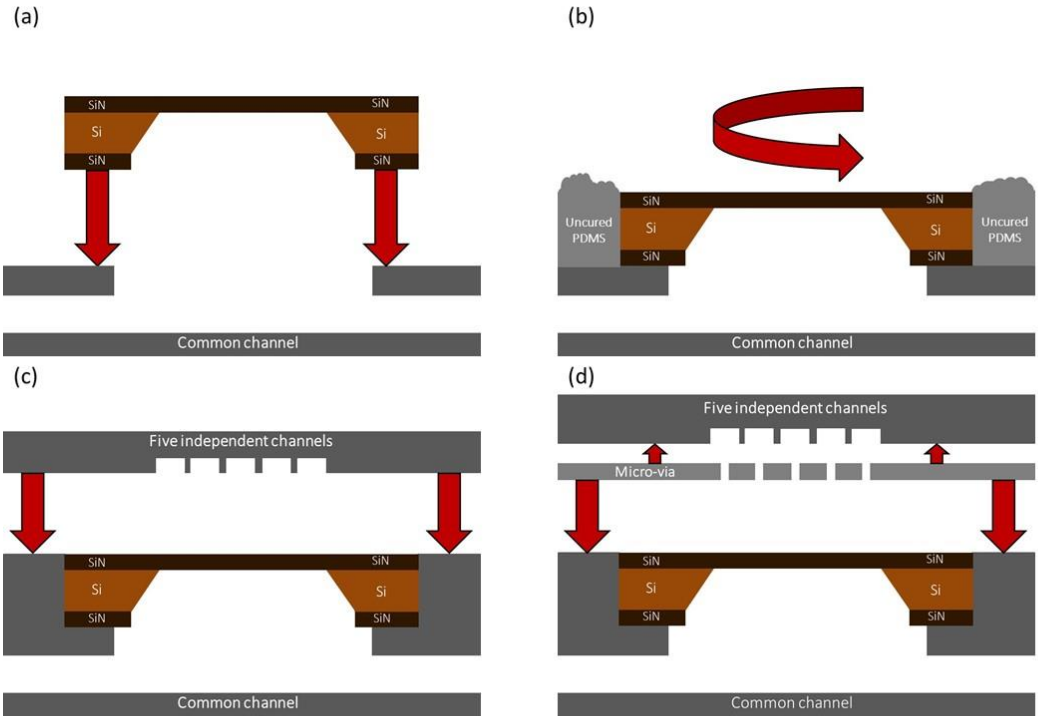

Figure 3-6 Schematic overview of the procedure to mount a silicon chip between the PDMS layers. **(a)** Following the plasma treatment, etched side of the silicon chip is brought into contact and bonded to the ~3-mm thick common channel layer atop a hand-punched 2.0 mm hole. **(b)** A thin layer (~100 ± 10 µm) of PDMS is then formed around the chip using a spin coater to level its thickness. Once the thin PDMS layer is cured, the five independent microchannels are **(c)** directly or **(d)** with the micro-via layer aligned over and permanently bonded to the silicon nitride membrane.

Once the device was bonded, access holes were punched through the entire assembly to allow electrical and fluidic access to the common (bottom) channel. Finally, the common channel was bonded to a clean glass slide (Fisher Scientific).

3.8.2 Experimental setup

Each nanopore was fabricated *in situ* by controlled breakdown (CBD)[33]. In order to create the high electric fields necessary for nanopore creation, custom-build electronic circuitry and external power supplies were used – for more detail see supplementary information of Reference [25]. Briefly, op-amps were used to amplify a software-controlled voltage generated by a data acquisition (DAQ) card (National Instruments USB-6351), which was then applied across the SiN membrane. The leakage current through the membrane was then recorded and monitored in real-time using a LabView program. Once the leakage current surpassed a pre-defined threshold, the applied potential was removed. This same circuitry was also used to apply alternating pulses of moderately high voltage for nanopore enlargement and conditioning.[18,29] Nanopore fabrication and conditioning were performed in 1 M KCl solution buffered with HEPES at pH 7.5 ± 0.1 ($\sigma = 10.1 \pm 0.1$ Sm^{-1}). Conductivity and pH of the solution were measured using a VWR symphony pH/conductivity meter (SB80PC) prior to experiment.

Sensitive low-noise measurements for nanopore characterization and single-molecule sensing were performed using an Axopatch 200B (Molecular Devices) current amplifier. Ionic current was sampled at 250 kHz and low-pass filtered at 100 kHz using a 4-pole Bessel filter. For such measurements, the current amplifier gain was set to 1 V/nA. All electronic measurements were controlled and recorded using LabView software via the DAQ card and carried out inside a grounded Faraday cage at room temperature.

Aqueous electrolyte solutions (with or without biomolecule samples) were introduced to the microchannels and nanopore using pressure-driven flow. Solution-containing vials were placed inside the Faraday cage and connected to the microfluidic networks via polyethylene tubing. Flow was then established using pressure regulators (Marsh Bellofram Type 10) and solenoid valves (SMC S070C-SDG-32), located outside of the Faraday cage and controlled by LabView software.

3.8.3 Electrical resistance of the microchannels

The micro-scale dimensions of the fluidic network leading up to the SiN membrane pose limitations on electrode placement. In macroscopic systems, the electrolyte solution separating a nanopore and electrodes contributes a negligible amount of electrical resistance to the system. When confined within microchannels and tubing, however, the electrolyte can contribute additional access resistance, reducing the device sensitivity and response time for detecting the small ionic current fluctuations produced by molecular translocations. For this reason, Ag/AgCl electrodes (In Vivo Metric) were placed as close to the SiN membrane as possible (~3 mm to ~5 mm to the center of the chip) without damaging the membrane upon electrode insertion or device handling.

In order to insulate the Ag wire of the electrodes, they were first encased in polyethylene tubing (OD) with the tips barely protruding from the tubing. The electrode assembly was then sealed by filling the tubing with PDMS and inserted it into the punched holes in the PDMS devices. Given this electrode placement as well as the dimensions of the microfluidic vias and all microchannels, access resistance in the devices presented was minimized to ~130 kΩ. This corresponds to <0.1 % of the total resistance of a 10-nm pore in 1 M KCl (~150 MΩ).[30] As such, the nanopore itself provided the dominant source of electrical resistance in the system, ensuring sensitive electrical measurements.

3.8.4 Electrical field in micro-via and non-micro-via devices

In order to understand the effects of adding a micro-via layer to the microfluidic configuration, finite element modeling of the electric field in both device geometries (with and without a microfluidic via) was explored. Device configurations were generated in 2D and electric fields were modeled using a stationary study within the Electric Currents module of COMSOL Multiphysics Modeling Software. Both geometries were examined first with an intact membrane (no aqueous connection across the membrane) and then with a nanopore (20-nm fluidic conduit through the membrane).

Briefly, geometries consisted of a chip and membrane of the same dimensions as those used in the experimental portion of this study (20-nm thick SiN layer on both sides of a 100-µm thick Si support, total width of 3 mm). A 500-µm wide portion of the membrane was exposed through an etch pit. Both configurations shared the same common channel design consisting of a 6 mm long and 100-µm high microchannel connected to the chip by a 2.0 mm wide by 3 mm high punched hole. A single independent channel (6 mm long by 50-µm high) was either placed directly on the membrane side of the chip (for the device that did not contain a microfluidic via) or separated from the membrane by a microfluidic via (300-µm wide, 200-µm high) that was situated in the center of the membrane away from the edges of the Si support chip. To model a simple nanopore, a 20-nm gap was left in the centre of the SiN layer to connect either side of the membrane.

Material properties assigned to the respective portions of the design were those inherent in the built-in materials used (liquid water, SiN and silicon). Electrical conductivities for the SiN membrane and aqueous solution filling all microchannels, nanopores and fluidic vias, however, were assigned based on experimentally measured values for each material. An electrical conductivity of 2 × 10^{-9} Sm^{-1} was found for SiN by measuring the amount of leakage current under a 10 V bias through a blank membrane, embedded in a device containing a microfluidic via of a known area. The conductivity of the aqueous solution was that of the 1 M KCl solution used in experiments (10.1 Sm^{-1}). PDMS defining the microchannel walls was approximated as an insulating boundary along the contour of the entire design, while electrodes were simulated by applying a potential of either 10 V (for intact membranes) or 200 mV (devices containing nanopores) to the left-most boundary of the independent channels (3 mm away from the center of the membrane). The corresponding boundary in the common channel was defined as ground.

In order accommodate the vastly different length scales of the geometry (nano-scale pores and membranes to millimeter-length channels), the meshing was set to 1 point per 2 nm on the boundaries within 1 µm of a nanopore. The mesh size was then swept along the length of the membrane and outwards from the nanopore, where the remaining geometry was filled using extra-fine free triangular meshing.

Figure 3-7 shows the geometry of a device with the independent microchannel placed directly on the membrane (a) and the device containing a microfluidic via (b). Both devices contain a 20-nm pore in the centre of the membrane. A zoom of the area surrounding the nanopore in Figure 3-7(d) shows that the electric field in the immediate vicinity of the nanopore in the microfluidic via configuration is quite symmetric. This is highlighted by the fact that the intensity of the electric field decays uniformly away from the nanopore on either side of the membrane. Furthermore, the electric field lines are symmetric from left to right despite the fact that both electrodes are placed 3 mm to the left of the nanopore. Conversely, Figure 3-7(c) shows that the electric field lines are quite asymmetric under the same conditions in a device without a microfluidic via. Both the electric field lines and the field intensity differ both across the membrane and from left to right in the independent (top) microchannel.

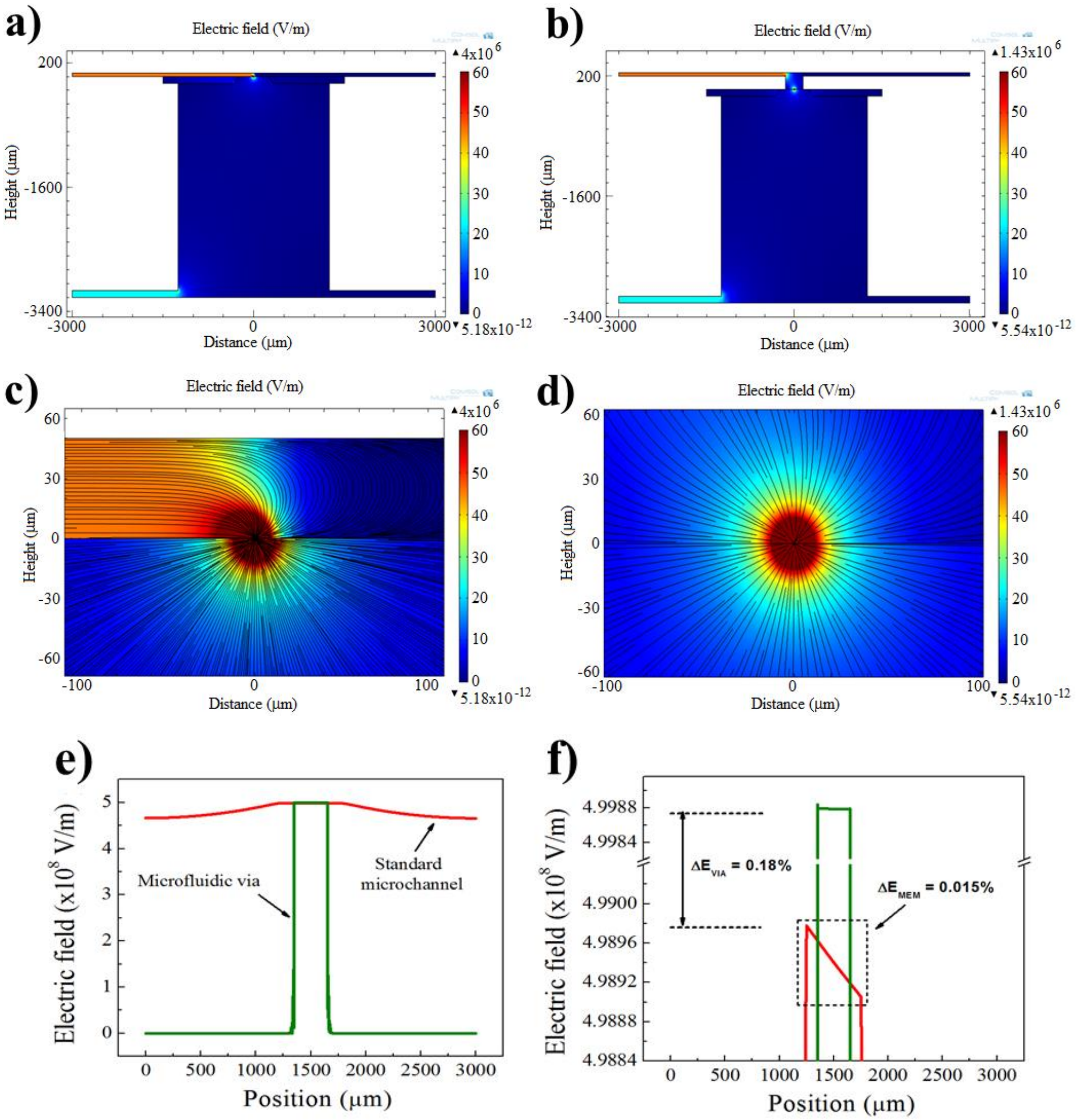

Figure 3-7 Finite element modelling of the electric field within microfluidic nanopore devices: **(a)** and **(b)** 2D geometries representing the entire fluidic system, including a 20-nm pore in the centre of the membrane, with and without a microfluidic via, respectively. A potential of 200 mV is applied to the left wall of the top (independent) microfluidic channel, while the left wall of the bottom (common) channel is designated as the ground. **(c)** and **(d)** Zooms of the electric field surrounding the nanopores shown in **(a)** and **(b)**, respectively. In the device without a microfluidic via, the electric field lines are asymmetric both across the membrane and from left to right across the nanopore. When a microfluidic via layer is added, the electric field becomes symmetric. **(e)** The magnitude of the electric field measured along the plane mid-way through the SiN membrane when a potential difference of 10 V is applied (as in nanopore fabrication). The presence of a microfluidic via, both localizes the electric field and renders it uniform across the exposed membrane. **(f)** The device without a via exhibits a somewhat lower electric field than that in a device with a via, which decreases with distance away from the electrode.

Further investigation of the electric field shape in these configurations shows that nanopore fabrication using CBD may also be affected by asymmetric placement of electrodes. Figure 3-7(e) and (f) shows the magnitude of the electric field though a horizontal cross section of an intact membrane in devices with and without microfluidic vias. In this example, a potential difference of 10 V was applied across the membrane as described above in order to simulate the nanopore fabrication conditions used in practice. While the device containing a microfluidic via exhibits a uniform electric field across the length of the exposed membrane, the device in which the independent (top) microchannel is placed directly on the membrane exhibits a stronger electric field closer to the side where the electrodes are placed.

3.8.5 Tune the size of fabricated nanopore

Following the nanopore fabrication procedure, we used high electric fields shaped by the application of alternating -5 V and +5 V 2-s pulses across the membrane. This allowed the nanopore size to be precisely tuned, for a particular sensing application, directly in the electrolyte solution.[18,29]

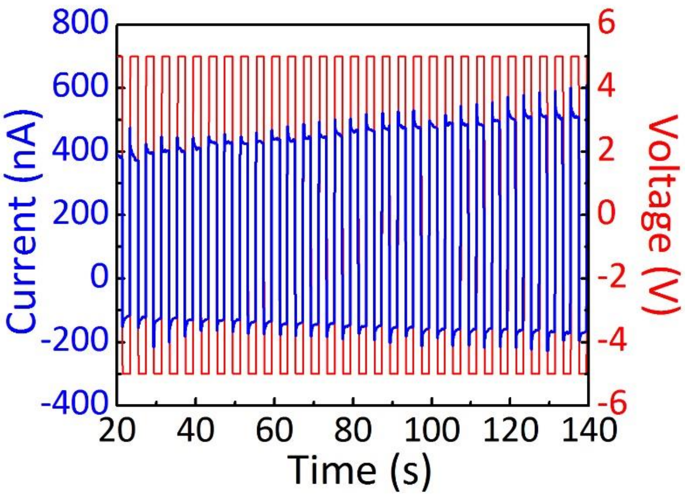

Figure 3-8 Enlargement of a nanopore using high electric fields produced by alternating pulses of ±5 V. Note that the current at this potential is non-ohmic.

3.8.6 High frequency noise reduction

Enhanced bandwidth in ionic current recordings and improved signal to noise ratio (SNR) are among the major topics of interest for furthering the development of nanopore sensors. The noise present in solid-state nanopore measurements can very broadly be classified as low-frequency (<10 kHz) and high frequency (>10 kHz). In the low-frequency regime, flicker noise is dominant and can vary with properties of the nanopore itself. High frequency noise, on the other hand, arises from the dielectric properties of the nanopore chip and electronics used for measurements.[34–36]

Attempts to mitigate noise issues in the high frequency regime have so far included techniques such as transfer printing of the suspended membranes directly on to PDMS channels[22], painting the chip with PDMS[35] and depositing other insulating layers such as silicon oxide on the nanopore membrane.[37] Such methods rely on minimizing the amount of parasitic capacitance of the device that gives rise to noise. In the microfluidic configurations presented in this work, we are able to reproduce these effects by confining the area of contact between the nanopore membrane and electrolyte solution using microfluidic channels. By further reducing the contact area using microfluidic vias, we are able to observe a significant decrease in the total capacitance of the dielectric membrane and achieve low-noise ionic current measurements.

In order to quantify the noise properties of our devices, we performed ionic current power spectral density analyses of SiN membranes in both microfluidic configurations (with and without microfluidic via layers) as well as in a standard macroscopic fluidic cell. Ionic current traces were recorded with an Axopatch 200B at no applied voltage, in the absence of any fabricated nanopores (intact membrane), and low-pass filtered using the internal 4-pole Bessel filter set to 100 kHz. While the PSDs related to each configuration are presented in the manuscript (Figure 3-4 (a)), here, in Figure 3-9, we also compare the RMS noise of each system as a function of bandwidth. This RMS noise is obtained by integrating the PSD over frequency.

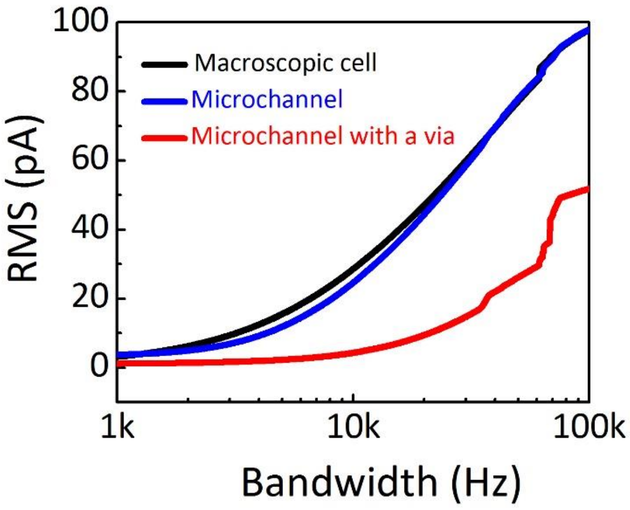

Figure 3-9 RMS noise comparison between 500×500 μm^2 SiN membranes in a macroscopic cell (black), a microchannel device (blue) and a device containing a X×Z μm^2 microfluidic via (red). Ionic current measurements were recorded over 30 s with no applied bias and low-pass filtered at 100 kHz. The exposed area of SiN membrane is reduced from ~3×10^5 μm^2 for a macroscopic cell to 600 μm^2 in a device with a microfluidic via.

While Figure 3-9 shows that the RMS noise of a nanopore in a device without a microfluidic via is comparable to that of a macroscopic cell, the nanopore in a microfluidic via device is significantly lower over the entire frequency range. For a 100 kHz bandwidth that is typically used for biomolecular sensing experiments, the RMS noise is reduced by a factor of 2 using this design.

3.8.7 Biomolecular translocation

The integration of solid-state nanopore arrays in microfluidic networks offers a platform that allows for a wide range of potential studies inaccessible to solid-state nanopore devices mounted in standard macroscopic fluidic cells. While the microfluidic architecture inherently introduces the ability of on-chip sample control and processing as well as requiring reduced sample volumes, the ability to fabricate multiple independent nanopores that share a common microchannel on a single device offers numerous additional advantages. As such, in addition to verifying the functionality of nanopores integrated in different microfluidic configurations for detecting biomolecular samples, we also performed a variety of experiments to explore the range of potential applications that could be targeted using this platform. As a proof-of-concept, we explored the ability of these devices to detect both protein and nucleic acid samples. For instance, a single sample of biomolecules (i.e. proteins or DNA) was introduced into the common bottom microchannel and interrogated sequentially using different nanopores without the need for introducing a new sample, a particularly attractive attribute for studying precious samples. In another scheme, a single nanopore can be used to study different samples introduced sequentially into one of the top independent microchannels.

In the following section, all protein samples (human α-thrombin) were introduced to the nanopore system at a concentration of 250 μM, while 10-kbp dsDNA was added at a concentration of 3 pM.

3.8.7.1 Protein

Proteins were reliably detected in both configurations presented (with or without microfluidic vias). A current trace of human α-thrombin translocating through a 10.5-nm pore (a scatter plot of which is presented in the manuscript Figure 3-5(a)) is shown in Figure 3-10(a)-(b). Protein sample (human α-thrombin) was introduced to in an independent channel in 1 M KCl buffered at pH 8.0 ± 0.1 while a -200 mV bias was applied relative to the common microchannel (ground). A histogram of the ionic current during translocation events is also shown in Figure 3-10 (c). Here, a distinct peak at a normalized current level of 1 indicates the open nanopore baseline and a broad peak corresponding to the blockage level of a protein molecule translocating through the nanopore is centered at 0.88. While a 5s ionic current trace and 150 ms zoom of translocation events are presented, similar events were recorded for over an hour without observing any deterioration of nanopore properties.

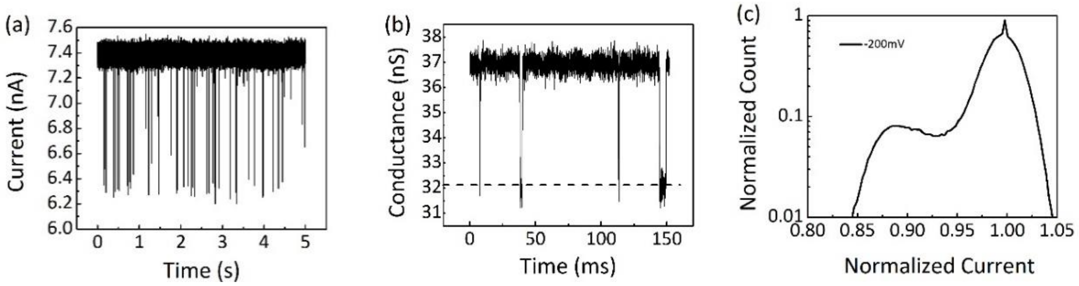

Figure 3-10 **(a)** Ionic current trace showing translocation events of human α-thrombin molecules in 1 M KCl pH 8.0 through a 10.5-nm pore in a 20-nm thick SiN membrane under an applied bias of -200 mV. **(b)** Zoom of typical translocation events. The dashed line indicates the typical ionic conductance level during translocation **(c)** Histogram of the ionic current level during translocation events normalized to the open nanopore baseline. A broad peak corresponding to a 12 % ionic current blockage is observed, consistent with what is expected for a 260 nm^3 object translocating through a nanopore of this size.

3.8.7.2 Nucleic Acid

By introducing the microfluidic via to the device architecture, the yield of successful dsDNA translocation experiments was significantly improved. While DNA detection was feasible in lower pH (such as pH 7.5 in Figure 3-11), nanopore performance in devices containing a micro-via was improved by working at higher pH.

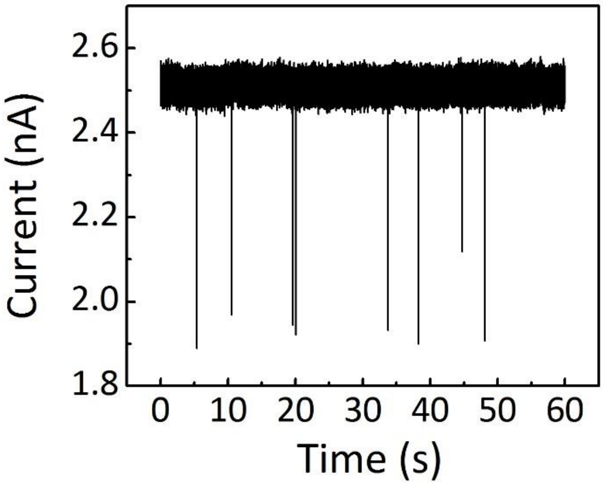

Figure 3-11 Ionic current trace at -200mV voltage bias showing 10-kb dsDNA fragments in 1 M KCl pH 7.5 translocating through a 5.5-nm pore in a device containing a microfluidic via layer. Data were multiplied by -1 for display clarity.

Figure 3-12 shows an example of ionic current traces of the scatter plot data presented in Figure 3-5(b). In order to confirm that nanopores fabricated using CBD in arrays of microfluidic channels exhibit expected capture rate trends and blockage levels upon translocation, three different voltage biases were applied across the nanopore (200 mV, 250 mV and 300 mV).

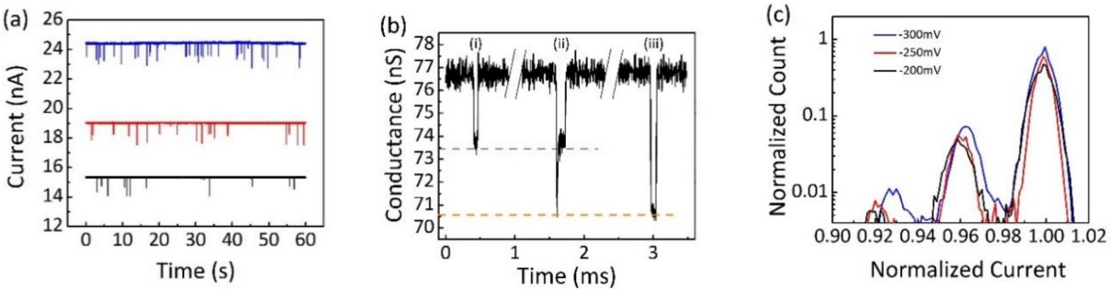

Figure 3-12 **(a)** Ionic current traces at various voltage biases showing 10-kb dsDNA fragments in 2M KCl pH10 translocating through an 11.5-nm pore in a device containing a microfluidic via. **(b)** Conductance traces of individual translocation events at 200 mV of **(i)** an unfolded (single-file), **(ii)** a partially folded, and **(iii)** a fully folded translocation event. The conductance of the open nanopore was ~76.7 nS and the dashed lines indicates the single blockage level (purple, 4.2%), and blockage level of a folded molecule (orange, 8%). **(c)** Histogram of the normalized current level (event current divided by the open nanopore current) revealing the expected blockage amplitude levels, which are in agreement with what is expected for this nanopore geometry.

As expected, capture rate increases as the voltage is increased, while the conductance change upon translocation is independent of the applied bias. Furthermore, the observed conductance blockages of 4.2 % and 8 % are in excellent agreement with what is expected for the translocation of dsDNA (single-file and folded, respectively) through an 11.5-nm pore.[30,32]

It is interesting to note that the ability of nanopores to detect translocating DNA at lower pH values (*e.g.* pH 8) which is improved by adding a second electrode to the top channel of a device. The symmetry in this configuration likely helps to produce a nanopore with desirable surface properties as well an electric field that favours the translocation of highly charged nucleic acid samples. Examples of DNA translocation at various voltages in a device with two top electrodes and a micro-via are shown in Figure 3-13.

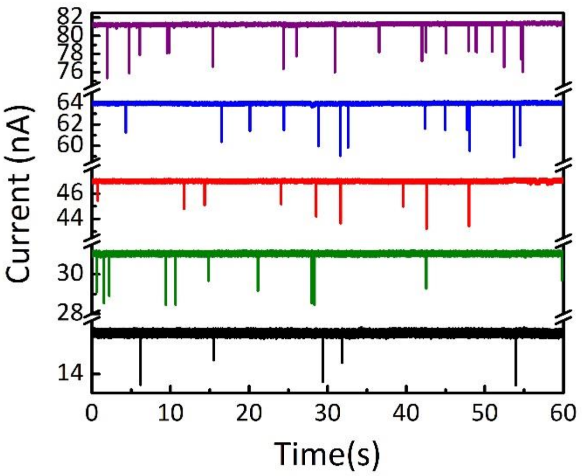

Figure 3-13 Typical ionic current traces showing 10-kb dsDNA in 3.6M KCl pH 8 translocating through a 14.0-nm pore in a device containing two top electrodes and a microfluidic via at voltage biases of 200 mV (black), 400 mV (green), 600 mV (red), 800 mV (blue) and 1 V (purple). Ionic current was sampled at 250 kHz and low-pass filtered at 100 kHz.

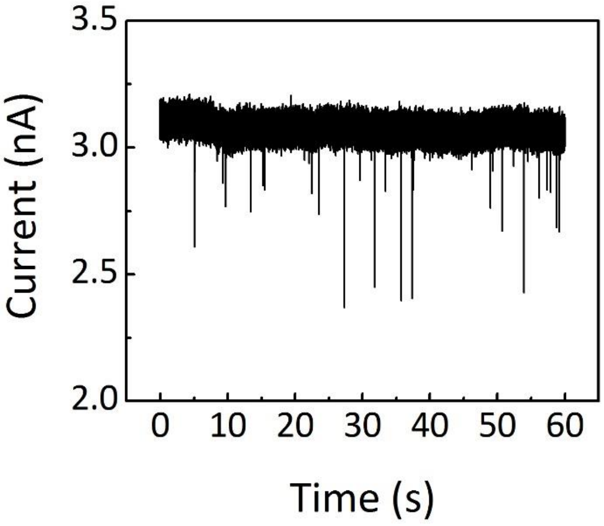

Figure 3-14 Ionic current trace at 500 mV bias of 50nt ssDNA in 3.6M KCl pH 8 translocating through a 3.5-nm pore in a device containing two top electrodes.

3.8.7.3 Serial probing of one sample through adjacent nanopores

Sharing a common microchannel with an array of independently addressable nanopores provides the opportunity for sequential sensing of one particular type of biomolecule through differently sized nanopores. This can be particularly useful for precious samples. For instance, a large nanopore can be used to extract information about the volume and charge of a biomolecule. Subsequent experiments could then be performed on a neighbouring nanopore that is smaller than the sample as a means of obtaining information about the kinetics of molecular unfolding. As a proof-of-concept, a solution of human α-thrombin in 2 M KCl pH 7.0 was loaded through the common channel of a device with two independent top channels on the other side of the membrane (without microfluidic vias). Each channel contained a nanopore fabricated by CBD followed by precise enlargement to 12.5-nm and 25.0-nm. The two independent top channels were also filled with the same buffer without the protein sample.

Figure 3-15 shows a 5 s ionic current trace of the detection of thrombin through each nanopore upon an applied voltage bias of -200 mV to the common channel (containing molecules). Measurements were performed sequentially. First, the independent microchannel exposing the 12.5-nm pore was grounded relative to the common channel. After 20 minutes of data acquisition, the current amplifier was then reconnected to an electrode embedded in the channel containing the 25.0-nm pore. Without flushing or requiring new sample, the experiment was then continued on the larger nanopore. As expected, the translocation blockage depth relative to the open pore current is decreased as molecules translocate though the larger nanopore.

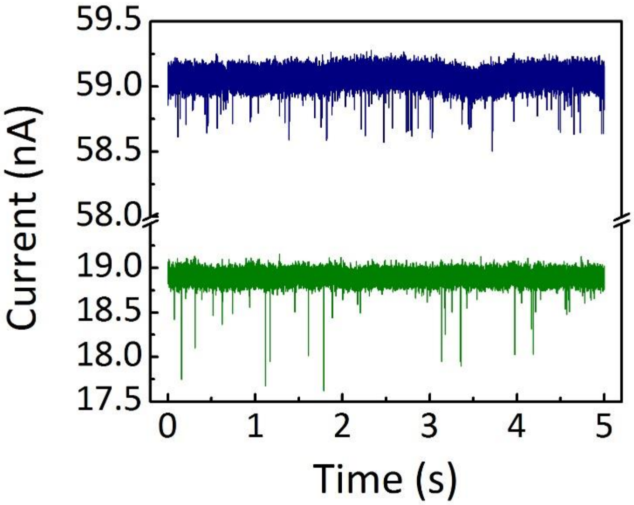

Figure 3-15 Current traces for human α-thrombin detection first through a 12.5-nm pore (green), and later through a 25.0-nm pore (blue) in the same device (without a microfluidic via layer). The sample was introduced to the bottom (common) channel while -200 mV was applied relative to the grounded independent microchannels.

3.8.7.4 Detecting dsDNA through a nanopore while neighboring parts of the membrane are broken or clogged

The ability to fabricate an array of independently addressable nanopores in separate microchannels allows the user to choose which nanopores will be used in an experiment. In a standard macroscopic device containing a single nanopore, it is impossible to continue an experiment should the nanopore become irreversibly clogged or the membrane is broken. With the nanopore arrays presented, however, it is possible to perform multiple experiments on a single device even after a particular nanopore irrecoverably began to exhibit the high noise associated with partial clogging. While less frequently observed, membranes that became damaged upon assembly or upon sharp fluctuations in pressure could also be used in biomolecular experiments by addressing a nanopore on an intact portion of the SiN membrane.

Figure 3-16 shows an ionic current trace through 10.5-nm and 15.5-nm pores in a two-channel device containing microfluidic vias. While a stable baseline was observed for the 15.4-nm pore (Figure 3-16(a).i), an unstable current baseline with high electrical noise properties (unsuitable for biomolecule experiments) was observed for the 10.6-nm pore at

-200 mV (Figure 3-16 (a).ii). The former was thus able to detect the translocation of 10-kbp dsDNA in 3.6 M LiCl, as shown in Figure 3-16(b). As expected for dsDNA translocation in high molarity lithium chloride, events in Figure 3-16(b) are of longer duration than those in KCl.[38] It should also be noted that this experiment was carried out over an hour without observing any significant degradation in nanopore performance.

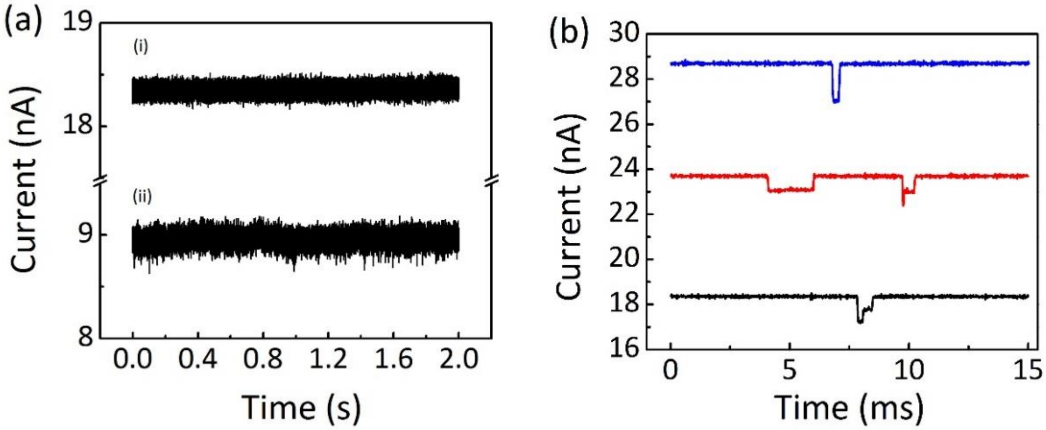

Figure 3-16 **(a)** Ionic current traces through a low-noise 15.5-nm pore **(i)** and an unstable 10.5-nm pore **(ii)** in the same two-channel device containing a microfluidic via layer. **(b)** Individual unfolded, partially folded and fully folded translocation events of 10-kb dsDNA through the low-noise nanopore in 3.6 M LiCl pH10 at three different applied voltages (-200 mV (black), -250 mV (red) and -300mV (blue)). Data were multiplied by -1 for display clarity.

3.9 Additional note

Figure 3-17 illustrates the pressure control scheme, used to introduce the electrolyte (with and without molecule of interest) through the channel of the presented device in this chapter. The device also has a bottom channel (not shown here) which is common between all the top channels of the device. To reduce the chance of breaking the silicon nitride membrane, PDMS-microfluidic channels (top and bottom) are connected to the same regulator and charged at the similar pressure.

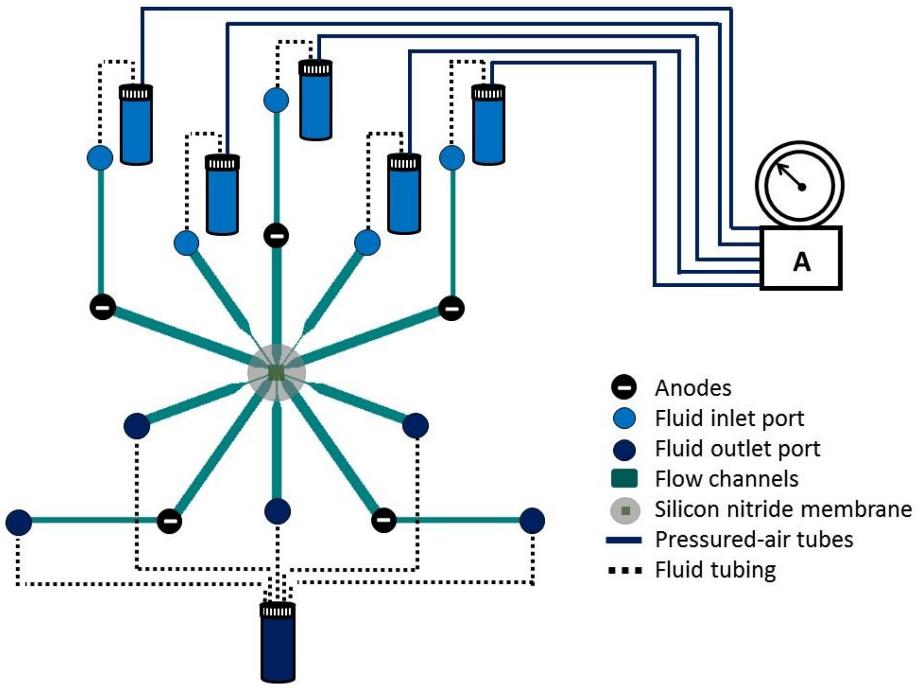

Figure 3-17 Flow control diagram (not to scale). Five-independent microchannels are aligned atop a silicon membrane. The channels are fluidically and electrically independent. The bottom channel is common and place on the other side of the SiN membrane (not shown here). The electrolyte is brought to each channel individually by pressurizing the corresponding vial with a regulator.

3.10 References

[1] C. Dekker, *Nat. Nanotechnol.* **2007**, *2*, 209.

[2] M. Wanunu, *Phys. Life Rev.* **2012**, *9*, 125.

[3] B. N. Miles, A. P. Ivanov, K. A. Wilson, F. Doğan, D. Japrung, J. B. Edel, *Chem. Soc. Rev.* **2013**, *42*, 15.

[4] S. Howorka, Z. Siwy, *Chem. Soc. Rev.* **2009**, *38*, 2360.

[5] O. Otto, U. F. Keyser, in *Eng. Nanopores Bioanal. Appl.* (Eds: J.B. Edel, T. Albrecht), William Andrew Publishing, Oxford, **2013**, pp. 31–58.

[6] J. J. Kasianowicz, J. W. F. Robertson, E. R. Chan, J. E. Reiner, V. M. Stanford, *Annu. Rev. Anal. Chem. Palo Alto Calif* **2008**, *1*, 737.

[7] B. M. Venkatesan, R. Bashir, *Nat. Nanotechnol.* **2011**, *6*, 615.

[8] D. Branton, D. W. Deamer, A. Marziali, H. Bayley, S. A. Benner, T. Butler, M. Di Ventra, S. Garaj, A. Hibbs, X. Huang, S. B. Jovanovich, P. S. Krstic, S. Lindsay, X.

S. Ling, C. H. Mastrangelo, A. Meller, J. S. Oliver, Y. V. Pershin, J. M. Ramsey, R. Riehn, G. V. Soni, V. Tabard-Cossa, M. Wanunu, M. Wiggin, J. A. Schloss, *Nat. Biotechnol.* **2008**, *26*, 1146.

[9] Y. He, M. Tsutsui, M. Taniguchi, T. Kawai, *J. Mater. Chem.* **2012**, *22*, 13423.

[10] J. J. Kasianowicz, E. Brandin, D. Branton, D. W. Deamer, *Proc. Natl. Acad. Sci.* **1996**, *93*, 13770.

[11] J. Clarke, H.-C. Wu, L. Jayasinghe, A. Patel, S. Reid, H. Bayley, *Nat. Nanotechnol.* **2009**, *4*, 265.

[12] W. Li, N. A. W. Bell, S. Hernández-Ainsa, V. V. Thacker, A. M. Thackray, R. Bujdoso, U. F. Keyser, *ACS Nano* **2013**, *7*, 4129.

[13] N. N. Jetha, V. Semenchenko, D. S. Wishart, N. R. Cashman, A. Marziali, *PLoS ONE* **2013**, *8*, e54982.

[14] J. E. Reiner, A. Balijepalli, J. W. F. Robertson, J. Campbell, J. Suehle, J. J. Kasianowicz, *Chem. Rev.* **2012**, *112*, 6431.

[15] V. Tabard-Cossa, M. Wiggin, D. Trivedi, N. N. Jetha, J. R. Dwyer, A. Marziali, *ACS Nano* **2009**, *3*, 3009.

[16] J. J. Kasianowicz, E. Brandin, D. Branton, D. W. Deamer, *Proc. Natl. Acad. Sci.* **1996**, *93*, 13770.

[17] J. Li, D. Stein, C. McMullan, D. Branton, M. J. Aziz, J. A. Golovchenko, *Nature* **2001**, *412*, 166.

[18] E. Beamish, H. Kwok, V. Tabard-Cossa, M. Godin, *Nanotechnology* **2012**, *23*, 405301.

[19] E. M. Nelson, V. Kurz, J. Shim, W. Timp, G. Timp, *Analyst* **2012**, *137*, 3020.

[20] Z. Fekete, G. Huszka, A. Pongrácz, G. Jágerszki, R. E. Gyurcsányi, E. Vrouwe, P. Fürjes, *Procedia Eng.* **2012**, *47*, 13.

[21] N. A. W. Bell, V. V. Thacker, S. Hernández-Ainsa, M. E. Fuentes-Perez, F. Moreno-Herrero, T. Liedl, U. F. Keyser, *Lab. Chip* **2013**, *13*, 1859.

[22] T. Jain, R. J. S. Guerrero, C. A. Aguilar, R. Karnik, *Anal. Chem.* **2013**, *85*, 3871.

[23] A. J. Storm, J. H. Chen, X. S. Ling, H. W. Zandbergen, C. Dekker, *Nat. Mater.* **2003**, *2*, 537.

[24] I. M. Derrington, T. Z. Butler, M. D. Collins, E. Manrao, M. Pavlenok, M. Niederweis, J. H. Gundlach, *Proc. Natl. Acad. Sci. U. S. A.* **2010**, *107*, 16060.

[25] H. Kwok, K. Briggs, V. Tabard-Cossa, *PLoS ONE* **2013**, *9*, DOI 10.1371/journal.pone.0092880.

[26] K. Briggs, H. Kwok, V. Tabard-Cossa, *Small* **2014**, *10*, 2077.

[27] D. Qin, Y. Xia, G. M. Whitesides, *Nat. Protoc.* **2010**, *5*, 491.

[28] S. H. Tan, N.-T. Nguyen, Y. C. Chua, T. G. Kang, *Biomicrofluidics* **2010**, *4*, 32204.

[29] E. Beamish, H. Kwok, V. Tabard-Cossa, M. Godin, *J. Vis. Exp.* **2013**, DOI 10.3791/51081.

[30] S. W. Kowalczyk, A. Y. Grosberg, Y. Rabin, C. Dekker, *Nanotechnology* **2011**, *22*, 315101.

[31] V. Tabard-Cossa, D. Trivedi, M. Wiggin, N. N. Jetha, A. Marziali, *Nanotechnology* **2007**, *18*, 305505.

[32] E. C. Yusko, P. Prangkio, D. Sept, R. C. Rollings, J. Li, M. Mayer, *ACS Nano* **2012**, *6*, 5909.

[33] H. Kwok, K. Briggs, V. Tabard-Cossa, *PLoS ONE* **2014**, *9*, e92880.

[34] R. M. M. Smeets, N. H. Dekker, C. Dekker, *Nanotechnology* **2009**, *20*, 95501.

[35] V. Tabard-Cossa, D. Trivedi, M. Wiggin, N. N. Jetha, A. Marziali, *Nanotechnology* **2007**, *18*, 305505.

[36] V. Tabard-Cossa, in *Eng. Nanopores Bioanal. Appl.* (Eds: J.B. Edel, T. Albrecht), William Andrew Publishing, Oxford, **2013**, pp. 59–93.

[37] V. Dimitrov, U. Mirsaidov, D. Wang, T. Sorsch, W. Mansfield, J. Miner, F. Klemens, R. Cirelli, S. Yemenicioglu, G. Timp, *Nanotechnology* **2010**, *21*, 65502.

[38] S. W. Kowalczyk, D. B. Wells, A. Aksimentiev, C. Dekker, *Nano Lett.* **2012**, *12*, 1038.

Outlined contributions

Communications: Manipulating electrical and fluidic access in integrated nanopore-microfluidic arrays using microvalves

- This work was submitted on **August 5th, 2016** and published online on **December 27th, 2016** in *Small*.
- I, Radin Tahvildari, contributed the large majority of the work including: device design (photomasks), microfabrication, and device assembly, sample preparation, performing the experiments, data acquisition and analysis.
- Eric Beamish, PhD candidate in the Godin lab, provided technical advice. He also assisted in editing all drafts of the manuscript.
- Kyle Briggs, PhD candidate in the Tabard-Cossa lab, developed analysis program based on the CUSUM+ algorithm and assisted in some data analysis.
- Sophie Chagnon-Lessard, a PhD candidate in the Pelling/Godin lab, assisted in some data analysis.
- Shuo Han, former Co-op student in the Godin lab, performed the preliminary experiments on the functionality of the microvalves.
- Dr. Benjamin Watts, former postdoctoral researcher in the Godin lab, trained Shuo Han for microfabrication and advised on preliminary device designs.
- Dr. Ali Najafi Sohi, postdoctoral researcher in the Godin lab, provided technical advice on treatment of the devices.
- The work was done under the supervision of Professor Michel Godin and Professor Vincent Tabard-Cossa.
- The format of the manuscript has been modified for formatting purposes.
- The presented supplementary material, Section 4.8, was submitted with this work.
- Section 4.9, as an additional note, was originally not included in the submitted draft of the manuscript.

Chapter 4 | Manipulating electrical and fluidic access in integrated nanopore-microfluidic arrays using microvalves

Reproduced by permission of Wiley Online Library from:

Tahvildari, R., Beamish, E., Briggs, K., Chagnon-Lessard, S., Najafi Sohi, A., Han, S., Watts, B., Tabard-Cossa, V., and Godin, M. Manipulating electrical and fluidic access in integrated nanopore-microfluidic arrays using microvalves. *Small*, (2016). DOI: 10.1002/smll.201602601

4.1 Motivation and Objectives

In the previous chapter, we demonstrated *in situ* fabrication of a 5×1 array of solid-state nanopores within microfluidic networks using controlled breakdown (CBD). The fluidic and electrical access of each microfluidic channel required to be controlled independently. Therefore, large number of fluidic and electronic connections complicated. Microvalve technology has become an important component for automation of microfluidic large-scale integration (mLSI). This chapter highlights our effort to deploy on-chip pneumatic microvalves to manipulate fluidic and electrical access within the integrated nanopore-microfluidic device.

4.2 Abstract

Controlled breakdown (CBD) facilitates the fabrication of arrays of individually addressable nanopores within microfluidic devices. Herein we show that the addition of PDMS-based on-chip microvalves makes it possible to fluidically and electrically isolate connected flow channels and their respective nanopore sensors. Pressure-actuated valves provide a high electrical resistance seal (~100 GΩ) through each flow channel of the device. A single pair of electrodes is sufficient to independently address multiple nanopores, allowing for the on-demand fabrication, size tuning and use in molecular

sensing experiments. We demonstrate on-chip sequestration of multiple biomolecular samples in the various flow channels and their subsequent analysis using independent nanopore sensors fabricated on a single solid-state membrane. Finally, we show that partially-actuated microvalves can be used to segment a fluidic sample while still allowing ionic current measurements during a sensing experiment.

4.3 Introduction

Nanopore sensors most commonly rely on an ionic current measurement to detect and characterize the conformation and structure of biological molecules such as DNA, protein or molecular complexes.[1] Intensive research efforts over the past two decades have explored their use in a variety of applications including DNA sequencing,[2–4] single molecule force and mass spectroscopy,[5–8] protein-aptamer interactions[9] and drug discovery.[10] Solid-state nanopores have drawn attention for their tunable size, environmental tolerance and propensity simplicity for integration in lab-on-a-chip technologies.[11–13] A solid-state nanopore device typically consists of a single nanoscale channel in a thin insulating membrane that separates two electrolyte solutions. Ionic current is induced across the pore by applying an electric potential difference across the membrane. The passage of molecules through the nanopore causes a disruption in the ionic conductance, which can be used to determine the structure and identity of the translocated molecule.[14] Typically, a nanopore experiment requires the translocation of many individual biomolecules to reliably extract information with statistical significance. Therefore, arrays of nanopores have compelling advantages in terms of rapid and high-throughput data acquisition. In addition, nanopore sensors are typically situated between macroscale fluidic reservoirs. This configuration limits the ability of a nanopore device to perform on-demand sample preparation, manipulation and processing.[15]

Sample manipulations within microfluidic architectures are recognized to enhance experimental outcomes through automation and miniaturization of analytical sensors.[16–18] Many researchers are adapting microfluidic technologies to perform a variety of diagnostic tests with built-in and low-cost analysis capabilities due to their spatial and temporal control.[16,17] They can confine, pre-process, purify, mix, sort, and fractionate a small volume (micro to nanoliters) of fluidic sample in their microscale architectures.[18–20]

Some techniques and strategies have been reported to integrate solid-state nanopores in microfluidics.[21–23] Nanopores used in these studies were milled in a thin insulating membrane using a high energy electron[24] or ion beam,[25] or derived from quartz capillaries with a laser puller[26] prior to integration. Beam-based techniques of nanopore fabrication are complex, expensive and ill-suited for integration within microfluidic networks since nanopores must be fabricated prior to integration, i.e. milled *ex-situ*. For instance, fragility of large-area membranes, handling risks, wetting issues and inaccurate alignment of multiple channels on pre-fabricated nanopores are among the commonly reported challenges.[21,23] On the other hand, while glass nanopores fabricated by laser pulling reduce cost and offer good performance, reproducibly achieving sub-20 nm diameter pores in this manner is generally difficult, and scaling to large arrays of glass pipettes can be challenging.[27]

We recently reported a microfluidic device[28] in which an array of low-noise solid-state nanopores was fabricated *in situ* by controlled breakdown (CBD).[29,30] Due to its simplicity, the CBD method can easily accommodate nanopore fabrication in solid-state membranes enclosed in a range of fluidic configurations. Importantly, we found that controlling the electrical field symmetry during the nanopore fabrication process and biomolecular sensing improved the sensor's detection efficiency. We demonstrated that a symmetric electric field can be ensured by including microfluidic *vias* on the membrane at the site of nanopore formation and/or by using equally biased electrodes within the same microchannel, one located upstream of the membrane and another downstream. However, the device previously presented required that each microfluidic channel be controlled independently with its own fluidic and electrical access. Indeed, the large number of fluidic and electronic connections (two fluidic tubes and two electrodes per channel) crowded the device and complicated the surrounding setup. In an effort to mitigate this issue, this work highlights the use of on-chip pneumatic microvalves, which also provides new opportunities for fluidic manipulation before and during sensing.[31,32] Typically, pneumatic valves are formed by stacking two microfluidic channels formed in separate layers using an elastomeric material. When a high pressure is applied to one channel, the other one will be compressed, restricting flow. This technology has been developed as a practical way to obtain microfluidic large-scale integration[33] in the design and fabrication of biosensors.[34–36]

Herein, we demonstrate a microfluidic device that includes multiple microvalves and an array of five independently addressable solid-state nanopores on a single membrane. This feature allows for precise manipulation of fluidic and electrical access to various regions of the embedded silicon nitride (SiN) membrane from a common inlet with a single pair of electrodes. Importantly, we show that the pressurized (actuated) microvalves provide electrical resistances that are high enough (>50 GΩ) to isolate desired regions of the SiN membrane for the serial fabrication and independent use of nanopore sensors in each flow channel. We introduce a looped flow channel design to ensure a symmetric electrical field profile at the pore location on the insulating membrane. In addition, we discuss chemical compatibility when nanopores are integrated within polydimethylsiloxane (PDMS) microchannels and report improved performance when the PDMS components constituting the microchannel layers of the device are treated with organic solvents prior to embedding the solid-state chip. This treatment removes uncross-linked contaminants from the bulk polymer.[37] Finally, we present the ability to store samples on chip prior to nanopore analysis using the microvalves. One of the more intriguing features of this design is the ability to use the microvalves in a partially pressurized configuration to restrict fluid flow while allowing for electrical access to the nanopores for biomolecular sensing.

4.4 Results and Discussion

4.4.1 Design and Validation

The microfluidic device integrating a solid-state membrane supported by a silicon chip is pictured in Figure 4-1. Five connected flow channels equipped with on-chip microvalves allow for the fabrication of individually addressable nanopores by CBD[29,30] and subsequent enlargement with high electric fields.[38,39] Figure 4-1a is a top view of the device showing the microvalves (red) and flow channels (blue) made from multilayered PDMS pieces.[24] Only a small, ~1000 μm^2 region of the membrane inside each flow channel is exposed to electrolyte through a microfluidic *via* (Figure 4-1(b)). As previously reported[28], these microvias limit the exposed area of the membrane to the aqueous solutions, thus localizing the formation of the nanopores by confining the electric field. This also results in a significant reduction of high frequency noise in the ionic current signal through reduction of chip capacitance.[41] The fluid is flushed in and out of the device through a common inlet and outlet. The etched side of the silicon chip sits atop a wide microfluidic channel containing an electrode that is common to all nanopores on the device (shown as purple in Figure 4-1). On the other side of the membrane, five flow channels are fluidically connected, but the inclusion of five pairs of microvalves adjacent to the membrane allows for separate fluidic and electrical control of each exposed membrane region or nanopore. A routing microvalve (green in Figure 4-1(a)) is also included next to the common inlet and pressurized during fluid introduction to ensure that flow channels are filled uniformly. Valves pressurized to 30 psi act as electrical resistors, providing more than 50 GΩ of electrical resistance in each flow channel that can effectively isolate different regions of the SiN membrane during serial nanopore fabrication and biomolecular sensing. Measurements validating the microvalve functionality are described in Section 4.8.7.

During the fabrication of each nanopore, electrical access is restricted in the other four flow channels by pressurizing the corresponding microvalve pairs (Figure 4-1(c)). The pair of the microvalves addressing the targeted flow channel remains unpressurized (Figure 4-1(d)). A cross sectional view of a typical device containing a pair of microvalves, a flow channel and a microvia atop the membrane is illustrated in Figure 4-6.

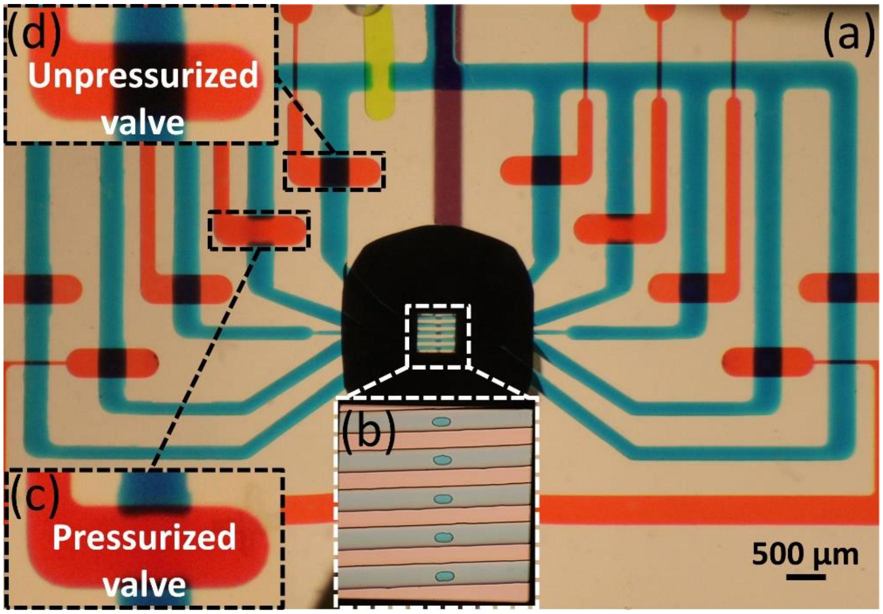

Figure 4-1 **(a)** Micrograph of the integrated SiN chip in a microfluidic network Containing the flow channels (blue), microvalves (red), routing valve (green) and a common bottom channel (purple). **(b)** Five flow channels, each containing a 50×20 μm^2 microvia, cross over a 500×500 μm^2 SiN membrane **(c) Pressurized (actuated) mode:** During nanopore fabrication or biomolecular sensing in the desired flow channel, all other valve pairs are pressurized to 30 psi to obtain high electrical resistance seal. **(d) Unpressurized (unactuated) mode:** Valve pairs corresponding to the target flow channel are charged to atmospheric pressure to allow for electrical and fluidic access to the nanopore. See Section 4.6.2 and Figure 4-4 for more detail.

While elastomeric microvalves are extensively used in microfluidic devices, we found that controlling the flow channel wall hydrophobicity was particularly important to ensure a high electrical resistance seal. High hydrophobicity prevents electrolyte solution (and thus parasitic ionic current) from remaining in the channel cross section when a flow channel is compressed by its valves. However, wetting the insulating membrane prior to nanopore fabrication is important and this can be challenging when the hydrophilicity of the device is reduced. In most cases, it was adequate to flush the hydrophobic flow channels with ethanol prior to the introduction of an aqueous solution. This flushing procedure increases the wettability of the flow channels and the SiN membrane due to the low surface tension of ethanol. Although plasma-treating[42] the assembled device prior to nanopore fabrication could still be a useful method to facilitate wetting of the flow channels and the membrane surface, we found that all of the valves in the device needed to be pressurized during plasma treatment in order to maintain hydrophobicity of the flow channels at the valves location. This process is described in Section 4.8.5.

The high electrical resistance seal provided by the on-chip microvalves enables the fabrication of individual nanopores by CBD, while the other areas of the same SiN membrane that are exposed to the electrolyte in other flow channels are electrically isolated and remain intact. We also confirmed that existing nanopores remain unaffected when isolated by the microvalves even when high electric fields are applied in adjacent flow channels. Each solid-state nanopore is formed by applying 14 V to 18 V across the 20-nm thick SiN membrane, thus producing a high electric field (0.7-0.9 V/nm). A typical nanopore fabrication curve is shown in Figure 4-9. Nanopore fabrication typically takes a few minutes[30] and the resulting nanopores are assessed and electrically validated immediately prior to performing molecular sensing experiments.

Figure 4-2(a) shows current to voltage (I-V) measurements of five nanopores fabricated sequentially in a single device. The diameter d of each nanopore was extracted from its conductance, G, which was measured by recording the ionic current over a range of applied potentials.[43] Equation 4-1 describes the relationship between nanopore diameter and conductance, where σ is the conductivity of the electrolyte and L_{eff} is the effective thickness of the nanopore assuming a cylindrical geometry.

$$\mathrm{G} = \sigma \left(\frac{4L_{\mathrm{eff}}}{\pi d^2} + \frac{1}{d} \right)^{-1} \tag{4.1}$$

Generally, the effective thickness of the nanopore is smaller than the nominal thickness of the SiN membrane due to deviations from the assumed cylindrical shape of the nanopore (60% to 85% of its nominal thickness).[44] Interestingly, nanopores formed at different locations within a single membrane can show different effective thicknesses, possibly due to varying SiN thickness across the membrane window or most likely, as a result of slight deviations of the actual nanopore shape from the assumed perfect cylindrical geometry. Note that we have found that this effect is more pronounced on membranes with thicknesses that are ≥20-nm than on <10-nm membranes.

Double-stranded DNA (dsDNA) translocation experiments were conducted to assess the suitability of these integrated nanopores for biomolecular sensing applications.

Figure 4-2(b) shows typical ionic current traces through five nanopores in the same device, each having different diameters.

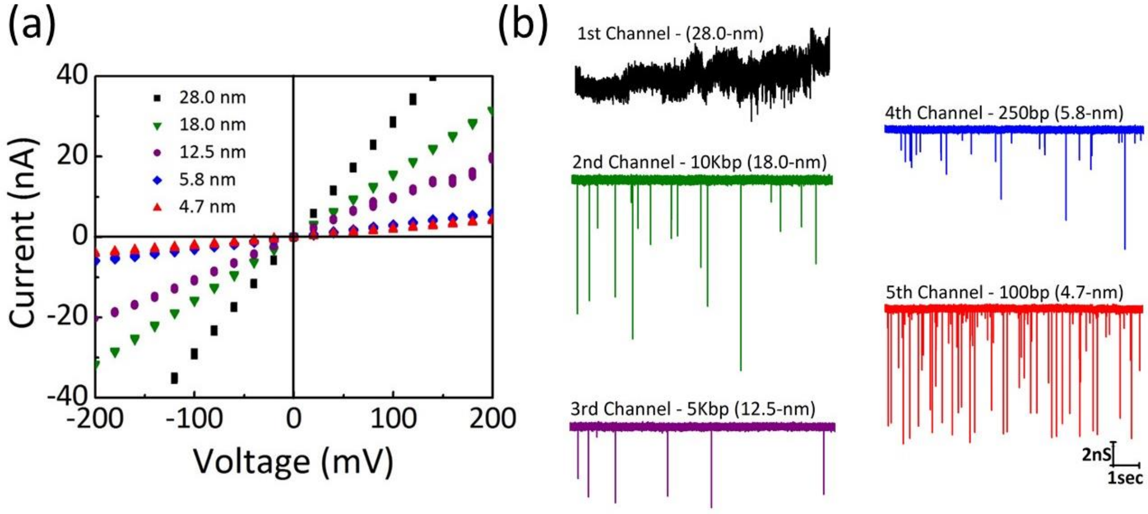

Figure 4-2 **(a)** Current versus voltage (I-V) curves used to infer each nanopore diameter. **(b)** Traces of the ionic current through five independently fabricated nanopores in a single device. The first nanopore (black) exhibited high noise and was unsuitable for biomolecular sensing experiments. The remaining four showed the translocation of various lengths of dsDNA under an applied potential difference of 200 mV. All measurements were done in 2 M KCl buffered at pH 8.0 and ionic current traces were sampled at 250 kHz, low-pass filtered at 100 kHz using a 4-pole Bessel filter and multiplied by -1 for visualization.

Here we present an example of a device in which the nanopore in the first flow channel exhibited high 1/*f* noise and was unsuitable for biomolecular sensing, while the remaining nanopores formed in the same membrane but in the other flow channels were fully functional and exhibited a clean, stable, conductance prior to the addition of biomolecular samples. This highlights one of the advantages of working with arrays of nanopores which are individually addressable using on-chip microvalves, namely increasing the experimental yield of functional pores by enabling the analysis of either the same injected sample with multiple nanopores, or multiple samples independently within a single device.

In this example, the biomolecular samples consisted of 100, 250, 5k and 10k base pair (bp) dsDNA fragments were independently introduce to the flow channels and the resulting translocation characteristics were consistent with results obtained using standard nanopore setups (Section 4.8.13).[43]

In PDMS-based microfluidic devices, incomplete curing of the two-part elastomer can result in unpolymerized monomers leaching out into the fluidic microchannels. In some instances, we have observed a degradation in the performance of a device over time (days) which we have linked to this leaching process. This can manifest itself as an increase in 1/*f* noise, frequent device clogging due to a gradual change in nanopore surface properties or a reduction in the nanopore capture rate. However, these issues were mitigated by immersing the PDMS components in a series of organic solvents prior to assembly,[37] which effectively removed unreacted low-molecular weight monomers from the PDMS bulk phase (see Section 4.6.2). This procedure ensures that the devices and their integrated nanopores perform reliably even when stored for up to 10 days prior to being used in molecular sensing experiments.

4.4.2 Modes of operation

The device configuration allowed for experiments to be conducted in various modes of operation depending on whether the sample was introduced in the common microchannel or in one of the independent flow channels located on the opposite side of the membrane. Samples introduced to the common channel could be analyzed by several different nanopores sequentially. This might be useful if the performance of a nanopore degrades during an experiment, as other nanopores can be used to continue acquiring translocation data to obtain a statistically significant number of single molecule events. This is particularly advantageous when a precious, low-volume sample is undergoing analysis. Experiments can also be conducted using the independent channels under constant flow conditions with the ability to exchange solutions and dilute samples at any time to be analyzed either by the same nanopore or by others in the array.

An interesting extension is the ability to use on-chip valves to store different samples in the vicinity of a nanopore until they are ready to be analyzed. In Figure 4-2(b), sensing was performed as each flow channel was sequentially filled with the desired sample type while other flow channels were fluidically isolated by their corresponding valves, as described in the Methods section. After >1000 translocation events were recorded, the sample was then trapped in the flow channel by pressurizing the appropriate microvalve pair while the device was flushed with fresh solution and a new sample was loaded to a neighbouring flow channel. After all samples were loaded, a specific sample could then be analysed by opening the appropriate pair of valves. While we successfully conducted experiments under these conditions, great care was required in this operational mode to equalize pressures to minimize unintended flow through the channel. Any pressure differential across a channel, even one induced by a difference in height of the vials which accommodate the inlet and outlet tubing, would rapidly remove a plug of solution containing sample from the vicinity of the nanopore. This small but unintended flow could result in a drastic decrease in sample concentration and nanopore capture rate (Section 4.8.8 and Figure 4-11).

We can address this issue by using the microvalves in a partially-pressurized configuration. As shown in Figure 4-13, it is possible to reduce the cross sectional area without complete collapse of the flow channel using a moderate valve pressure. This constriction increases flow resistance, minimizing the removal of sample from the vicinity of the nanopore while still allowing electrical access for biomolecular sensing. In the case of a small sample volume (nanoliters) trapped in a flow channel between valves while the remainder of the channel is filled with pure belectrolyte solution, the reduced cross sectional area of the constricted channel also minimizes diffusion of biomolecules away from the sensing region of the nanopore. In order to facilitate the partial collapse of flow channels, a device with modified flow channel dimensions (wider flow channels under narrower valves) was used (Figure 4-5). A schematic cross section of this operational mode is shown in Figure 4-3(a), where 5kb dsDNA was first introduced into a flow channel containing a nanopore. Figure 4-3(b).i shows an ionic current trace containing biomolecular translocation events while the valves remained unpressurized. As pressure is applied to the microvalves, the flow channel is partially collapsed on either side of the nanopore, trapping the sample in the vicinity of the pore. As shown in Figure 4-3(b).ii, applying moderate pressure to the microvalves initiates a reduction in the ionic current measured through the system due to the increased electrical resistance imparted by the partially collapsed flow channel. However, the desired electric field strength at the nanopore was then re-established by increasing the applied electric potential difference (Figure 4-3(b).iii) until the ionic current through the nanopore was equal to its initial value when the valves were unpressurized.

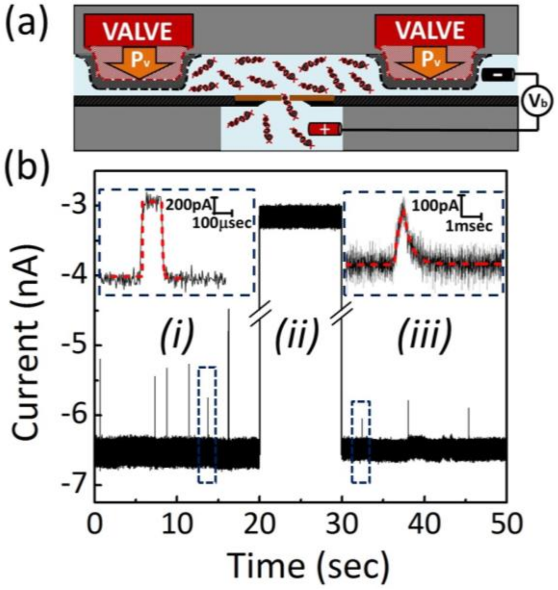

Figure 4-3 **(a)** Schematic cross section of a device showing a flow channel (light blue) and microvalves (dark red). By pressurizing the microvalves to a moderate pressure P_v, the active PDMS membrane is deflected downward to reduce fluid flow and sample loss through the flow channel (dashed lines). (**b)** Ionic current traces showing the translocation of 5 kbp dsDNA in 2 M KCl pH 8.5 through a 7.8-nm pore in three different conditions: **(i)** an applied bias $V_b = 200$ mV and pressure $P_v = 0$ psi, **(ii)** $V_b = 200$ mV and $P_v = 20\pm1$ psi and **(iii)** $V_b = 500$ mV and $P_v = 20\pm1$ psi. Traces of individual linear (unfolded) translocation events before and after the valves are pressurized are shown in the insets. Dashed red lines show fits to the events using Equation 4.11 to extract rise times and blockage levels of translocation events. Ionic current measurements were acquired at 250 kHz and low-pass filtered at 100 kHz using a 4-pole Bessel filter.

In order to show that nanopore sensing is possible while the microvalves are partially actuated and test the limits of channel constriction while maintaining molecular sensing ability, a proof-of-concept experiment was performed in which dsDNA was introduced into an independent flow channel while the corresponding microvalve pair was pressurized. To determine the limits of channel compression while maintaining the ability to sense biomolecular translocations, the experiment presented in Figure 4-3 reflects the maximum valve pressure that could be applied before completely preventing electrical measurements of the nanopore sensor (20±1 psi for this device). In this configuration, the flow channel is almost completely collapsed, with a cross sectional area reduced from 12500 μm^2 to <50 μm^2 at the location of the microvalves. Cross sectional profile of the flow channel during microvalves actuation is presented in Section 4.8.9. While this constriction had negligible effect on the equivalent capacitance of the device in this regime (20±5 pF), the total electrical resistance of the flow channel was increased by almost three orders of magnitude, from $\mathrm{R_{ch}} = 0.075\pm0.005\ \mathrm{M\Omega}$ to $\mathrm{R'_{ch}} = 45\pm5\ \mathrm{M\Omega}$, and the ionic current was reduced accordingly. Even after increasing the applied voltage from 200mV to 500mV in order to re-establish the ionic current level through the channel, this added resistance results in a smaller ionic current blockade upon translocation, as shown in Figure 4-3(b), as the relative change in the current blockage in the pressurized and partially pressurized valve configurations is given by

$$\frac{\Delta \mathrm{I}'}{\Delta \mathrm{I}} = \frac{\mathrm{R_{DNA}}}{\mathrm{R'_{ch}}+\mathrm{R_{DNA}}} \tag{4.2}$$

Where $\Delta\mathrm{I}'$and $\Delta\mathrm{I}$ are the ionic current changes caused by DNA translocation while the valves are respectively partially pressurized and open, $\mathrm{R'_{ch}}$ is the resistance of the channels when the valves are partially pressurized, and $\mathrm{R_{DNA}}$ is the nanopore resistance during the passage of a DNA molecule. In this example, the ratio of blockage levels for unfolded dsDNA in the pressurized and unpressurized valve regimes is 0.41, in agreement with what is expected for the electrical resistance values measured (Section 4.8.10).

The increase in electrical resistance of the flow channels when the valves are partially pressurized can also affect the shape of the ionic current trace corresponding to the translocation of dsDNA molecules by significantly slowing the response of the ionic current to step changes in the pore resistance. The current response is dominated by the slower of either the applied low-pass filter, in our case a 100 kHz 4-pole Bessel filter imposed by the current amplifier, or the RC response of the device.[45] In the present case, the low-pass filter dominates when the valve is unpressurized, and the RC response dominates when the valve is partially pressurized.

When compressed flow channels contribute significant electrical resistance, the relevant rise times for DNA entry to, α_1^{-1}, and exit from, α_2^{-1}, the pore are then given respectively by Equations 4-3 and 4-4, where R_p and C are respectively the resistance of the nanopore and the capacitance of the membrane/chip exposed to liquid through the microvia.[45]

$$\alpha_1^{-1} = \frac{CR'_{ch}R_{DNA}}{R'_{ch}+R_{DNA}} \quad (4.3)$$

$$\alpha_2^{-1} = \frac{CR'_{ch}R_p}{R'_{ch}+R_p} \quad (4.4)$$

Fits to unfolded translocation events for the equivalent electrical circuit presented in Section 4.8.10, yield experimental rise times of $\alpha_1^{-1} = 277 \pm 79$ µs and $\alpha_2^{-1} = 377 \pm 24$ µs, which is in good agreement with what would be expected from Equations 4.3 and 4.4. While this distorting effect is present in configurations of extreme flow channel compression, such as that shown in Figure 4-3, we note that it is possible to apply a lower pressure to the microvalves (<10 psi) such that flow channel constriction does not contribute significant electrical resistance while still restricting flow (Figure 4-13). However, the minimal signal attenuation inherent in such configurations come at the expense of a decreased ability to confine sample in the vicinity of a nanopore for sensing.

4.5 Conclusions

In this article, we have utilized PDMS-based pneumatic microvalves to manipulate electrical and fluidic access to solid-state nanopore arrays fabricated by controlled breakdown within microfluidic architectures. While unpolymerized monomers from the PDMS components of a device can interfere nanopore sensing, their extraction using a series of organic solvents improves device performance. This is providing a biocompatible environment for rapidly generating prototype lab-on-a-chip devices. By fully collapsing flow channels using pressurized microvalves, it is possible to obtain a high electrical resistance seal (>50 GΩ) for the serial on-demand fabrication of nanopores in different regions of a single embedded silicon nitride membrane.

This integrated sensing platform allows for biomolecular analysis while offering microfluidic sample processing capabilities, all while efficiently minimizing the required number of electrodes and fluidic tubing to increase scalability. To improve nanopore fabrication and molecular sensing, a symmetric electric field is provided within a looped flow channel and using a single electrode pair. In addition, microvalves allow for the introduction and sequestration of multiple samples to be analyzed by different nanopores within a single device. Furthermore, partially pressurizing microvalves can effectively segment a biomolecular sample in the vicinity of a nanopore while allowing electrical access for sensing.

While the flow channel cross section can be reduced to sub-50 μm^2 to minimize parasitic flow and sample loss, this can impart an electrical resistance comparable to the integrated nanopore, limiting the bandwidth of the sensor. However, varying microvalve pressure can precisely control cross section collapse to provide <1 MΩ of electrical resistance while still segregating fluidic samples. Such sample control can ultimately be used to effectively purify, sort and mix biomolecular samples for on-chip analysis using large-scale arrays of nanopores.

4.6 Experimental Section

4.6.1 Microfabrication

Low-stress 500×500 μm^2, 20-nm-thick silicon nitride membranes supported on 100-µm-thick, 3 mm frame size silicon substrate (SiMPore Inc. SN100-A20Q05) are embedded between PDMS pieces (Sylgard 184 kit, Dow Corning). Each PDMS piece is replicated from a master mould fabricated by multilayered soft lithography[31] with SU-8 2050 (MicroChem) and AZ 50X (Electronic Materials) photoresists. Full microfabrication protocols and methods are provided in Sections 4.8.2 and 4.8.3.

4.6.2 Device specifications and assembly

Figure 4-1 is a top view of an assembled device in which aqueous food coloring (Club house) was used to feature flow channels and valves. A three-layer PDMS piece (valves, flow channels and the microvia layer) was aligned and bonded to the membrane side of the silicon chip using an oxygen plasma system. The etched side was placed on a hand-punched hole in the middle of a single channel (purple) to allow electrical and fluidic access to the etched side of the chip. This common bottom channel is 400 µm wide and 100 µm high.

The flow channel layer (blue) consisted of five connected microfluidic channels, which narrowed over the membrane. The valve layer (red) located above the flow channels contained five pairs of independent channels, which intersected perpendicularly with flow channels of similar width. In order to avoid undesired collapsing of a fluidic channel, valve channels narrowed over such intersections (passive crossovers).[32] A routing valve (green) is discharged to atmosphere during nanopore fabrication and biomolecular sensing, resulting in a symmetric electric field across the membrane in each flow channel.

A thin (5 to 7 μm) deflectable PDMS membrane separates the flow channel layer from the valves. The thickness of this membrane is dictated by the thickness of the PDMS elastomer covering the flow channels. Therefore, uncured PDMS was spun onto the flow channels mould whereas the elastomer was directly cast on the valves mould. Consequently, the valve layer is several millimeters thick to securely accommodate the tubing and electrodes. Detailed device specifications and assembly are presented respectively in Sections 4.8.1 and 4.8.4. Figure 4-16 is an overview of a typical integrated nanopore-microfluidic device with five connected flow channels while all the microfluidic channels are filled with food coloring dyes.

4.6.3 Solvent extraction of PDMS pieces

Significant improvement in the yield of nanopores functional for biomolecular sensing was observed when residual uncross-linked PDMS monomers were extracted from the PDMS device components. For this purpose, the PDMS pieces were immersed sequentially in three different organic solvents[37] prior to mounting the silicon chip. The PDMS pieces were first soaked in 20% (v/v) hexane in ethanol for an hour, followed by ethyl acetate (1 day), then acetone (2 days). The components were then dried at 70 °C for 2 days in an oven. This extraction resulted in a ~0.4-1.0% reduction in overall weight of the PDMS pieces.

4.6.4 Electrical and fluidic setup

The location of the electrodes was chosen to limit the electrical resistance of the flow channels approaching each nanopore to ~100 kΩ in 1 M KCl (~0.1% of the total electrical resistance of a 10-nm nanopore). Fluid was introduced to the flow channels and microvalves *via* PEEK tubes (IDEX health & Science), which were connected to vials pressurized using high-precision pressure regulators. To avoid introducing air bubbles in the flow channels, the valves were filled and pressurized with deionized water. Prior to nanopore fabrication, a resistance seal of ~100 GΩ was measured between the different flow channels while the valves were pressurized up to 30 psi.

4.6.5 Nanopore fabrication

Individual nanopores were fabricated within a few minutes by CBD in 1 M KCl buffered to pH 8.3 ($\sigma = 11.0 \pm 0.1$ S m^{-1}). As previously described,[28] this was achieved by applying high electric fields across the SiN membrane (using a potential difference of 14 V to 18 V) through each of the integrated flow channels using a custom-built current amplifier circuit. A typical nanopore fabrication by CBD is shown in Figure 4-9. Nanopores were conditioned and enlarged as required by the cyclic application of moderate electric field pulses.[22, 23] Afterward, ionic currents were measured in the same electrolyte solutions that were used for biomolecular sensing experiments. Ionic current power spectral density plots of the presented nanopores are provided in Figure 4-15. This protocol was used to produce 15 microfluidic devices, each containing at least 3/5 stable low-noise nanopores. Pores showing excess 1/*f* noise (defined as >10 pA^2/Hz at 1 Hz under an applied potential of 200 mV), were not used in sensing experiments.

4.6.6 Sample preparation and sensing methods

Double-stranded DNA fragments (NoLimits, Thermo Scientific) of 100, 250, 5k and 10k base pair (bp) in length were diluted in 2 M KCl ($\sigma = 20.0 \pm 0.1$ S m^{-1}) buffered with 10 mM HEPES to pH 8.0 to a final concentration of 750 ng/µL. To avoid mixing of different DNA lengths between experiments or between flow channels within a device, the common inlet channel was flushed with aqueous salt solution prior to the introduction of each new sample. For this purpose, all valves were pressurized while the routing valve was unpressurized. The target dsDNA sample was sent through the next flow channel and sensed with the appropriate nanopore. All sensing experiments were performed until approximately 1,000 translocation events were acquired for each nanopore.

4.6.7 Data acquisition and analysis

All experiments were performed inside a Faraday cage to minimize environmental electrical noise pickup. Custom-written LabView programs interfaced with a USB-6351 DAQ card (National Instruments) were used for nanopore fabrication and sensing. Nanopore fabrication was monitored at 10 Hz, while data acquisition for biomolecular sensing experiments was performed at 250 kHz and low-pass filtered at 100 kHz with a 4-pole Bessel filter using an Axopatch 200B (Molecular Devices). Translocation data was analyzed using a custom implementation of the CUSUM+ algorithm[46,47], as well as the adept2State module of MOSAIC v1.3.[45] Figures were plotted in Originlab. Nanopore and microchannel capacitance measurements were performed using a handheld capacitance meter (Keysight U1701B) connected to electrodes embedded in the appropriate microchannels under the indicated operational modes.

4.7 Acknowledgement

This work was supported by funding from the Natural Sciences and Engineering Research Council of Canada (NSERC), the Ontario Ministry of Research and Innovation, and the Canada Foundation for Innovation (CFI). The authors would also like to acknowledge Sebastian Hadjiantoniou for his help in analyzing the fluorescence images (Section 4.8.9).

4.8 Supplementary Information

Supporting information includes device specifications, microfabrication protocols, device assembly, nanopore fabrication and control experiments, and analysis of partially-closed valve data.

4.8.1 Device specifications

4.8.1.1 Five linked flow channels

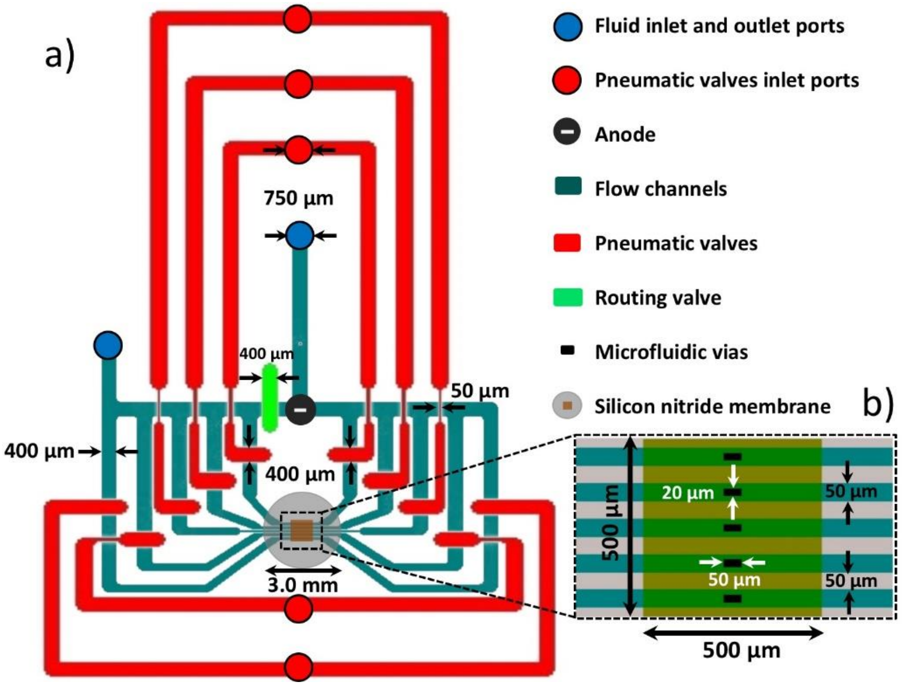

Figure 4-4 Schematic top view of the PDMS layers on one side of the integrated nanopore device showing a) the configuration and dimensions of the fluidic microchannel and microvalve layers, and b) an enlarged view of the fluidic channels crossing and linked to the SiN membrane by microfluidic vias. For clarity, the common bottom channel of the device is not shown in the schematic.

4.8.1.2 Two linked flow channels

This device was used to investigate the translocation properties of biomolecules in the partially-pressurize valve regime. In order to partially collapse fluidic channels, narrow valves crossed widened portions of two linked flow channels. The PDMS layer of the flow channels was mixed at 5:1 (base:curing agent) for increased stiffness, enabling controlled channel collapse over a wider range of applied pressure. This configuration contains a microvia layer on the SiN membrane and accommodates two electrodes in order to produce a symmetric electrical field across the membrane.

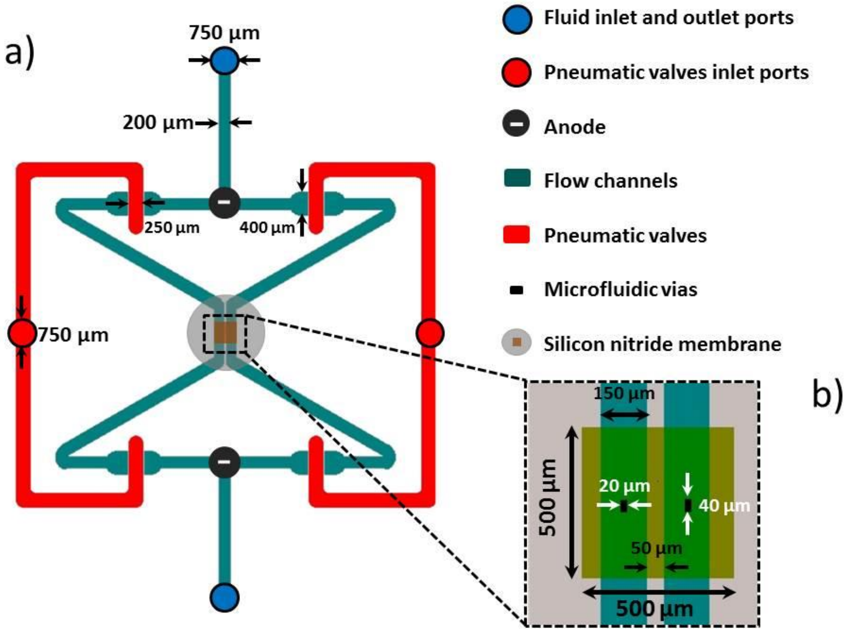

Figure 4-5 Schematic top view of the device with two linked fluidic channels used for operating in the partially-pressurized microvalve regime. a) The dimensions of each layer and b) an enlarged view of the channels crossing over the membrane are shown. For clarity, the common bottom channel of the device is not shown in the schematic.

4.8.2 Microfabrication

Photomasks used to fabricate master moulds by soft lithography[48] were first designed in a CAD program (CleWin, PhoeniX software). Microfluidic devices made of polydimethylsiloxane (PDMS) layers were then replicated from the master moulds. The various fabrication parameters (spin speeds, baking times and temperatures, UV exposures and developing times) are used for the different final thicknesses (heights) of the features for each layer (Tables 4-1 and 4-2).

Table 4-1 SU8-2050 (Microchem Inc.) master mould fabrication parameters

Valve layer (100µm height)				
Spin	**Soft Bake**	**UV exposure***	**Post Bake**	**Developing**
5 s @ 500 rpm	3 min @ 65 ^{0}C 9 min @ 95 ^{0}C	15 s	4 min @ 65 ^{0}C 9 min @ 95 ^{0}C	8 min
30 s @ 1700 rpm				

Common (bottom) channel layer (100µm height)				
Spin	**Soft Bake**	**UV exposure***	**Post Bake**	**Developing**
5s @ 500 rpm	3 min @ 65 ^{0}C 9 min @ 95 ^{0}C	15 s	4 min @ 65 ^{0}C 9 min @ 95 ^{0}C	8 min
30s @ 1700 rpm				

Microvia layer (50µm height)				
Spin	**Soft Bake**	**UV exposure***	**Post Bake**	**Developing**
5 s @ 500 rpm	1 min @ 65 ^{0}C 6 min @ 95 ^{0}C	9 s	1 min @ 65 ^{0}C 6 min @ 95 ^{0}C	5 min
30 s @ 3000 rpm				

***UV energy in our system is measured to be 17.6 mJ/cm^2 (OAI 306, UV power meter)**

In order to achieve sufficient electrical resistance to isolate channels for nanopore fabrication using high electric fields, rounded flow channels were used to enable full collapse using microvalves. To this end, the moulds used for flow channels were patterned with 45-µm thick features using an AZ-50XT layer which was reflowed to result in 50-µm thick rounded microchannels.[49]

Table 4-2 AZ-50XT (AZ Electronic Materials) master mould fabrication parameters

Flow channel layer (50µm height)					
Spin	**Soft Bake**	**Rehydration**	**UV exposure***	**Developing**	**Reflow**
5 s @ 500 rpm	2 min @ 85 ^{0}C 12 min @115 ^{0}C	At least 3 hr	70 s	20 min	5 min @ 75 ^{0}C 5 min @ 105 ^{0}C 5 min @ 135 ^{0}C
30 s @ 1200 rpm					

***UV energy in our system is measured to be 17.6 mJ/cm^2 (OAI 306, UV power meter)**

After fabrication of each master mould, the related features thicknesses were measured by a profilometer (Dektak 3-30, Veeco Sloan).

4.8.3 Multi-layer PDMS

Following the fabrication, all the moulds were silanized with trichlorosilane (tridecafluoro-1, 1, 2, 2-tetrahydrooctyl, Sigma Aldrich) to facilitate PDMS removal. PDMS was mixed at 10:1 (w:w) base:curing agent for the valve and bottom channel layers, then poured directly over their respective master moulds. The mixture was degassed in a vacuum chamber for 30 minutes and baked at 80°C for 2 hours.

PDMS mixtures for flow channels (mixed at 20:1) and microvia layers (mixed at 10:1) were degassed, spun on their master moulds and baked at 80 °C for 20 minutes. Table 4-3 contains the spin parameters used.

Table 4-3 Spin settings for PDMS layers

Flow channel PDMS layer (55-µm thick)	**Microvias PDMS layer (36-µm thick)**
5 s @ 500 rpm	5 s @ 500 rpm
30 s @ 1000 rpm	2 min and 35 s @ 1250 rpm

4.8.4 Device assembly

Figure 4-6 schematically describes the steps for mounting the silicon chip between the PDMS multilayers.[31]

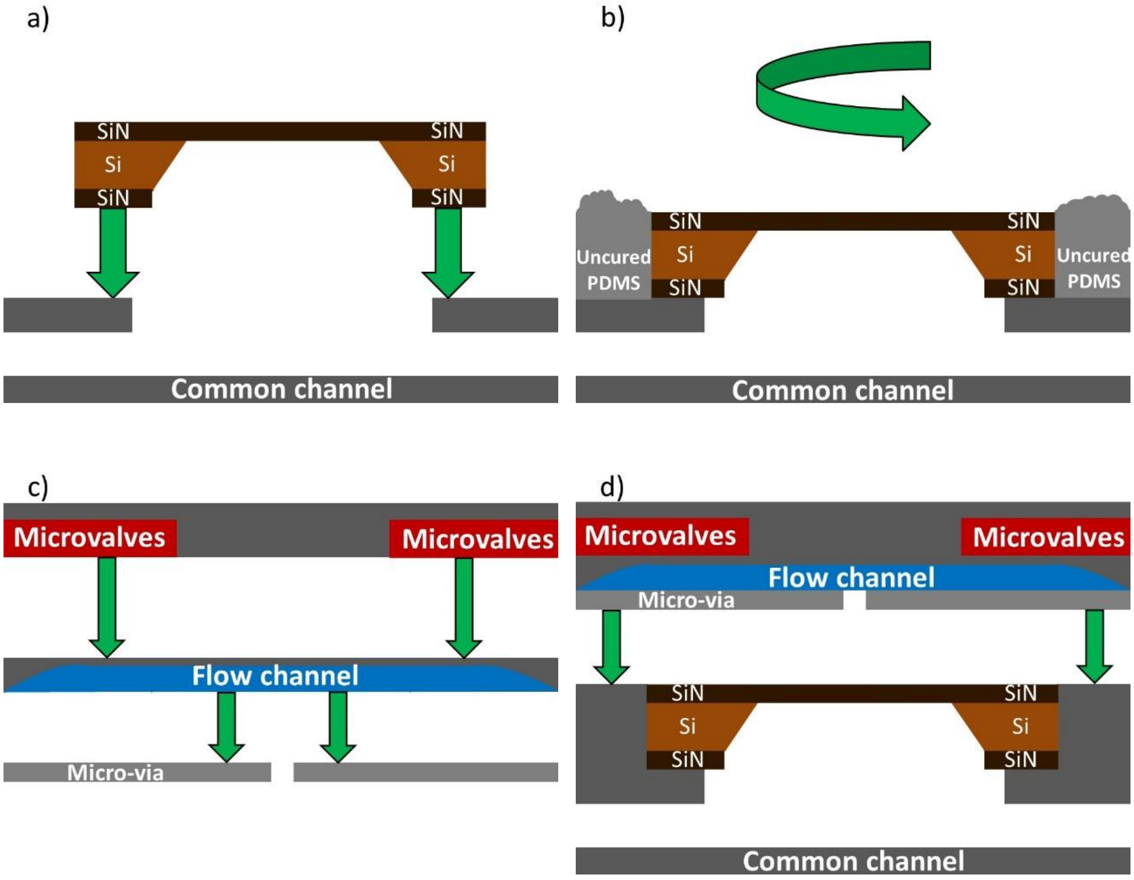

Figure 4-6 Cross section schematic of the procedure used to mount a silicon chip between PDMS layers. **(a)** Following the plasma treatment, the etched side of the silicon chip is bonded to the bottom channel layer atop a hand-punched hole. **(b)** A thin layer of PDMS is then formed around the chip to level its thickness. **(c)** The valve, the flow channel and the microvia layers are respectively plasma treated and bonded together. Here, only the cross section of one of the flow channels is shown. **(d)** Once the thin PDMS layer is cured, the three-layer PDMS composite is aligned over and permanently bonded atop the SiN membrane.

A 2.0 mm hole was hand-punched in the middle of common channel to allow fluidic access to the bottom of the silicon chip. The etched side of the chip was bonded to the common channel atop the punched hole using a plasma system (AutoGlow Research). In order to compensate for the thickness of the silicon chip and leave a level, smooth surface for bonding, a thin layer (100 ± 10 µm) of PDMS was spun around the chip (5 s @ 500 rpm followed by 10 s @ 1000 rpm). This thin layer was cured directly on a hot plate at 80°C for 20 minutes. The three-layer PDMS piece consisted of valve, flow channel and microvia layers which were bonded together using a plasma system followed by a 2-hour oven bake.

In order to precisely situate the PDMS composite atop the SiN membrane, all alignment steps were done using an OAI DUV/NUV mask aligner (Model 206). The plasma bonding steps were performed at 50 W for 30 seconds. Access holes for fluidic and electrode access were punched through the channels (0.75 mm OD for fluidic tubing and 1.25 mm OD for electrodes).

4.8.5 Plasma treatment of an assembled device

While plasma treatment of an assembled device[42] is useful, it is also very important to maintain hydrophobicity of the flow channels where they are compressed by the valves. We built a PDMS gasket for the lid of the plasma chamber through which tubing accommodated to pressurize the valves during plasma treatment. Each tube connects a valve pair to a pressurized vial of deionized water. The valves are pressurized to 30 psi (the pressure used during nanopore fabrication and biomolecular sensing to achieve a high electrical resistance).

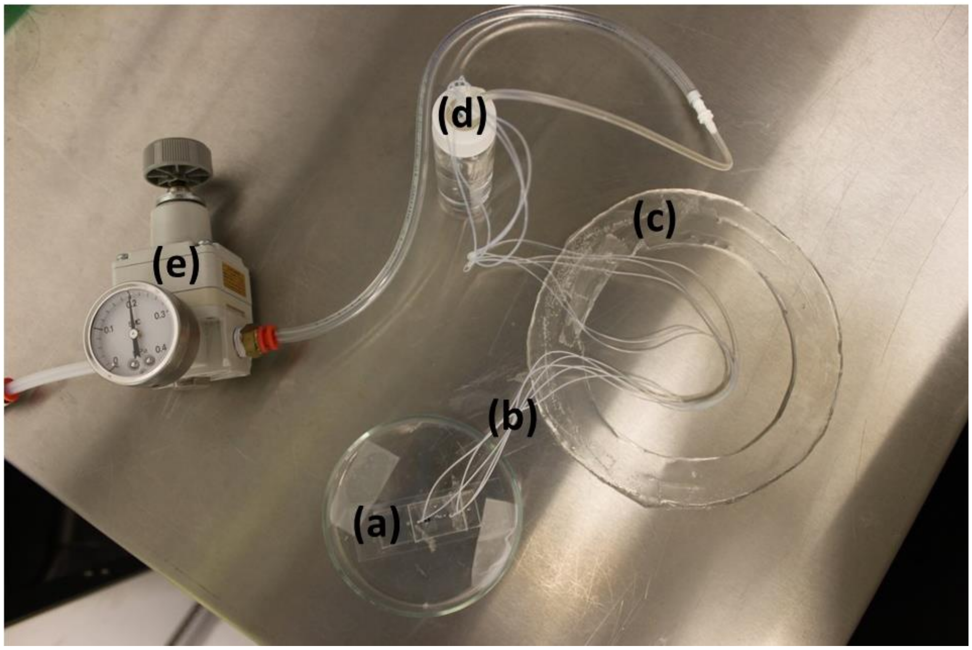

Figure 4-7 The valves of an assembled device **(a)** are connected to tubing **(b)** which fed through a PDMS gasket **(c)** to a vial filled with deionized water **(d)**. The vial is pressurized using compressed air adjusted with a regulator **(e)**.

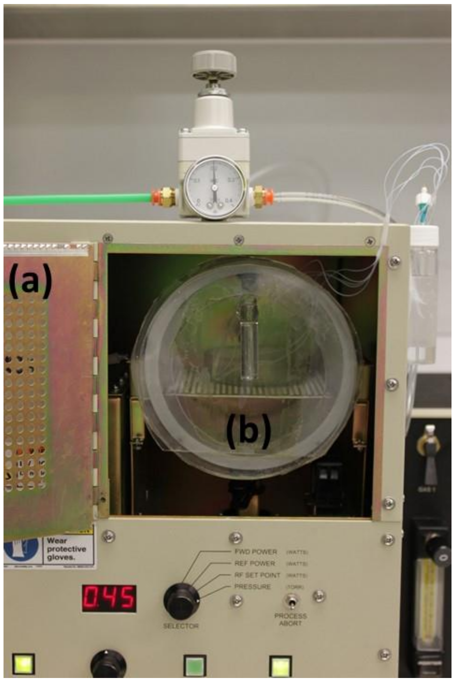

Figure 4-8 The device is treated in a plasma system (a) while the PDMS gasket accommodates the tubing is placed between the chamber of the system and its lid (b) to maintain a vacuum inside the chamber. The device is then treated at 70 W power for 5 minutes while all the valves are pressurized to 30 psi.

4.8.6 Experimental setup and Nanopore fabrication

Each nanopore was fabricated *in situ* by controlled breakdown (CBD).[29] Nanopore fabrication and conditioning[38] was performed in 1 M KCl solution buffered with HEPES at pH 8.3 ± 0.1 with $\sigma = 11.0 \pm 0.1$ Sm^{-1}. Solution conductivity and pH were measured using a VWR Symphony pH/conductivity meter (SB80PC) prior to experiment.

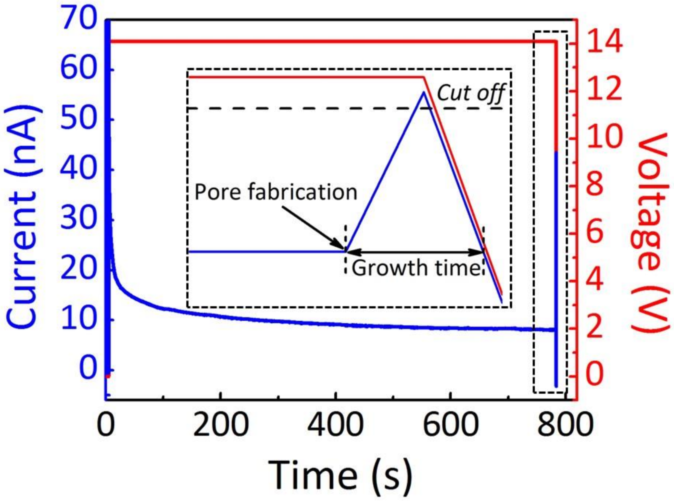

Figure 4-9 A typical nanopore CBD fabrication curve showing leakage current when 14 V is applied across a 20 nm thick SiN membrane in 1M KCl pH 8.3. Inset: The resultant nanopore is detected when a current spike exceeds the predefined threshold current.

Aqueous electrolyte solutions (with or without biomolecular samples) were introduced to the flow channels and nanopore using pressure-driven flow. Solution-containing vials were placed inside the Faraday cage and connected to the microfluidic networks via polyethylene tubing. Flow was then established using pressure regulators (Marsh Bellofram Type 10) and solenoid valves (SMC S070C-SDG-32) located outside of the Faraday cage and controlled by custom-written LabView program.

4.8.7 High electrical resistance obtained by the pressurized valves

Several control measurements were done to verify the functionality of the microvalves for achieving high electrical resistance. Figure 4-10 shows an ionic current trace when 200 mV is applied across five individual nanopores of different diameters in a single device. The functionality of each valve is remarked by electrical disconnection and elimination of the ion current when each valve pair is pressurized.

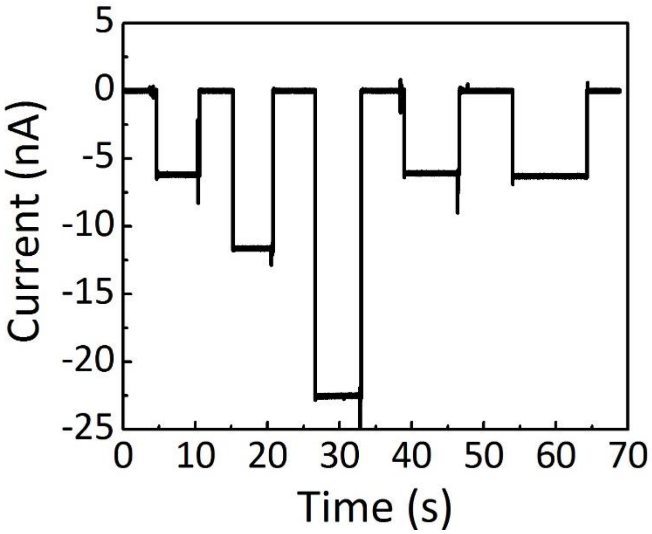

Figure 4-10 Determination of microvalve functionality. When all microvalve pairs are pressurized, no ionic current is observed. When a pair is released and then re-pressurized, a transient ionic current is measured through the corresponding nanopore before an electrical seal is re-established.

4.8.8 Effect of parasitic fluidic flow

As shown by the green histograms in Figure 4-11, the nanopore capture rate is constant if sample is continuously introduced using pressure-driven flow. However, when a sample is segmented between solutions that do not contain biomolecules (such as when a sample is trapped in one flow channel using microvalves while different samples are being loaded in neighbouring channels), parasitic flow in the system can result in sample depletion from the sensing region and a reduction in nanopore capture rate. Although sensing in this regime is possible if great care is taken to minimize flow (red histogram in Figure 4-11b), parasitic flow is difficult to avoid and sample can be lost in a matter of minutes, as shown by the red histogram in Figure 4-11a.

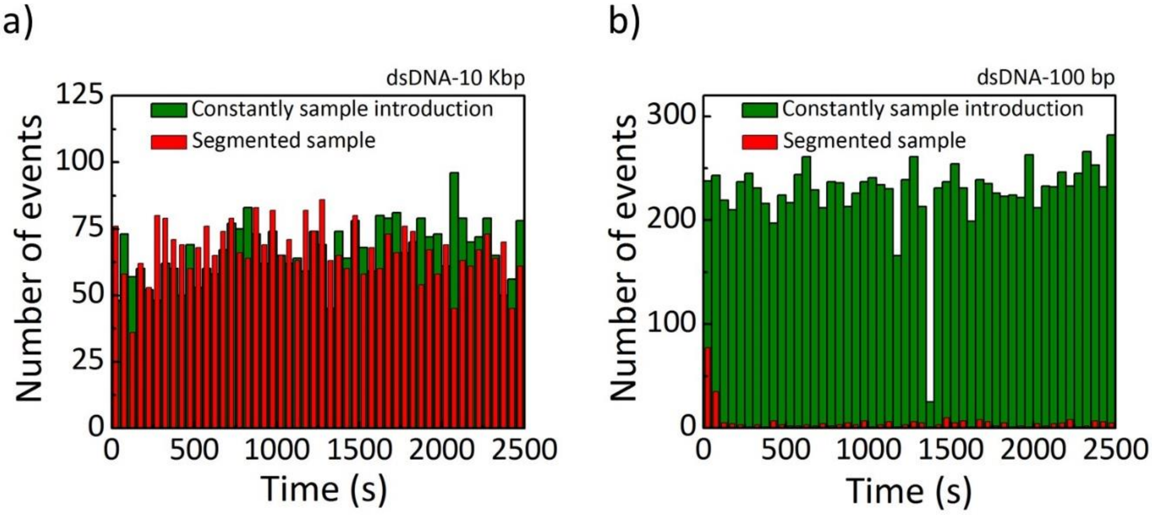

Figure 4-11 Histograms of the number of events detected as a function of experiment time using two different nanopores when samples are constantly fed (green) and segmented between solutions that do not contain biomolecules (red). a) 10 Kbp dsDNA is being sensed, whereas b) 100 bp dsDNA is being sensed through a different nanopore.

4.8.9 Cross sectional profile of the flow channel during microvalves actuation

The cross sectional area of the flow channels beneath a microvalve as a function of valve pressure was determined by fluorescence imaging. Figure 4-12 shows the flow channel cross sections at various valve pressures for the configuration shown in Figure 4-5. This configuration was used for partially collapsing flow channels to minimize flow while allowing electrical access to the nanopore. Here, the flow channels were bonded directly to a glass slide and filled with fluorescent dye solution for quantitative imaging. The channel height was determined by measuring the fluorescence intensity (ImageJ) relative to the maximum intensity in the uncompressed channel, which had a height of 50±1 µm as measured using a profilometer. The cross sectional area of the channel was calculated as the integral of each profile (Figure 4-13).

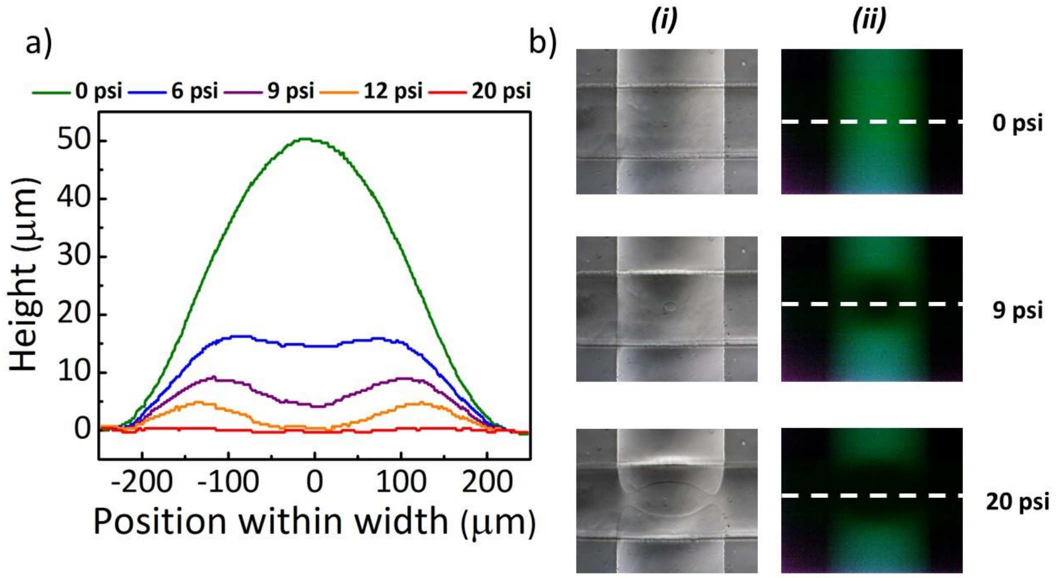

Figure 4-12 **(a)** Flow channel cross sections for different valve pressures obtained through fluorescence imaging. The height of the unpressurized channel was determined with a profilometer measurement of the AZ 50-XT mould for a channel having a 50 µm height and a 400 µm width. **(b)** Bright field **(i)** and fluorescence **(ii)** images of the flow channel and microvalve for various applied pressures. The dashed lines indicate the locations of the profiles shown in **(a)**. The fluorescence images were analyzed with ImageJ.

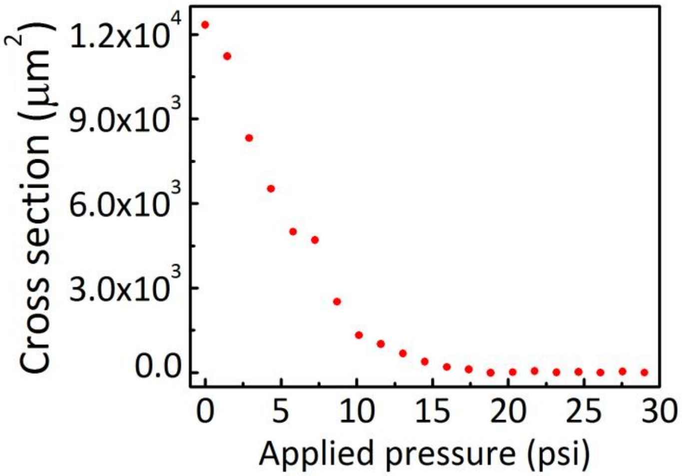

Figure 4-13 Flow channel cross sectional area as a function of valve pressure. The applied pressure on the valve varied from 0 to 29 psi while the flow channel pressure was <2 psi.

4.8.10 Ionic current measurements for partially-pressurized valves

4.8.10.1 Equivalent RC circuit

An equivalent RC circuit of the device is shown in Figure 4-14. The nanopore is modeled as a resistor $\mathbf{R_p}$ which is in parallel with a SiN membrane capacitance $\mathbf{C}$.[45] The pore is electrically connected in series with the resistance caused by the flow channels $\mathbf{R_{ch}} = \frac{\mathbf{l}}{\mathbf{2\sigma A}}$. σ is the conductivity of the electrolyte, l is the length of the channels approaching to either side of the nanopore, **A** is the cross section of the channel and the factor of ½ arises from the fact that the configuration of the flow channels in the device (Figure 4-5) constitute two equal channel resistances in parallel (shown as a single channel resistance in Figure 4-14 for simplicity. Note that with the valves unpressurized, $\mathbf{R_p} \gg \mathbf{R_{ch}}$). By pressurizing the microvalves, the PDMS membrane separating the flow channels from the valve layers gets deflected and reduces the cross section of the channels to $\mathbf{A'}$. This leads to an increase in the total electrical resistance of the flow channels to a value of $\mathbf{R'_{ch}}$, while the passage of DNA molecules increases the nanopore resistance to $\mathbf{R_{DNA}}$.

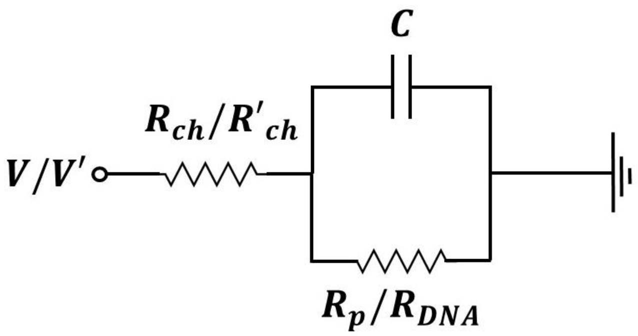

Figure 4-14 Equivalent RC circuits of the device: V is the applied potential difference, R_{ch} the resistance of the flow channel, C the membrane capacitance and R_p the resistance of the nanopore in the open (unoccupied) state. The electrical resistance of the channels increases to R'_{ch} when the microvalves are partially pressurized, which is compensated for by changing the bias voltage to V'. When DNA translocates, the pore resistance is increased to R_{DNA}.

4.8.10.2 Amplitude of biomolecule blockage depth

For events that are long enough to reach a steady state current, we can ignore capacitive effects when calculating the event amplitude. When the microvalves are unpressurized, $R_{ch} << R_p$, and therefore we can ignore the channel resistance, giving $I_0 = \frac{V}{R_p}$. Upon passage of DNA molecule through the pore the current is $I = \frac{V}{R_{DNA}}$, and the change in ionic current produced by DNA translocation will be

$$\Delta I = I_0 - I = \frac{V}{R_p}\left[1 - \frac{R_p}{R_{DNA}}\right] \tag{4-5}$$

When the valves are pressurized, the resistance of the channels is increased, and the applied potential is increased to V' to maintain the ionic current level:

$$I'_o = \frac{V'}{R'_{ch}+R_p} = \frac{V}{R_p} \tag{4-6}$$

Which yields

$$V' = V\left[\frac{R'_{ch}+R_p}{R_p}\right] \tag{4-7}$$

When DNA molecules translocate through the pore, the ionic current can be written as

$$I' = \frac{V'}{R'_{ch}+R_{DNA}} = \frac{V}{R_p}\left[\frac{R'_{ch}+R_p}{R'_{ch}+R_{DNA}}\right] \tag{4-8}$$

The change in ionic current caused by DNA translocation while the valves are pressurized is then

$$\Delta I' = I'_0 - I' = \frac{V}{R_p}\left[\frac{R_{DNA}-R_p}{R'_{ch}+R_{DNA}}\right] \tag{4-9}$$

Giving the ratio of the blockage depths with and without the pressurized microvalves as

$$\frac{\Delta I'}{\Delta I} = \frac{R_{DNA}}{R'_{ch} + R_{DNA}} \qquad (4\text{-}10)$$

4.8.10.3 Distorted ionic current

The general solution for the time evolution of the current response of a DNA molecule translocating through a nanopore is given by[45]

$$I(t) = I_0 + \sum_{k=1}^{N} \Delta I_k \left[1 - \exp\left(-\alpha_k (t - \tau_k)\right)\right] \Theta(t - \tau_k) \qquad (4\text{-}11)$$

The characteristic rise time for step changes in the pore resistance is given by,

$$\alpha_k^{-1} = \frac{C R'_{ch} R_k}{R'_{ch} + R_k} \qquad (4\text{-}12)$$

In which R_k is the resistance of the pore in state k and $I_0 = \frac{V}{R_p + R'_{ch}}$. In the case of a simple single-file DNA translocation such as is considered in this paper, $N = 2$, $R_1 = R_{DNA}$ and $R_2 = R_p$. The magnitude of the current steps ΔI_k is the same as that predicted in Section 4.8.10.2. In the case of unpressurized microvalves, α_k is instead equal to the filter cut-off frequency.

4.8.11 Ionic current noise characterization

At a constant applied potential across the fabricated nanopores, a time series of ionic current is recorded. By performing power spectral density (PSD) measurements, we examined noise in the ionic current through each fabricated nanopore integrated within the microfluidic environment. All measurements are done using a current amplifier, Axopatch 200B (Molecular device), with the 4-pole Bessel filter set at 100 kHz. Figure 4-15 shows the PSD of five nanopores fabricated in a single microfluidic device under an applied potential of 200 mV, in 1 M KCl – pH 8.3.

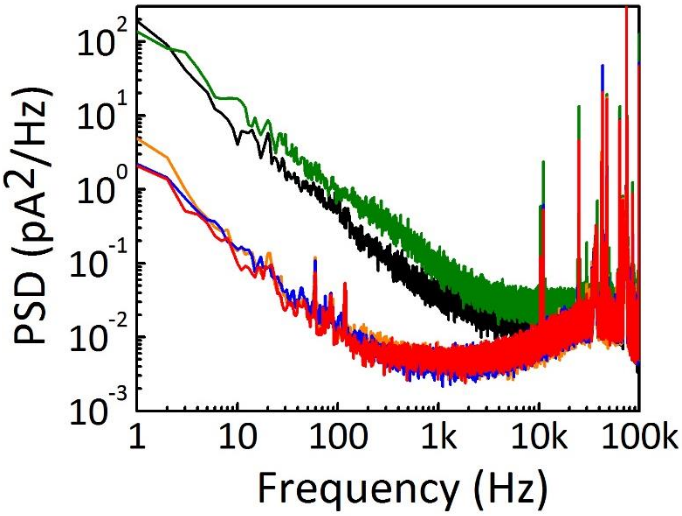

Figure 4-15 Power spectral density (PSD) noise comparison of five nanopores fabricated by CBD within a single microfluidic device. The size of the nanopores are respectively 9.9 nm (Black), 19.5 nm (Green), 6.9 nm (Yellow), 7.9-nm (Blue) and 9.3 nm (Red) in diameter. The measurements are done in 1 M KCl – pH 8.3, sampled at 250 kHz and low-pass filtered at 100 kHz by a 4-pole Bessel filter using a current amplifier, Axopatch 200B.

4.8.12 Typical integrated nanopore-microfluidic device

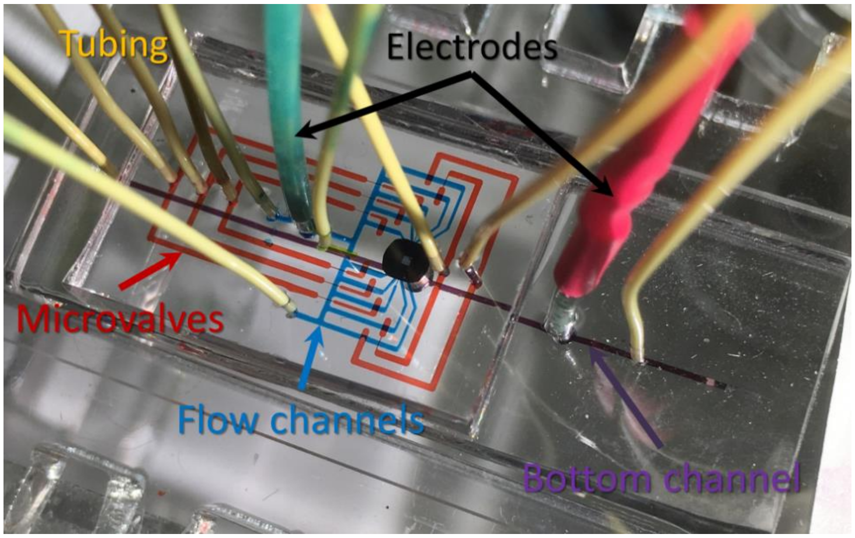

Figure 4-16 A typical integrated nanopore-microfluidic device with five connected flow channels. For clarity, the microfluidic channels including the flow channels, microvalves and common bottom channel, are respectively filled with blue, red and purple food coloring dyes. The fluid tubing and electrodes are labeled as well.

4.8.13 Analysis of nanopore translocation data

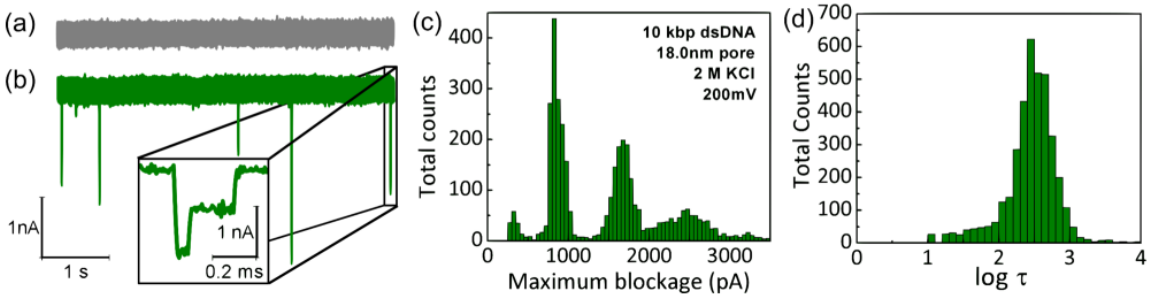

Figure 4-17 Ionic current traces through the 18.0-nm diameter pore shown in Figure 2 before **(a)** and after **(b)** the addition of 10 kbp dsDNA fragments. As expected for nanopores of this diameter, multiple ionic current levels can be seen within individual events as folded molecules translocate through the nanopore (inset). **(c)** A histogram of the maximum ionic current blockage per event shows that linear and singly folded dsDNA translocation results in transient ionic current reductions of 850 ± 60 pA and 1670 ± 90 pA, respectively. **(d)** A histogram of the log-dwell time of translocation events shows the most probable log (τ) = 2.5 ± 0.2 μs.

4.9 Additional note

The flow control diagram is depicted in Figure 4-16. The device has five connected flow channels. The inlet and outlet ports are common between all the flow channels. Solution of interest is driven through the channels by pressurizing the corresponding vial (light blue) with a regulator, (A). The fluid access to each flow channel is controlled by a pair of microvalves. The pressurized routing valve (light green) is designed to direct the solution toward the flow channels. The microvalves are filled with water and individually actuated by pressurizing the related vials (red) which are connected to a separate regulator, (B). The device also has a bottom channel (not shown here) which is common between all the top channels of the device. The corresponding vial for the bottom channel (not shown here) is also pressurized via regulator A.

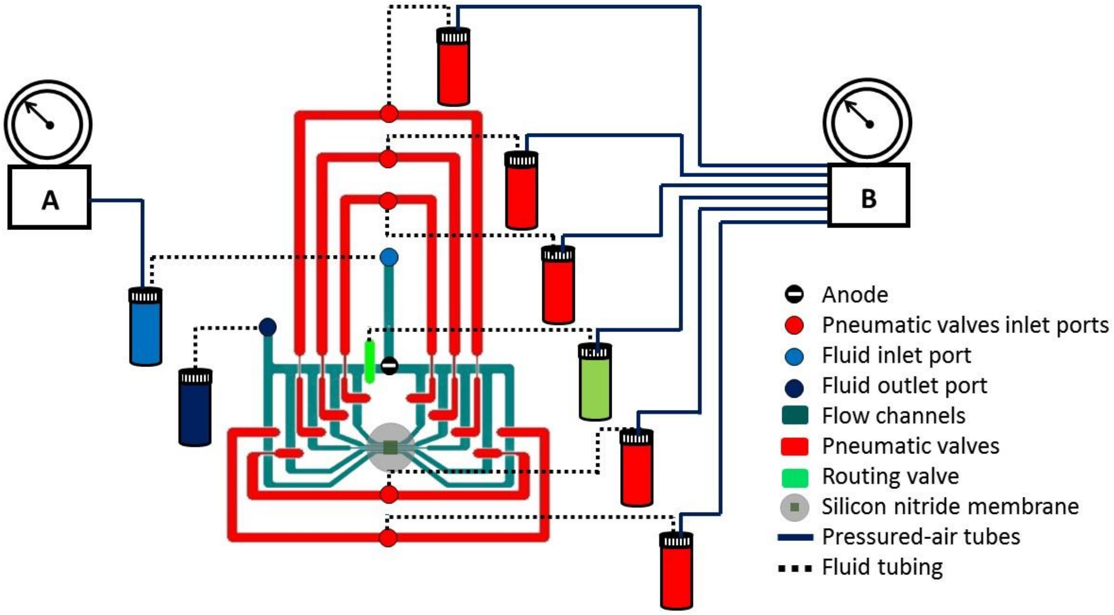

Figure 4-18 Flow control diagram (not to scale). Five connected flow channels are aligned a top a silicon membrane. The fluid and electric access to each flow channel are controlled by pressurizing the corresponding microvalves.

4.10 References

[1] D. W. Deamer, M. Akeson, *Trends Biotechnol.* **2000**, *18*, 147.

[2] D. Branton, D. W. Deamer, A. Marziali, H. Bayley, S. A. Benner, T. Butler, M. Di Ventra, S. Garaj, A. Hibbs, X. Huang, S. B. Jovanovich, P. S. Krstic, S. Lindsay, X. S. Ling, C. H. Mastrangelo, A. Meller, J. S. Oliver, Y. V. Pershin, J. M. Ramsey, R. Riehn, G. V. Soni, V. Tabard-Cossa, M. Wanunu, M. Wiggin, J. A. Schloss, *Nat. Biotechnol.* **2008**, *26*, 1146.

[3] M. Wanunu, *Phys. Life Rev.* **2012**, *9*, 125.

[4] U. F. Keyser, *Phys. Life Rev.* **2012**, *9*, 164.

[5] U. F. Keyser, B. N. Koeleman, S. van Dorp, D. Krapf, R. M. M. Smeets, S. G. Lemay, N. H. Dekker, C. Dekker, *Nat. Phys.* **2006**, *2*, 473.

[6] V. Arnaut, M. Langecker, F. C. Simmel, *Biophys. J.* **2013**, *105*, 1199.

[7] V. Tabard-Cossa, M. Wiggin, D. Trivedi, N. N. Jetha, J. R. Dwyer, A. Marziali, *ACS Nano* **2009**, *3*, 3009.

[8] G. Baaken, N. Ankri, A.-K. Schuler, J. Rühe, J. C. Behrends, *ACS Nano* **2011**, *5*, 8080.

[9] D. J. Niedzwiecki, R. Iyer, P. N. Borer, L. Movileanu, *ACS Nano* **2013**, *7*, 3341.

[10] C. Shasha, R. Y. Henley, D. H. Stoloff, K. D. Rynearson, T. Hermann, M. Wanunu, *ACS Nano* **2014**, *8*, 6425.

[11] M. L. Kovarik, S. C. Jacobson, *Anal. Chem.* **2008**, *80*, 657.

[12] Z. Fekete, G. Huszka, A. Pongrácz, G. Jágerszki, R. E. Gyurcsányi, E. Vrouwe, P. Fürjes, *Procedia Eng.* **2012**, *47*, 13.

[13] J. K. Rosenstein, M. Wanunu, C. A. Merchant, M. Drndic, K. L. Shepard, *Nat. Methods* **2012**, *9*, 487.

[14] B. M. Venkatesan, R. Bashir, *Nat. Nanotechnol.* **2011**, *6*, 615.

[15] B. R. Cipriany, P. J. Murphy, J. A. Hagarman, A. Cerf, D. Latulippe, S. L. Levy, J. J. Benítez, C. P. Tan, J. Topolancik, P. D. Soloway, H. G. Craighead, *Proc. Natl. Acad. Sci. U. S. A.* **2012**, *109*, 8477.

[16] T. M. Squires, S. R. Quake, *Rev. Mod. Phys.* **2005**, *77*, 977.

[17] G. M. Whitesides, *Nature* **2006**, *442*, 368.

[18] E. K. Sackmann, A. L. Fulton, D. J. Beebe, *Nature* **2014**, *507*, 181.

[19] T. N. Shendruk, R. Tahvildari, N. M. Catafard, L. Andrzejewski, C. Gigault, A. Todd, L. Gagne-Dumais, G. W. Slater, M. Godin, *Anal. Chem.* **2013**, *85*, 5981.

[20] J. Riordon, M. Nash, M. Calderini, M. Godin, *Microelectron. Eng.* **2014**, *118*, 35.

[21] E. M. Nelson, V. Kurz, J. Shim, W. Timp, G. Timp, *Analyst* **2012**, *137*, 3020.

[22] N. A. W. Bell, V. V. Thacker, S. Hernández-Ainsa, M. E. Fuentes-Perez, F. Moreno-Herrero, T. Liedl, U. F. Keyser, *Lab. Chip* **2013**, *13*, 1859.

[23] T. Jain, R. J. S. Guerrero, C. A. Aguilar, R. Karnik, *Anal. Chem.* **2013**, *85*, 3871.

[24] A. J. Storm, J. H. Chen, X. S. Ling, H. W. Zandbergen, C. Dekker, *Nat. Mater.* **2003**, *2*, 537.

[25] J. Li, D. Stein, C. McMullan, D. Branton, M. J. Aziz, J. A. Golovchenko, *Nature* **2001**, *412*, 166.

[26] B. Zhang, J. Galusha, P. G. Shiozawa, G. Wang, A. J. Bergren, R. M. Jones, R. J. White, E. N. Ervin, C. C. Cauley, H. S. White, *Anal. Chem.* **2007**, *79*, 4778.

[27] J. Y. Y. Sze, S. Kumar, A. P. Ivanov, S.-H. Oh, J. B. Edel, *Analyst* **2015**, *140*, 4828.

[28] R. Tahvildari, E. Beamish, V. Tabard-Cossa, M. Godin, *Lab. Chip* **2015**, *15*, 1407.

[29] H. Kwok, K. Briggs, V. Tabard-Cossa, *PLoS ONE* **2014**, *9*, e92880.

[30] K. Briggs, H. Kwok, V. Tabard-Cossa, *Small* **2014**, *10*, 2077.

[31] M. A. Unger, H.-P. Chou, T. Thorsen, A. Scherer, S. R. Quake, *Science* **2000**, *288*, 113.

[32] J. Melin, S. R. Quake, *Annu. Rev. Biophys. Biomol. Struct.* **2007**, *36*, 213.

[33] T. Thorsen, S. J. Maerkl, S. R. Quake, *Science* **2002**, *298*, 580.

[34] J. Riordon, M. Mirzaei, M. Godin, *Lab. Chip* **2012**, *12*, 3016.

[35] J. Riordon, M. Nash, W. Jing, M. Godin, *Biomicrofluidics* **2014**, *8*, 11101.

[36] S.-J. Kim, D. Lai, J. Y. Park, R. Yokokawa, S. Takayama, *Small* **2012**, *8*, 2925.

[37] J. N. Lee, C. Park, G. M. Whitesides, *Anal. Chem.* **2003**, *75*, 6544.

[38] E. Beamish, H. Kwok, V. Tabard-Cossa, M. Godin, *Nanotechnology* **2012**, *23*, 405301.

[39] E. Beamish, H. Kwok, V. Tabard-Cossa, M. Godin, *J. Vis. Exp.* **2013**, DOI 10.3791/51081.

[40] D. C. Duffy, J. C. McDonald, O. J. A. Schueller, G. M. Whitesides, *Anal. Chem.* **1998**, *70*, 4974.

[41] V. Tabard-Cossa, D. Trivedi, M. Wiggin, N. N. Jetha, A. Marziali, *Nanotechnology* **2007**, *18*, 305505.

[42] S. H. Tan, N.-T. Nguyen, Y. C. Chua, T. G. Kang, *Biomicrofluidics* **2010**, *4*, 32204.

[43] S. W. Kowalczyk, A. Y. Grosberg, Y. Rabin, C. Dekker, *Nanotechnology* **2011**, *22*, 315101.

[44] M.-H. Lee, A. Kumar, K.-B. Park, S.-Y. Cho, H.-M. Kim, M.-C. Lim, Y.-R. Kim, K.-B. Kim, *Sci. Rep.* **2014**, *4*, DOI 10.1038/srep07448.

[45] A. Balijepalli, J. Ettedgui, A. T. Cornio, J. W. F. Robertson, K. P. Cheung, J. J. Kasianowicz, C. Vaz, *ACS Nano* **2014**, *8*, 1547.

[46] E. S. Page, *Biometrika* **1954**, *41*, 100.

[47] K. Briggs, *CUSUM: Release for DOI Generation by Zenodo*, **2016**.

[48] D. Qin, Y. Xia, G. M. Whitesides, *Nat. Protoc.* **2010**, *5*, 491.

[49] W. W. Flack, H.-A. Nguyen, M. Neisser, E. Sison, P. H. Lu, B. Plass, T. Makii, Y. Murakami, **2005**, pp. 899–911.

Chapter 5 | Conclusion and Outlook

5.1 Summary & Accomplishments

The development of integrated microfluidic devices enables researchers to perform complex and sophisticated experiments on a single chip. Their miniature format allows to detect compounds of interest rapidly in only microliters of required sample volumes. Thus, the microfluidic realm becomes home of a wide variety of applications and embodiments, from sample fractionation to point-of-care diagnostic platform. These small-in-size devices are inexpensive to fabricate and operate, disposable, and require small sample volume for analysis. The manuscripts presented in preceding chapters of this thesis have demonstrated findings and promising results using three microfluidic devices with the application goals in life science.

In biosensors field, nanopore allows label-free sensing of various biological molecules. This leads to major advances in the understanding of fundamental biological processes and potentially revolutionize the world of medicine and technology. The new simplified nanopore fabrication using controlled breakdown (CBD) was an important step toward merging solid-state nanopore technology into more automated and complex systems. For the first time, we deployed microfluidic networks to integrate solid-state nanopore arrays fabricated *in situ*. We presented the requirements and prerequisites for rapidly generating prototype lab-on-a-chip devices.

In **Chapter 3**, we reported highly scalable production of independently addressable nanopores in a single silicon nitride (SiN) membrane. We demonstrated devices with five-independent microchannels while the fabrication of larger arrays of nanopores will be possible by adapting the SiN membrane design and packing them accordingly. The membrane with custom dimensions are commercially available or can be fabricated in-house using wet etching (Section 7.3 of the Chapter 7-Appendix). Inclusion of the microfluidic via (microvia) confines the electric field in the device, results in a pore with better performance. This inclusion minimizes the exposed surface of the membrane to the solution and results in significant reduction of electrical noise during high-bandwidth recording. Potential applications in biomolecular sensing in such a platform include serial probing of one sample through adjacent nanopores, and sequential sensing through a nanopore while neighboring parts of the membrane is broken or clogged.

We then utilized PDMS-based pneumatic microvalves to control on-demand the fluidic and electrical access to each part of the embedded membrane. As discussed in **Chapter 4**, this inclusion allows reducing number of required electrodes. Fully pressure-actuated valves obtain a high electric resistance seal enabling fabrication a new nanopore and/or enlarging an existing nanopore in different regions of a single embedded SiN membrane. Whereas, partially pressure-actuated microvalves results in reduction of the biosample loss while allowing electrical access for sensing. Such precise control on small volume fluid can ultimately be used to effectively purify, sort, and mix biosamples for high throughput on-chip analysis using large-scale arrays of nanopores.

5.2 Future directions – Integrated nanopore-microfluidic device

The presented research on the integrated nanopore-microfluidic device can be extended and improved further in several directions.

One such direction would be on-chip biosample mixing and sensing to build an automated DNA microarray analysis. The microarray is a powerful and popular technology for identification of disease genes. In this method, target DNA molecules suspended in a solution hybridize with surface-bound DNA probes to determine the relative concentration of multiple targets in the sample.[1] However, the conventional methods require quite large volumes of sample and reagent, and the hybridization reaction is limited by slow diffusion kinetics. Several techniques have been investigated within microfluidic devices to improve the efficiency, reduce the relevant time and reagent consumption. For instance on-chip ultrasonic transducers[2], magnetic stirring bars[3], and pneumatically powered pumps[4] are used for active mixing to speed up the reaction time. In another work reported by Wei *et al*, chaotic mixing of droplets in a microfluidic channel is utilized to hybridize 1 µL DNA microarray in 500 seconds.[5]

Translocation of hybridized DNA molecule through a nanopore can obtained the information about binding sites of the probe from the temporal profile of the current trace. If this information is combined with a priori knowledge of probe sequence, considering the partial sequence of the target DNA might then be possible. If the same process is repeated with a library of probes and in massively parallel sequencing, complete sequence of the DNA could be determined. This is the core principle of hybridization assisted nanopore sequencing or the HANS approach.[6] The feasibility of this approach is already demonstrated by detection of trimeric structure consists of ss-ds-ss-ds-ss segments using solid-state nanopores.[7]

As discussed in Chapter 4, inclusion of the microvalves in the integrated device allows routing samples within microfluidic channels. In a primary experiment within an integrated nanopore-microfluidic device with three flow channels and several microvalves, first two single-stranded DNA molecules were individually sensed by two nanopores. In Figure 6-1, A and B represent the two ssDNA samples within the two microfluidic channels. Then by actuating corresponding microvalves, the two ssDNA molecules are brought in contact inside the third, (middle) channel of the device. By giving enough time and incubating the trapped samples, the hybridization of the two ssDNA happened and double-stranded DNA was sensed through the corresponding nanopore (The hybridized sample is labeled C in Figure 6-1). The hybridization of the two ssDNA molecules occurred based on diffusive mixing within the middle microchannel. The increase in the blockade depth was the evidence of the successful process (Figure 6-2). Although the primary results for this study look encouraging, these are the first steps and requires further studies and development. For instance, adding rotary micromixer to the microfluidic networks can accelerate the mixing reaction between the reagents. With this approach, the two samples will be loaded into a loop and completely mixed after actuating peristaltic pumps.[8]

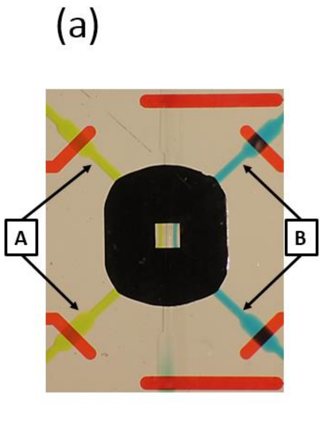

Figure 5-1 An integrated nanopore-microfluidic device with three flow channels and several microvalves to route the samples **(a)** Two different samples are individually detected, **(b)** then they are brought in contact in the middle channel, **(c)** while the corresponding valves for the middle channel are pressurized and samples are trapped, by given enough time, the diffusive mixing results in a new sample. Food coloring dyes are used to illustrate the idea of on-chip mixing.

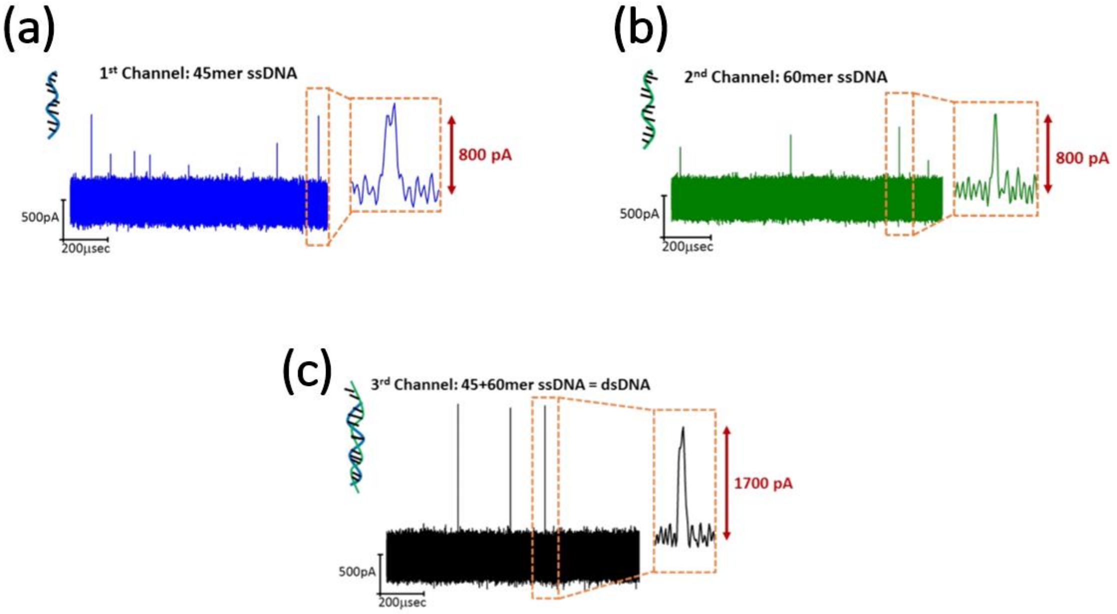

Figure 5-2 In the integrated device a single-stranded DNA (45mer ssDNA) is sensed through one nanopore **(a)** while another single-stranded DNA molecule (60 mer ssDNA) is sensed another nanopore of the device **(b)** The increase in blockade depth indicates the presence of hybridized double-stranded DNA molecule **(c)**.

A second direction would be combining a polymerase chain reaction (PCR) chip[9] with the integrated nanopore-microfluidic device. Such a combination adds the sample preparation step to the chip enables to handle DNA molecule from the preparation region to the amplification region and then detection by the nanopores. However, the noise might arise from the additional thermal and electrical components.

Another alternative for further development is incorporation of the device into MEMS devices such as complementary metal-oxide-semiconductor (CMOS) preamplifier with integrated microelectrodes[10]. This highly engineered platform can significantly reduce electrical parasitic present in measurements with external amplifiers while still utilizing the advantages of microfluidics.

To summarize, the advantages of integration of nanopore sensors within microfluidic environment are numerous with promising future, although it is at an early stage of development.

5.3 References

[1] R. Bumgarner, *Curr. Protoc. Mol. Biol. Ed. Frederick M Ausubel Al* **2013**, *0 22*, Unit.

[2] G. G. Yaralioglu, I. O. Wygant, T. C. Marentis, B. T. Khuri-Yakub, *Anal. Chem.* **2004**, *76*, 3694.

[3] P. K. Yuen, G. Li, Y. Bao, U. R. Müller, *Lab. Chip* **2003**, *3*, 46.

[4] N. B. Adey, M. Lei, M. T. Howard, J. D. Jensen, D. A. Mayo, D. L. Butel, S. C. Coffin, T. C. Moyer, D. E. Slade, M. K. Spute, A. M. Hancock, G. T. Eisenhoffer, B. K. Dalley, M. R. McNeely, *Anal. Chem.* **2002**, *74*, 6413.

[5] C.-W. Wei, J.-Y. Cheng, C.-T. Huang, M.-H. Yen, T.-H. Young, *Nucleic Acids Res.* **2005**, *33*, e78.

[6] X. Ling, B. Bready, *Hybridization Assisted Nanopore Sequencing*, **2007**, US20070190542 A1.

[7] V. S. K. Balagurusamy, P. Weinger, X. S. Ling, *Nanotechnology* **2010**, *21*, 335102.

[8] J. Melin, S. R. Quake, *Annu. Rev. Biophys. Biomol. Struct.* **2007**, *36*, 213.

[9] C. Zhang, J. Xu, W. Ma, W. Zheng, *Biotechnol. Adv.* **2006**, *24*, 243.

[10] J. Rosenstein, V. Ray, M. Drndic, K. L. Shepard, in *Life Sci. Syst. Appl. Workshop LiSSA 2011 IEEENIH*, **2011**, pp. 59–62.

Chapter 6 | Other contributions

6.1 An experiment supports a new theory

In addition to the primary work presented in Chapters 3 and 4, I also co-first-authored a paper titled "Field-flow fractionation and hydrodynamic chromatography on a microfluidic chip"[1] in collaboration with **Dr. Tyler Shendruk**, a former PhD candidate at the time in **Professor Gary Slater's group** at the University of Ottawa.

Field-flow fractionation (FFF)[2,3] is a family of useful techniques for separating various sizes of macromolecules and particles in which the separation is achieved by imposing perpendicular external force across a channel of height h to a solution of particles flowing under parabolic velocity profile. Particles of different size will elute at different rates as they settle at different height in the fluidic channel. In this work, Gravitational field-flow fractionation (GrFFF) and hydrodynamic chromatography applied to a broad range of microbead sizes eluting through 18μm microfluidic channels. Ideal theory predicts four operational-modes, from hydrodynamic chromatography to Faxén-mode.[4] The average retention ratio of colloids with both a large specific weight and neutral buoyancy was investigated using video microscopy and mesoscopic simulations. By eluting microbeads at various sizes, including particles that barely fit in the microchannel, we experimentally prove for the first time the existence of Faxén-mode, and the transition from hydrodynamic chromatography to normal-mode field-flow fractionation. Miniaturized FFF systems have been used previously but, to the best of our knowledge, never with such a relatively broad range of particle radii or for such small channel heights.

Our findings show that retention ratios are largely reduced above the steric-inversion point, causing the variation of the retention ratio in the steric- and Faxén-mode regimes to be suppressed due to increased hydrodynamic interactions (drag) with the microchannel walls. This demonstrates the importance of wall effects on the transport of colloids with diameters comparable to channel heights. Furthermore, our results show that normal mode FFF remains a high selectivity technique in microfluidic channels that can be implemented with a simple channel design. We propose that modification to the ideal FFF theory in microchannels can be used to optimize the separation efficiency. This also provides a correction to particle tracking velocimetry (PTV) techniques when applied to microfluidic systems.

In this project, I, **Radin Tahvildari**, led the large majority of experimental work including: microfabrication (soft lithography, PDMS moulding, and assembly of the devices), sample preparation, data acquisition by video microscopy and analysis of the experimental data. **Tyler Shendruk** developed the theory and was responsible for the simulations and determining the form of the wall-induced lag. The work was done under the supervision of **Professor Michel Godin** and **Professor Gary Slater**. Preliminary work was presented as a poster at the 2012 Gordon Research Conferences,

- T.N. Shendruk, **R. Tahvildari**, C. Gigault, L. Andrzejewski, A. Todd, L. Gagne-Dumais, M. Godin, G.W. Slater, "FFF: Verification of Faxn-mode, FFF: Verification of Faxén-mode", Gordon Research Conferences: Colloidal, Macromolecular & Polyelectrolyte Solutions, February 2012 (Poster).

I also had the opportunity to present these results at the **2014 Ontario-on-a-chip (OOAC9)/MATCH symposium, Toronto, Canada**.

- **R. Tahvildari**, T. N. Shendruk, G. Slater, M. Godin, "Modifications to gravitational field-flow fractionation and hydrodynamic chromatography in a microchannel", *Ontario-on-a-Chip/MATCH*, Toronto, Ontario, Canada, 2014 (Poster).

6.2 References

[1] T. N. Shendruk, R. Tahvildari, N. M. Catafard, L. Andrzejewski, C. Gigault, A. Todd, L. Gagne-Dumais, G. W. Slater, M. Godin, *Anal. Chem.* **2013**, *85*, 5981.

[2] J. C. Giddings, *J. Chem. Phys.* **1968**, *49*, 81.

[3] F. A. Messaud, R. D. Sanderson, J. R. Runyon, T. Otte, H. Pasch, S. K. R. Williams, *Prog. Polym. Sci.* **2009**, *34*, 351.

[4] T. N. Shendruk, G. W. Slater, *J. Chromatogr. A* **2012**, *1233*, 100.

Chapter 7 | Appendix

7.1 List of the Photomasks

Project/Specifications	Full view	Close view
Gravitational field-flow fractionation Designed by Andrew Todd January 2011 Polarity: Negative (Inverted for printing) Photoresist: SU8-10	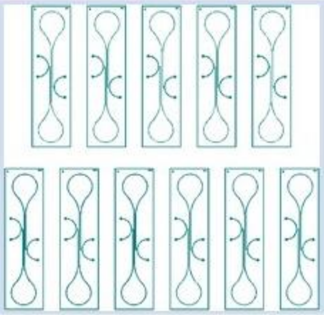	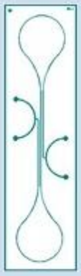
Integrated nanopore-microfluidic Top channel (Single, Dual and Triple) Designed by Radin Tahvildari November 2012 Polarity: Negative (Inverted for printing) Photoresist: SU8-10	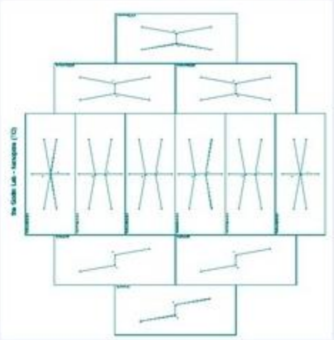	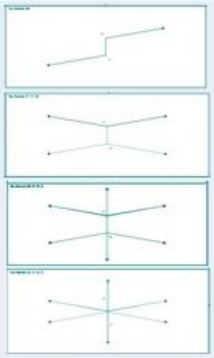
Integrated nanopore-microfluidic Bottom channels Designed by Radin Tahvildari November 2012 Polarity: Negative (Inverted for printing) Photoresist: SU8-2050	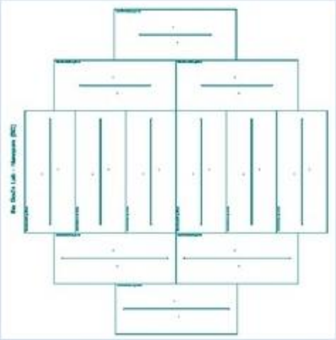	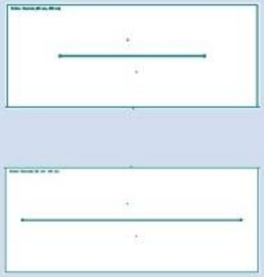
Integrated nanopore-microfluidic Wider top channels Designed by Radin Tahvildari March 2013 Polarity: Negative (Inverted for printing) Photoresist: SU8-2050	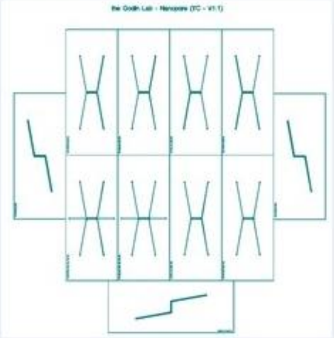	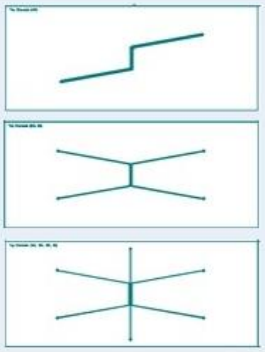

Project/Specification	Full view	Close view
Integrated nanopore-microfluidic Top channels Designed by Radin Tahvildari August 2014 Polarity: Negative (Inverted for printing) Photoresist: SU8-2050	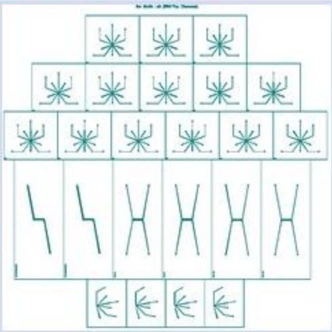	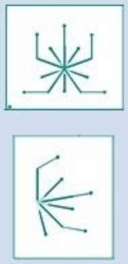
Integrated nanopore-microfluidic Microfluidic vias Designed by Radin Tahvildari August 2014 Polarity: Negative (Inverted for printing) Photoresist: SU8-2050	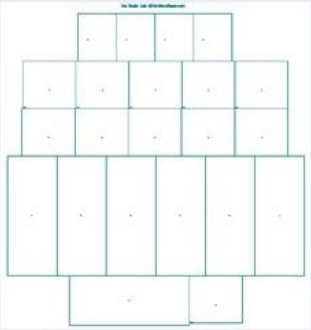	
Integrated nanopore-microfluidic Valves Designed by Radin Tahvildari December 2014 Polarity: Negative (Inverted for printing) Photoresist: SU8-2050	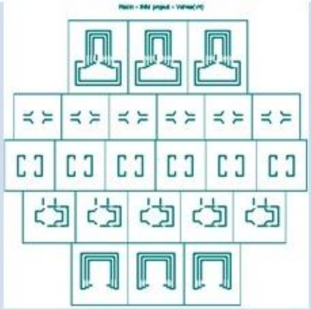	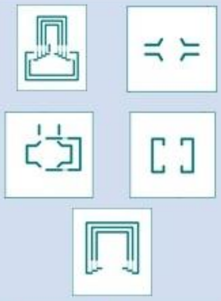
Integrated nanopore-microfluidic Flow channels Designed by Radin Tahvildari December 2014 Polarity: Positive Photoresist: AZ-50XT	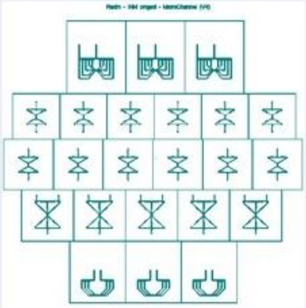	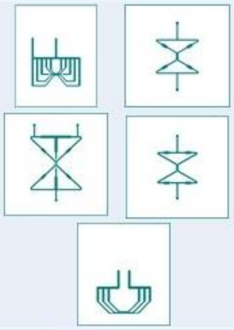
Integrated nanopore-microfluidic Microfluidic vias Designed by Radin Tahvildari December 2014 Polarity: Negative (Inverted for printing) Photoresist: SU8-2050	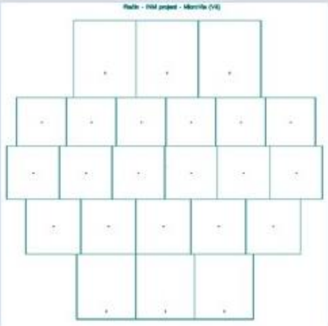	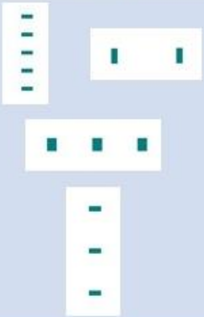

Project/Specification	Full view	Close view
Integrated nanopore-microfluidic Bottom channels Designed by Radin Tahvildari June 2015 Polarity: Negative (Inverted for printing) Photoresist: SU8-2050	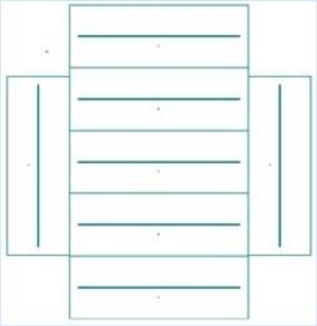	
Integrated nanopore-microfluidic Valves Designed by Radin Tahvildari June 2015 Polarity: Negative (Inverted for printing) Photoresist: SU8-2050	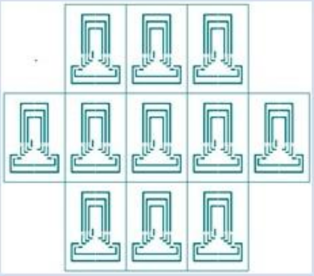	
Integrated nanopore-microfluidic Flow channels Designed by Radin Tahvildari June 2015 Polarity: Positive Photoresist: AZ-50XT	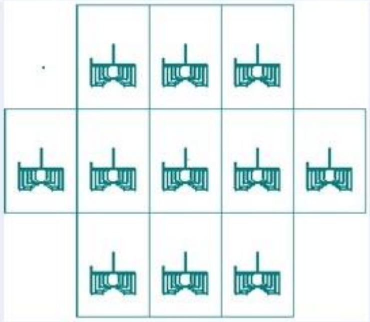	
Integrated nanopore-microfluidic Microfluidic vias Designed by Radin Tahvildari June 2015 Polarity: Negative (Inverted for printing) Photoresist: SU8-2050	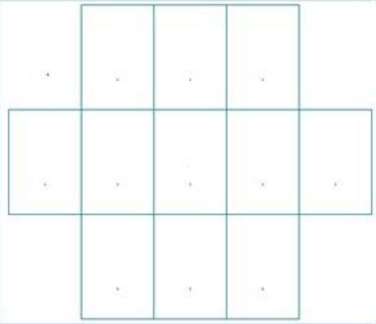	

7.2 Faraday cage

Design and dimensions of the Faraday cage are shown as follows,

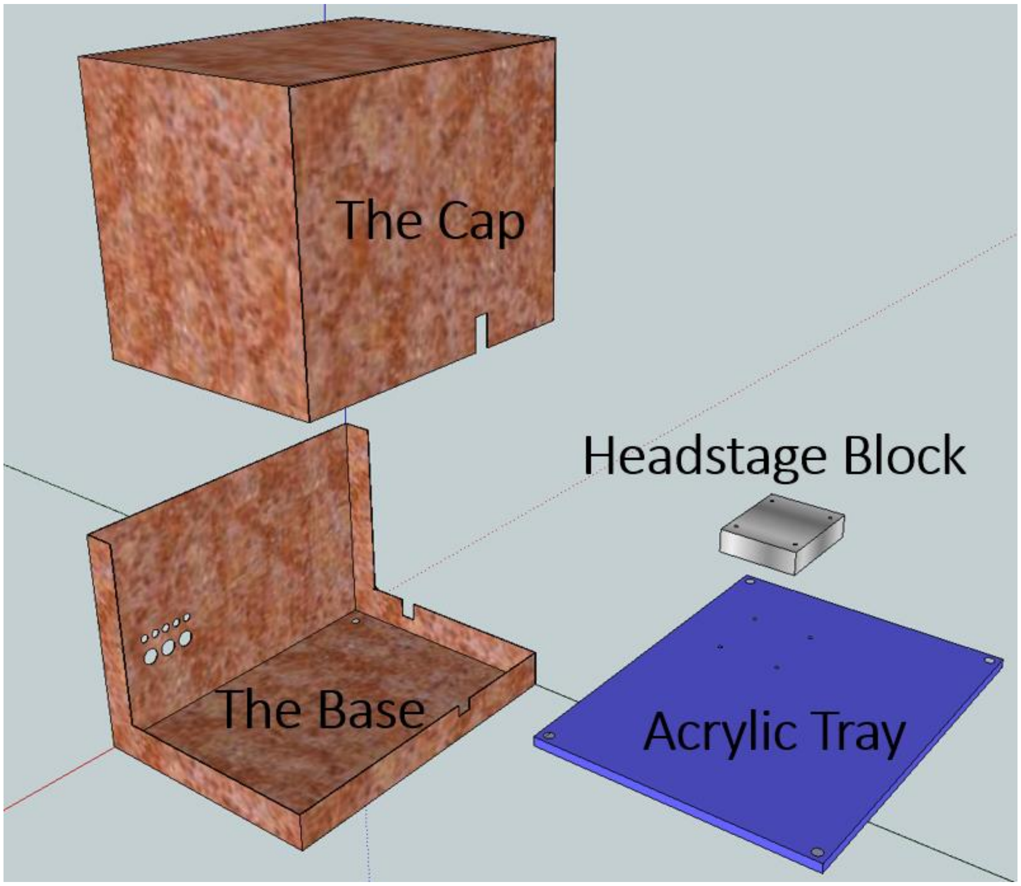

Figure 7-1 Design overview of the Faraday cage drew in Google Sketchup.

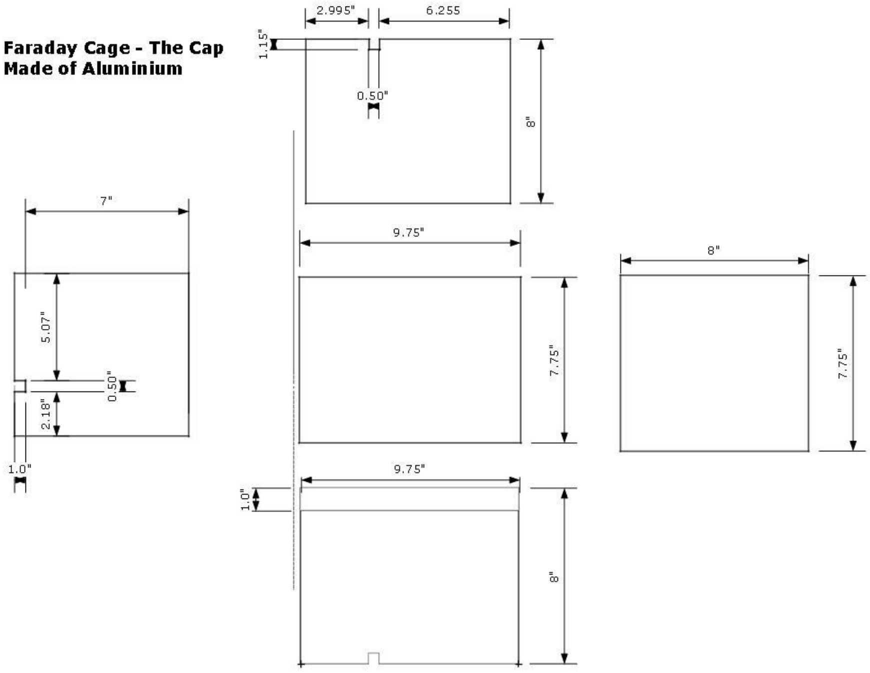

Figure 7-2 Dimensions of the Cap for the Faraday cage

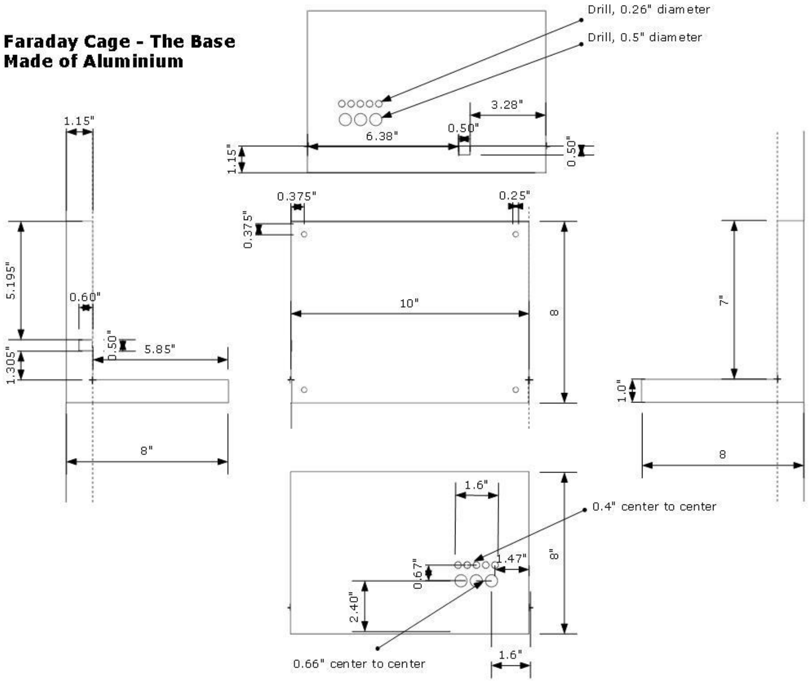

Figure 7-3 Dimensions of the Base for the Faraday cage

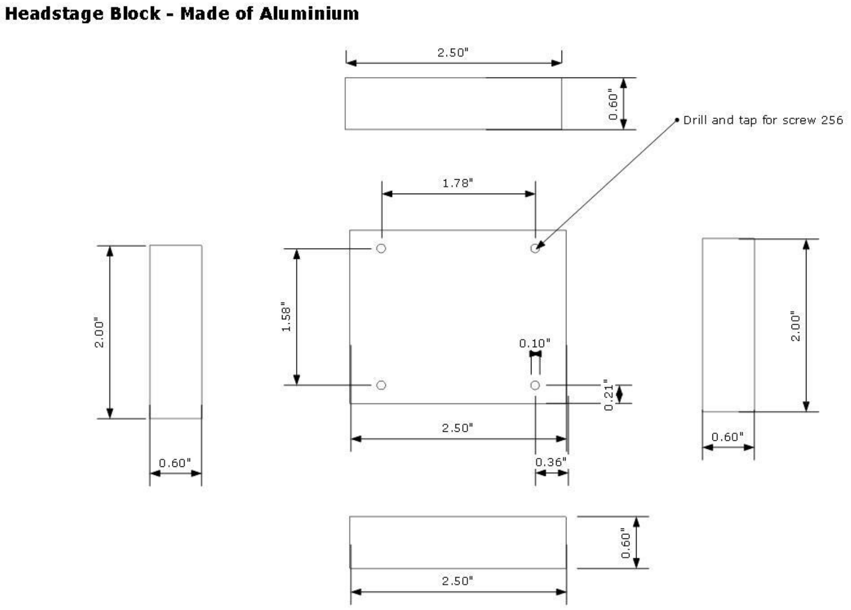

Figure 7-4 Dimensions of the Block on which the headstage is attached

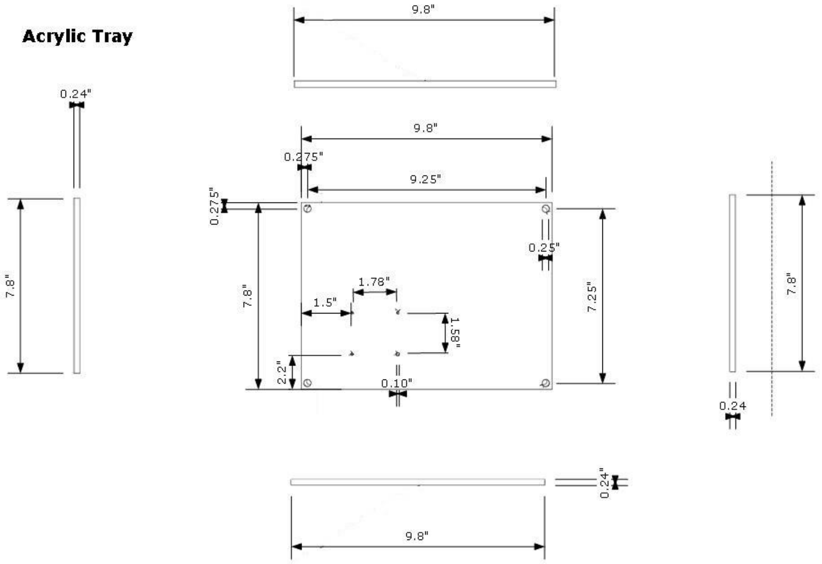

Figure 7-5 Dimensions of the Aclyic Tray placed inside the Faraday cage

7.3 In-house fabrication of SiN membrane

The devices presented in Chapter 3 and 4 are highly scalable and the fabrication of larger arrays of nanopores will be possible by adapting the membrane design and packing them accordingly. As discussed earlier in, during the course of this study, commercial silicon chips with 500×500-µm^2 silicon nitride (SiN) membrane (SiMPore Inc. SN100-A20Q05) were embedded between PDMS microfluidic channel arrays. While different arrangements were explored, this membrane size accommodates limited number of fluidic channels. Therefore, in-house fabrication of SiN membrane will open more design flexibilities as well the ability to expand the number of parallel fluidic channels. This also allows to fabricate membrane with very large window which facilitates transfer printing of the membrane within microfluidic networks.[1] Although such fabrication is considerably more demanding and time-consuming, it results in more cost-effective production of almost 500 individual chips with various geometries out of a single wafer. The procedure typically consists of three main steps; photolithography, Buffered Oxide Etch (BOF) or Reactive Ion Etching (RIE) followed by Potassium Hydroxide (KOH) etch.[2]

For this purpose, 100-mm in diameter, 200µm-thick silicon wafers coated with 30±5nm low-stress silicon nitride on both sides were purchased (Norcada Inc. W-SIN-X). The silicon wafer requires to have <100> crystallographic direction for an anisotropic etching. Firstly, photolithography is performed and areas for selective etching of the SiN layer are defined on one side of the wafer. The steps of the photolithography process, described earlier in Chapter 2, are also illustrated in Figure A-6. A patterned wafer as the result of the photolithography procedure is shown in Figure A-7.

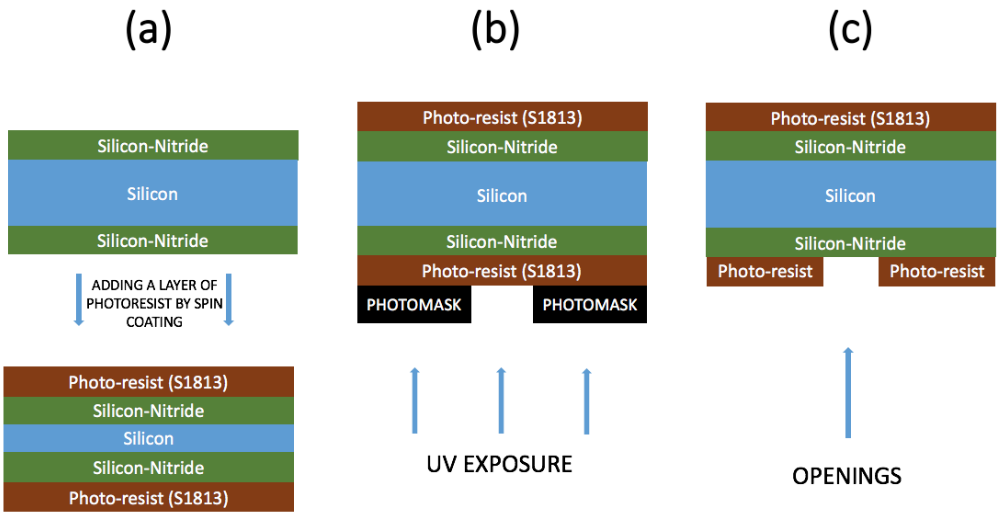

Figure 7-6 Steps of the photolithography to define areas for silicon nitride (SiN) etch, **(a)** A layer of the photoresist (S1813) is coated both sides of the wafer, **(b)** The coated layer on one side is only exposed to UV light through a photomask with the desire designs, **(c)** After removal of unexposed photoresist, only specific areas of the SiN remain opened.

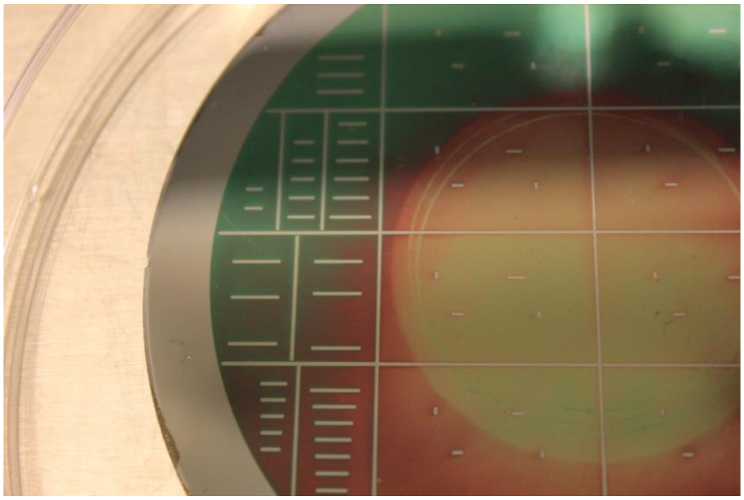

Figure 7-7 A patterned wafer after performing the photolithography procedure

Figure A-8 illustrates the etching steps for a patterned wafer. During the course of this study, the patterned wafer is exposed to 5% BOF for selectively SiN removal through the defined openings. The etching rate of SiN in 5% BOF at room temperature is about 1.3 nm/min.[3] Therefore, the 30-nm SiN layer should be etched within 20 to 25 minutes (Figure A-9). Afterwards, the remained photoresists are removed by an organic solvent, and the wafer is washed with deionized water.

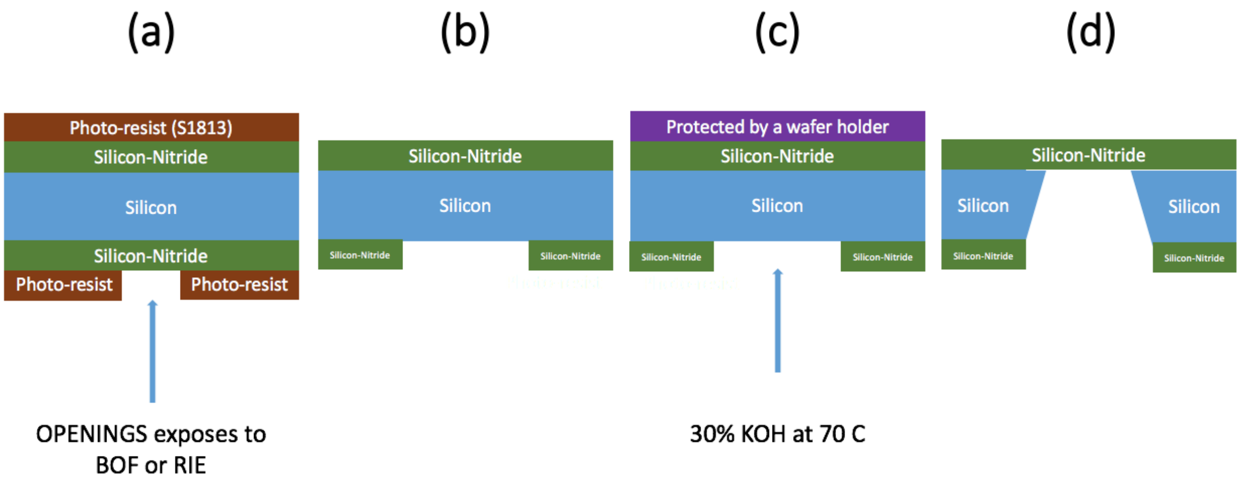

Figure 7-8 Etching steps of a patterned wafer, **(a)** SiN is selectively removed using either Buffered Oxide Etch (BOF) or Reactive Ion Etching (RIE), **(b)** The remained photoresist films are removed from the wafer with an organic solvent, **(c)** The wafer is then placed tightly in a holder to protect one side of it while the other side is exposed to 30% Potassium Hydroxide (KOH) at 70C, **(d)** The SiN layer acts as a mask and enables the selective removal of silicon substrate of the wafer. Pyramidal pits etch down to the silicon wafer and the freestanding SiN membranes are formed.

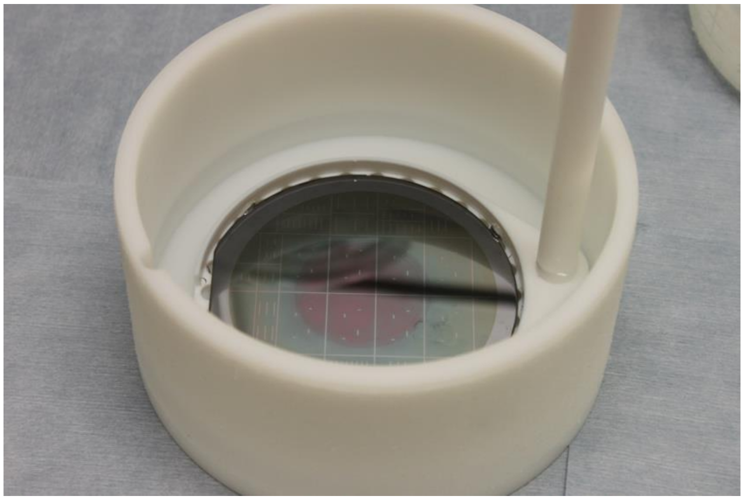

Figure 7-9 Over the course of this study, the selective removal of SiN from the patterned wafer is often performed in BOF. The dish and the holder are made of high density polyethylene.

Etching the exposed silicon substrate is carried out using KOH etch. For this purpose, the wafer is placed in a holder and entirely immersed in 30% KOH solution at 70C (Figure A-10). The etching rate of silicon in such a condition is 45 µm/hr and the 200-

µm thick silicon is etched approximately within 5 hours. The etch rate of silicon is very fast in the <100> direction and results in pyramidal pits etch down to the silicon wafer only in the defined spots that are not protected by SiN layer.[4]

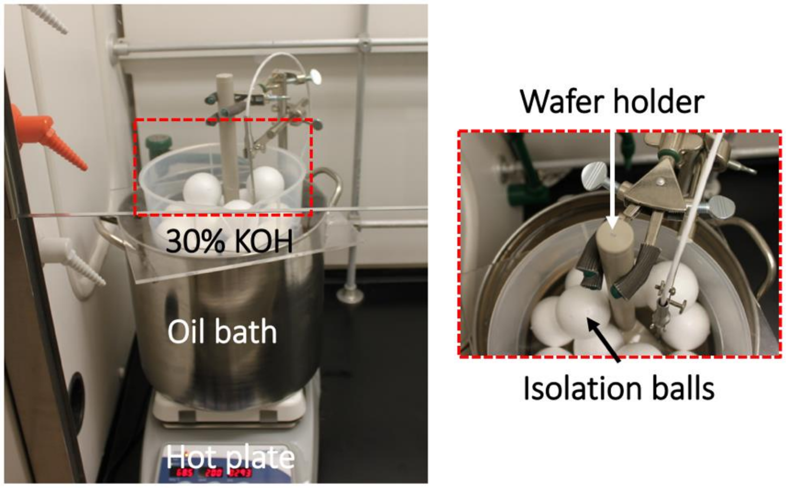

Figure 7-10 The wafer is tightly sealed in a holder to be protected on one side and entirely immersed in a 30% KOH solution heated at 70C. The heat is transferred from a hot plate to the container of KOH using an oil bath.

The KOH etching should be monitored until the free standing membranes are observed at the spots defined by the photolithography features. Several fully etched chips with different dimensions are shown in Figure A-11.

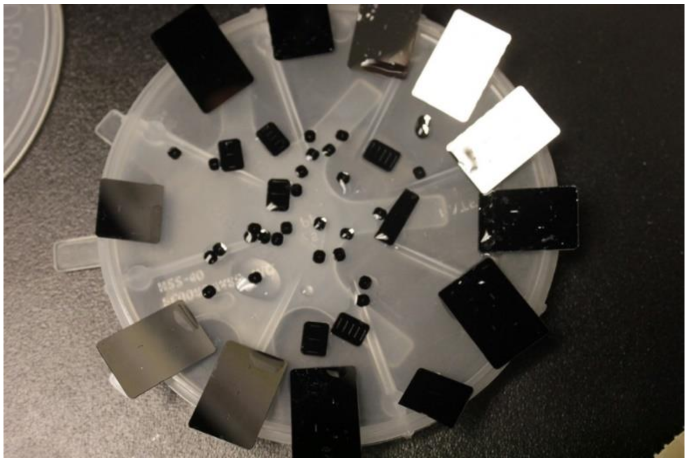

Figure 7-11 Fully etched chips with different dimensions contain freestanding SiN membranes

As shown in Figure A-12, the in-house fabricated SiN membrane is embedded within the microfluidic networks following the similar assembly steps earlier described in Chapters 3 and 4. However, at this stage the fabricated membranes require to be tested for nanopore fabrication and sensing experiments within microfluidic devices. Moreover, the chip designs and fabrication protocols require further modifications.

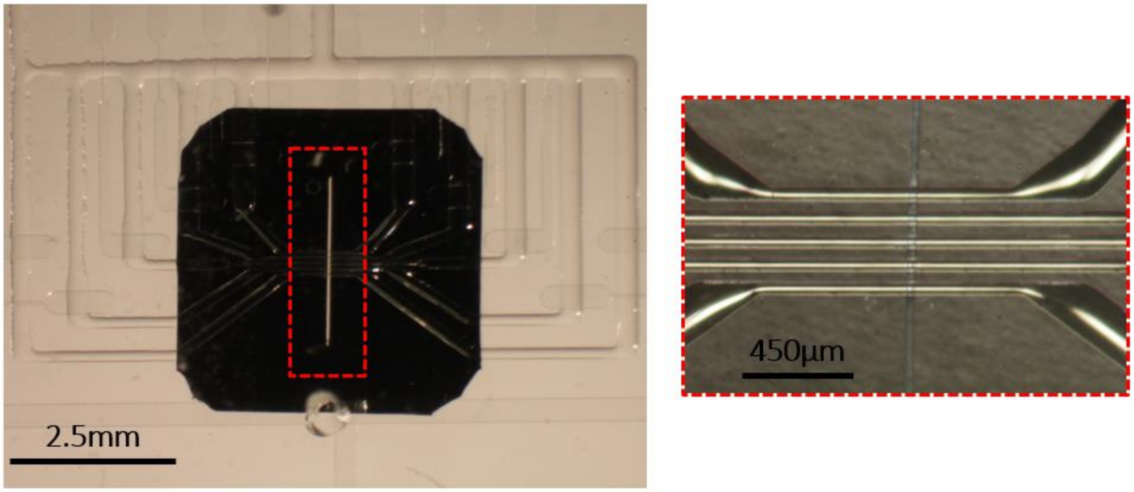

Figure 7-12 An in-house fabricated SiN membrane is embedded within microfluidic networks.

7.4 Further Protocols

7.4.1 Piranha cleaning of the silicon wafers for mould fabrication

1) All organic solvents should be removed from the fumehood.
2) Cover the bench surface with blue wipes to indicate acid spills.
3) Leave the water running at all time for safety.
4) Fill 200mL of distilled water in a clean 1L beaker and labelled “acid waste”.
5) Wear goggles, a protective face mask, apron, and protective (antacid) gloves.
6) Measure 10mL of H2O2 and 30 mL of sulfuric acid.
7) Mix them together in a glass dish with a flat bottom accommodated in a secondary glass dish.
8) Everything that comes in contact with acid should be rinsed thoroughly prior to disposal.
9) Place the wafer gently in the piranha solution.

10) After 15 minutes, shake the acid bath gently.

11) After 30 minutes, transfer the wafer into a clean glass dish filled with deionized water and let them seat for 5 minutes.

12) Immerse the wafer in fresh deionized water, for two more times each for 5 minutes, to ensure complete removal of the acid.

13) Blow dry the wafer with nitrogen and place it in a covered clean petri-dish

13) Empty the acid in the waste beaker and let it degas overnight.

7.4.2 Plasma cleaning of the wafers

The wafer can be plasma cleaned at 200 W for 10 minutes in a plasma system. This is as an alternative process instead of piranha cleaning. Cooling time for 5 minutes should be given before proceeding further. This is the only technique for cleaning of the silicon nitride used for KOH etching.

7.4.3 Photolithography of the silicon nitride wafer

1) Spincoat one side of the wafer with S1813 (Shipley) at 500 rpm for 10 seconds follow by 3000 rpm for 30 seconds.

2) Bake the wafer on a hotplate at 115C for 2 minutes, follows by 5-minute cooling time.

3) Repeat steps 2 and 3 for the other side of the wafer.

4) Expose the side that the features should be formed to UV light for 20 seconds through the designed photomask.

5) Mix 36 mL of deionized water with 4 mL of TMAH.

6) Immerse the wafer in the mixed solution for 45 seconds.

7) Wash the wafer with deionized water follows by drying it with nitrogen gas.

7.5 Buffer solutions

Eric Beamish, PhD candidate in the Godin lab, wrote majority of the following protocols for buffer solutions preparation. They are also available through the Godin lab wiki.

7.5.1 Materials

1) Potassium Chloride (KCl) (BP366 – Fisher Scientific), MW = 74.55 g/mol
2) Lithium Chloride (LiCl) (L121 – Fisher Scientific), MW 42.39 g/mol
3) HEPES buffer (BP310 – Fisher Scientific), MW = 283.3 g/mol
4) EDTA (431788 – Aldrich Chemistry), MW = 292.24 g/mol
5) Potassium hydroxide (KOH), MW = 56.11 g/mol
6) Vacuum filtration unit, (10040-436 – VWR – 0.2 µm pore size)
7) Deionized water
8) pH/conductance meter

7.5.2 Preparation

1) Partially fill a clean lab beaker to slightly less than the final desired volume.
2) Measure out salt and buffer powder (and optionally 1 mM EDTA) and add to DI water (Check the table below).
3) Fill the beaker to final desired volume with DI water.
4) Add magnetic stir bar to the solution and mix it on a stirrer until the salt completely dissolved.
5) Bring the solution to the desired pH by adding 2 M KOH dropwise while monitoring with a pH meter.
6) Afterwards, measure the conductance.

Table 7-1 Protocol for buffer solutions preparation (pH 8.0)

Solutions	**Volume**	**Mass of salt (gr)**	**Mass of buffer (gr)**	**Mass of EDTA (gr)**
1 M KCL, 10mM HEPES	500 mL	37.5	1.4	0.15
2 M KCL, 10mM HEPES	500 mL	74.5	1.4	0.15
3 M KCL, 10mM HEPES	500 mL	112	1.4	0.15
1 M LiCL, 10mM HEPES	500 mL	22	1.4	0.15
3.6 M LiCL, 10mM HEPES	500 mL	76.5	1.4	0.15
4 M LiCL, 10mM HEPES	500 mL	85	1.4	0.15

To make salt solution with **pH 10.0**, "**HEPES**" should be replaced by "**Sodium Bicarbonate (NaHCO3)**". For this purpose, **0.42 gr of NaHCO3** should be added to **500 mL** of the solution.

To prepare **2 M KOH**, **11.3 gr of potassium hydroxide (KOH)** should be dissolve in **100 mL of deionized water**. This requires to be done in the fumefood while wearing goggles, a protective face mask, apron, and protective gloves.

7.6 References

[1] T. Jain, R. J. S. Guerrero, C. A. Aguilar, R. Karnik, *Anal. Chem.* **2013**, *85*, 3871.

[2] T. Gibb, M. Ayub, in *Eng. Nanopores Bioanal. Appl.*, William Andrew Publishing, Oxford, **2013**, pp. 121–140.

[3] K. R. Williams, K. Gupta, M. Wasilik, *J. Microelectromechanical Syst.* **2003**, *12*, 761.

[4] "MEMS: Design and Fabrication," can be found under https://www.crcpress.com/MEMS-Design-and-Fabrication/Gad-el-Hak/p/book/9780849391385, **2005**.